TECHNISCHE UNIVERSITÄT MÜNCHEN

Lehrstuhl für Technische Chemie 2

Novel Solid Sorbents for CO_2 Capture and Evaluation to Applied Systems

Maximilian Werner Hahn

Vollständiger Abdruck der von der Fakultät für Chemie der Technischen Universität München zur Erlangung des akademischen Grades eines

Doktor-Ingenieurs (Dr.-Ing.)

genehmigten Dissertation.

Vorsitzender: Univ.-Prof. Dr.-Ing. Kai-Olaf Hinrichsen

Prüfer der Dissertation:
1. Univ.-Prof. Dr. techn. Johannes A. Lercher
2. Univ.-Prof. Dr.-Ing. Harald Klein

Die Dissertation wurde am 11.02.2015 bei der Technischen Universität München eingereicht und durch die Fakultät für Chemie am 11.05.2015 angenommen.

„Probleme kann man niemals mit derselben Denkweise lösen, durch die sie entstanden sind." – A. Einstein

Statutory Declaration

I declare that I have authored this thesis independently, that I have not used other than the declared sources/resources, and that I have explicitly marked all material which has been quoted either literally or by content from the used sources. At the end of each chapter all collaborators are listed and their specific contribution is addressed. Published content of this thesis is clearly marked at the beginning of each chapter and the publishing agreement of the publisher is stated.

_____, _____ _____

Acknowledgment

First I would like to thank Johannes A. Lercher for giving me the possibility to join his research group and guidance throughout my studies. It has been a wonderful and challenging time and I thank you for all the effort, support and especially trust from your side.
Special thanks goes to my advisor Andreas Jentys for his continuous support throughout the time. Andy, you were always honest, critical and kept myself up to consistently question and reflect my work. Thank you for the continuous support over the last 3 years.
I would like to thank all my collaborators in the BMBF iC^4 AdCOO project (01RC1106A) for fantastic 3 years and so many fruitful discussions and successful cooperation: Andreas Geisbauer and Richard Fischer from Clariant, Bernhard Rieger, Karsten Reuter and Jelena Jelic from TUM and Henning Schramm from Siemens. I further like to thank Wolfgang A. Herrmann, Kai-Olaf Hinrichsen and Johann Plank for access to experimental equipment.
There have been a lot of colleagues working in the field of CO_2 capture that I have to thank. First I would like to thank Edith Berger for a continuous and very successful collaboration. I especially want to thank Pamina Bohn and Yulia Martynova for their contribution to the basic understanding of the adsorption processes.
Moreover, I would like to thank my former students Matthias Steib and Andreas Berger for their significant scientific collaboration during their Master's studies in our group. I am also very grateful for the contribution of my students all over the last years: Moritz Wolf, Andreas Hilger, Katrin Holzwarth, Korina Hartman, Jürgen Hajdo, Florian Franz, Ferdinand Vogelgsang, Florian Obergruber and especially Christian Scherer.
A special thanks goes to my parents Rudi and Lis for being very patient with me all over the years. Thanks for your support and all the love over the years.
There have been a lot of people that always have been a great support. I especially want to thank Alex Kern, Jan Borchers, Jens Bosse Parra, Benno Jering, Julia Klinger, Dennis Kirpensteijn and Kevin Milsztein.
Last but not least I thank all my colleagues, office mates and peeps who made this last 3 years so special. At this point I would like to especially name Christian Gärtner, Linus Schulz, Stanislav Kasakov, Sebastian Foraita, Peter Hintermeier, Elisabeth Hanrieder and Sylvia Albersberger.

Abstract

Abstract

The following thesis addresses the need for the development and implementation of adsorbents required for sustainable CO_2 capture process. The concept of hierarchically structured sorbents is a promising candidate for the newly developed capture processes oxy-fuel and pre-combustion that require abrasion-resistant sorbents with selective CO_2 adsorption at high pressures. In contrast, strong chemisorption is essential to sorbents applicable for low CO_2 partial pressures in post-combustion CO_2 capture. The presented investigations in the design of solid amine functionalized sorbents are fundamental in the understanding of amine interaction that are necessary for the development of highly efficient adsorbents for ambient CO_2 capture. H_2O is the main by-product of atmospheric combustion of fossil fuels. Thus, the impact of H_2O on the kinetics and thermodynamics of the CO_2 adsorption on amine impregnated sorbents is systematically explored, referring to changes in the adsorption mechanism.

Kurzfassung

In den folgenden Kapiteln wird die Entwicklung und Eignung von neuartigen Adsorbentien in einem nachhaltigen Prozess zur CO_2 Abtrennung diskutiert. Der Ansatz hierarchisch strukturierter Adsorbentien ist insbesondere für die neu entwickelten Abtrennungsprozessen Oxy-Fuel sowie Pre-Combustion geeignet. Hierbei sind insbesondere eine Abriebsfestigkeit und hohe CO_2 Selektivitäten unter Hochdruck wichtigere Kriterien für die Auswahl der Adsorbentien. Im Gegensatz hierzu ist eine stärkere Bindung des Adsorbats mittels Chemisorption notwendig, für die Abtrennung bei niedrigen CO_2 Partialdrücke (Post-Combustion). Die hierdurch gewonnenen Erkenntnisse, über den Aufbau aminfunktionaliserter fester Adsorbentien, erweitern grundlegend das Verständnis von Aminwechselwirkungen, die maßgeblich für die Entwicklung von effizienten Adsorbentien beitragen. H_2O ist das am stärksten anfallende Nebenprodukt der atmosphärischen Verbrennung fossiler Brennstoffe. Daher wurde speziell der Einfluss von H_2O auf den CO_2 Adsorptionsmechanismus aminfunktionaliserter Sorbentien in Bezug auf Kinetik und Thermodynamik untersucht.

Table of Contents

List of Figures

List of Schemes

List of Tables

List of Abbreviations

AAMS	N-[3-(trimethoxysilyl)propyl]ethylendiamine
APTMS	(3-aminopropyl)trimethoxy-silane
BET	Brunauer-Emmett-Teller
BJH	Barret-Joyner-Halenda
DETA	Diethylenetriamine
DSC	Differential scanning calorimetry
ICP OES	Inductively coupled plasma optical emission spectrometry
IR	Infrared spectroscopy
MAPS	N-methyl-3-aminopropyl-trimethoxysilane
PEI	Polyethyleneimine
ppm	Parts per million
PSA	Pressure swing adsorption
PTMS	Phenyltrimethoxysilane
SEM	Scanning electron microscopy
TCD	Thermal conductivity detector
TEOS	Tetraethylorthosilicate
TEPA	Tetraethylenepentamine
TG	Thermogravimetry
TSA	Temperature swing adsorption
XRD	X-ray diffraction

1 Introduction

With the rapid proceeding of the industrialization in Europe, the worlds energy demand drastically emerged over the centuries. Ever since, the CO_2 output and the gross domestic product (GDP) of an industrialized country are strongly connected. Because the anthropogenic CO_2 concentration has increased over the last decades, it is necessary to control and decrease CO_2 emissions.[1] Investments in alternative energies such as wind and solar energy, as well as biomass-derived fuels, are crucial in the path to limit further growth of non-renewable energy resources.[2] However, the costs associated with the decentralized structure of renewable energy and the strong fluctuations in availability lead to significant challenges to steadily cover the high energy demand of industrialized countries.[2,3]

Technological barriers of biomass derived fuel production and solar energy still hinder a combined sustainable approach to gain industrial relevance on a larger scale.[4–7] Electro mobility is likely to have a significant impact on the transportation sector and might even displace the need of liquid fuels.[8] Nevertheless, fuel cells and batteries require vast amounts of novel and rare earth metals and an economical, environmentally friendly production of hydrogen could not yet be achieved.[9–12] Overall, fossil fuels are still inevitable to cover the major energy demand and therefore have to be included in the reduction of CO_2 emissions worldwide. Oil, gas, and coal, are the backbone of our energy consumption and will remain dominating far out into the future.[3,4,13] Furthermore, the low societal acceptance of nuclear energy[14] have led to the renaissance of gas and coal as dominating fossil carbon sources, varying in importance as direct consequence of the local availability.[15] Especially the recent developments in the extraction of gas and oil from previously inaccessible reservoirs (enhanced oil recovery) dictate particular efforts to achieve a sustainable CO_2 capture to limit the impact on the greenhouse effect.[16,17]

Worldwide efforts to decrease the emission of CO_2 create the necessity of controlling especially the emissions from coal-fired power plants that represent the largest stationary emitters of greenhouse gases to the atmosphere.[18–20] Post combustion capture (PCC) processes with an aqueous solution of monoethanolamine (MEA) are state of the art for the use in enhanced oil recovery (EOR) since the 1970s.[21] Nevertheless, the adsorption capacities that are required for a modern coal-fired power plant by far exceed the separation capacity of these early processes.[22,23] The currently practiced separation of CO_2 from flue gas stream with a PCC amine wash decreases the effectiveness of a coal-fired power plant by 10 - 12 %.[24] Additionally to the initial investment costs of a CO_2 separation unit, operating costs of approximately 60 dollars per ton of CO_2 have to be taken in account for a standard 30 wt.% monoethanolamine (MEA) scrubbing capture

process.[25] The major contributions to the cost of the amine wash based PCC are the degeneration of the amine and the energy intensive desorption step, reflecting the high heat capacity of the aqueous amine solution ($c_p(H_2O) = 4.18\,kJ\,kg^{-1}\,K^{-1}$).[26,27] Thus, the development of amine impregnated solid sorbents that possess lower heat capacity (e.g. $c_p(SiO_2) = 0.8\,kJ\,kg^{-1}\,K^{-1}$)[28] has been in the focus of various research groups.[29–36] Direct grafting to create supported aminosilanes incurs costly synthesis that limits an economical industrial application.[37,38] Therefore, the use of solid sorbents impregnated with amines is still the economically most promising option.

Alternatively, more effective processes are also being explored that include gas separation directly in the process.[39] Exemplarily, pre-combustion and oxyfuel processes are high pressure and high temperature processes using a highly enriched oxygen stream from which CO_2 has to be separated from H_2 (pre-combustion) or H_2O (oxyfuel).[39,40] Implementation of such a process not only requires new reactor engineering approaches, but also the development of cost effective adsorbents, well-adjusted to the new separation conditions.[41] Large pore volumes and surface areas are more applicable for the high pressure CO_2 capture than chemisorption that is the most suitable route for CO_2 capture at ambient pressures. Zeolites and MOFs are among the most promising candidates that are widely studied. Integrated processes are still in the early research state and therefore require tremendously higher investment costs compared to retrofitted PCC.[42,43]

The following chapters focus on the adsorption of CO_2 on solid sorbents being the specific target of the iC^4 AdCOO project. The BMBF iC^4 project is devided in CO_2 capture, AdCOO and COOMem (membrane separation), and conversion, COOMeth (methanisation) and PhotoCOO (photocatalysis), as illustrated in Figure 1.1 below.

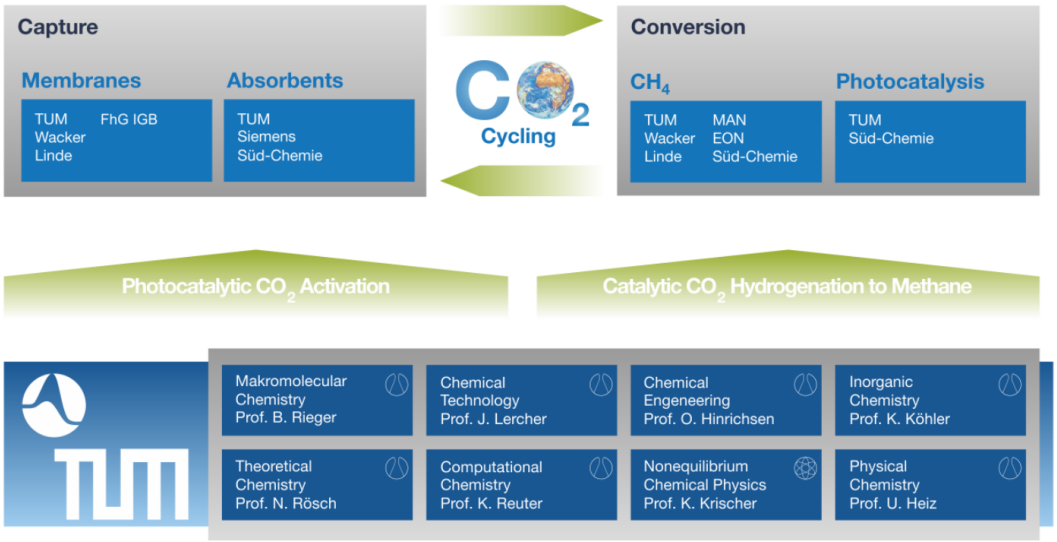

Figure 1.1: Structure of the BMBF iC^4 project.

The applicability of novel, hierarchically structured sorbents for high pressure CO_2 adsorption (pre-combustion, oxy-fuel) is investigated in Chapter 2. Furthermore, Lewis basic Zr^{4+} cations were added to the structure of the sorbents to enhance CO_2 capture and stability at high pressures. Chapter 3 and Chapter 4 focus on atmospheric CO_2 adsorption via solid, amine-functionalized sorbents that are most suited for post-combustion capture. The impact of the functionality and concentration of amines groups on the capture mechanism, CO_2 uptake and long term stability is discussed in Chapter 3. H_2O is the main by-product of atmospheric combustion of fossil fuels and therefore is crucial to be included in the industrial application of adsorbents. A kinetic and thermodynamic study of solid, amine-functionalized sorbents under the presence of H_2O vapor is presented in Chapter 4.

The industrial realization of all discussed capture processes will strongly depend on the utilization of CO_2 as the main contaminant of the flue gas stream (by volume %).[25,44] The conversion of H_2 and CO_2 over a Ni catalyst to CH_4 and H_2O (Sabatier reaction) is particularly interesting, because the storage of CH_4 is less expensive compared to H_2 and also allows the utilization of the existing natural gas network.[45–47] Moreover, high pressure CO_2 can also be directly used for EOR and the purity of CO_2 gas composition has much lower requirements compared to the utilization in the Sabatier process.[48–50] The necessity to convert and utilize CO_2 is further addressed in the COOMeth and PhotoCOO project as part of the iC^4 cluster and is not discussed in this thesis.

2 Tailoring Hierarchically Structured SiO_2 Spheres for High Pressure CO_2 Adsorption

2.1 Abstract

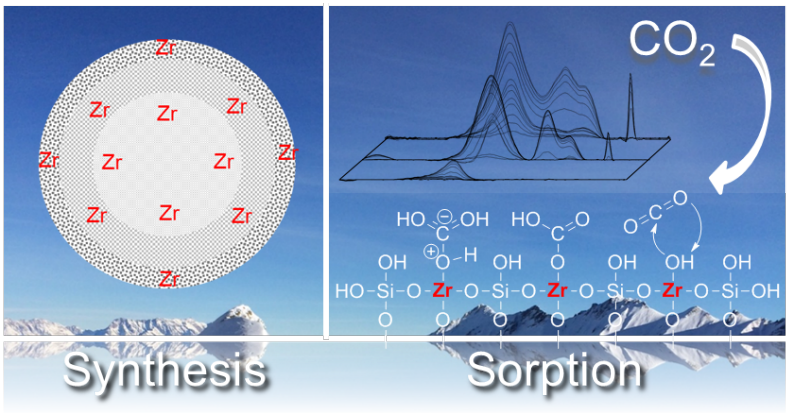

The synthesis, characterization, and experimental validation of hierarchically structured, millimeter-sized SiO_2 spheres with high CO_2 uptake capacities has been systematically explored.[1] The solvents employed during synthesis (aniline, benzyl alcohol and butanol) of the silica structures from alkoxisilanes strongly influence the physicochemical properties by controlling hydrolysis and condensation rates. The new sorbents possess specific surface areas up to $660\,m^2\,g^{-1}$ and a hierarchically ordered mesoporous/macroporous pore structure. The SiO_2 spheres showed lower heats of adsorption of CO_2 (8 - 17 $kJ\,mol^{-1}$) compared to the benchmark zeolite 13X, facilitating the desorption of CO_2 in temperature swing adsorption applications. Moreover, the CO_2 adsorption isotherms of SiO_2 spheres are less steep compared to zeolite 13X resulting in an increased CO_2 uptake capacity in pressure swing adsorption processes. Addition of Zr^{4+}cations to SiO_2 increases the CO_2 uptake by generating Lewis acid-base sites. Because the presence of Zr^{4+} in the structure also dramatically enhances the abrasion resistance of the sorbents, additional coagulation steps, required for the benchmark sorbents, are not necessary.

[1] This chapter is based on the article of the same title as appeared in the Journal of Material Chemistry A. The Royal Society of Chemistry gave approval to non-commercially reproduce the article (DOI: 10.1039/C4TA02145B) both in print and online.

2.2 Introduction

Adsorbents for pre-combustion are currently intensely investigated.[41,51–54] Exemplarily, Schell et al. investigated the adsorption equilibrium of CO_2 and H_2 on MCM-41 and metal organic framework (MOF) USO-2-Ni at different temperatures up to 140 °C and at pressures up to 150 bar.[53] However, the time-intensive synthesis in combination with high costs is a major drawback of these materials (MCM-41, SBA-15 and MOF).[55–58] This is related with the fact that the synthesis of the materials and the forming step are separated requiring several preparation steps.

In contrast, emulsion based, biphasic chemistry allows to control the shape and mesostructure during material synthesis in one step.[59] Huo et al. synthesized mesoporous SiO_2 spheres synthesized similar to MCM-41 with a diameter of 0.5 - 1 mm in a one-step procedure.[60] These SiO_2 spheres exhibited 2 nm pores and specific surface areas up to 1100 $m^2\,g^{-1}$.[60] Nevertheless, the pore volumes of the SiO_2 spheres were only in the range of 0.24 - 0.54 $ml\,g^{-1}$ limiting the maximum CO_2 storage capacity. The larger, hierarchically structured, millimeter sized SiO_2 spheres (in the range of 1 -2 mm), which were recently developed as sorbents and catalyst supports offer advantages compared to the former materials with respect to pore volume and pore size distribution.[61–64] The surface of the SiO_2 spheres is dominated by large pores allowing fast access of CO_2 from the gas phase into the sorbent, followed by a mesoporous inner part enabling high CO_2 sorption capacities (Figure 2.1).[62–64]

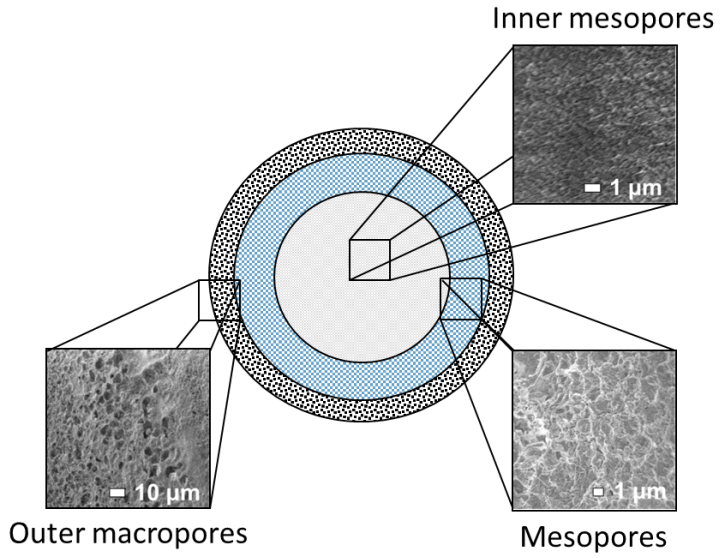

Figure 2.1: Proposed structure of SiO_2 spheres according to Scholz et al..[62,64]

The sorption process of these materials was found to be not kinetically limited due to fast transport in the mesopores and relatively small domains of microporous SiO_2. It should be noted that with increasing pressure, the regime changes from Knudsen to bulk

diffusion and therefore film diffusion is assumed to be the rate determining step, if transport limitations occur. High specific surface areas and well-ordered pore structures make the hierarchically structured SiO_2 spheres a promising alternative to zeolites, mesoporous silicates and MOFs for high pressure pre-combustion applications.

In this study, we investigate the influence of three solvents (aniline, benzyl alcohol, and butanol) with comparable density on the morphology of mesoscopic, hierarchically structured SiO_2 spheres for pre-combustion CO_2 separation (Scheme 2.1). The difference in polarity of the solvents influenced the rate of hydrolysis, whereas the different basicity of the solvents directly affected the condensation reactions in the sol-gel process (Scheme 2.2). In part of the samples, Zr^{4+} cations were incorporated in the SiO_2 framework to enhance the interaction with CO_2 and increase separation from H_2. The uptake of CO_2 and N_2 (selected instead of H_2 as a non-explosive probe molecule) was investigated up to a pressure of 40 bar at two different temperatures. Thermodynamic parameters (ΔH_{ads}, ΔS_{ads}) were calculated using the Langmuir adsorption model. The structural and physicochemical properties of the adsorbents were investigated to derive structure activity relationships.

Scheme 2.1: Hydrolysis and condensation reactions during synthesis of SiO_2 spheres.

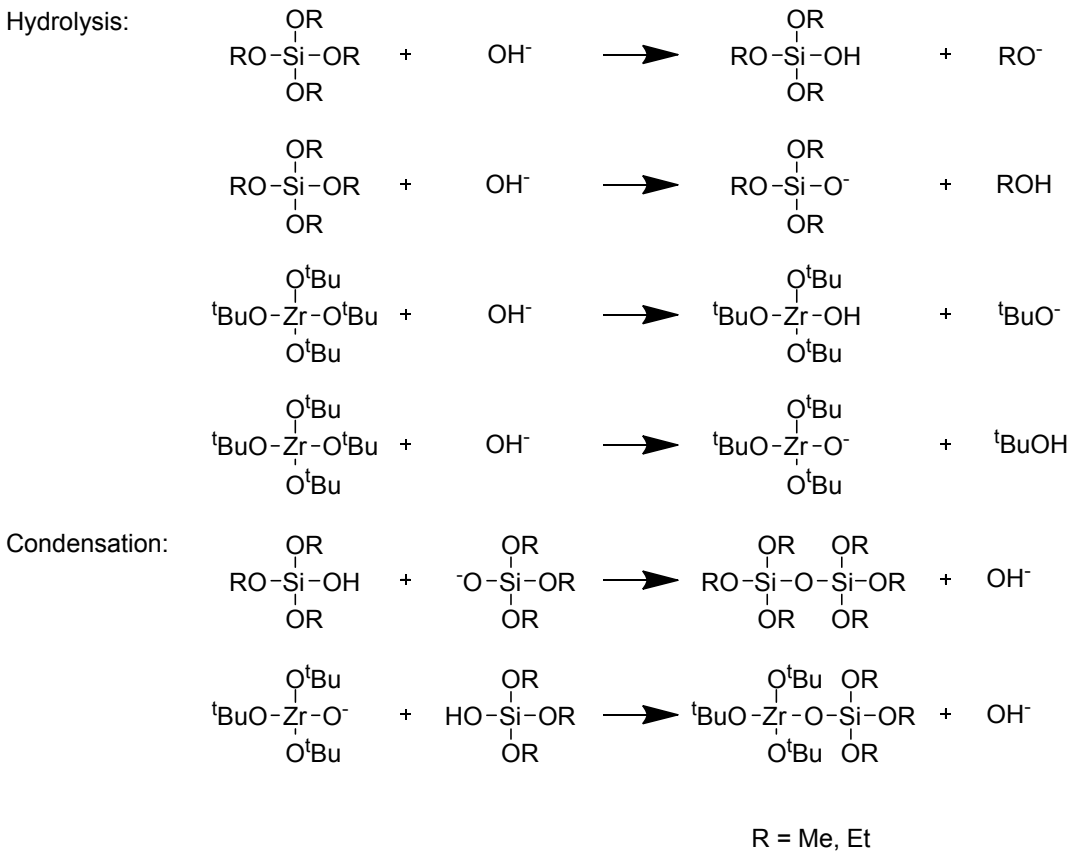

Scheme 2.2: (a) Structure directing compounds, (b) solvents and (c) proposed coordinative structure prior to calcination.

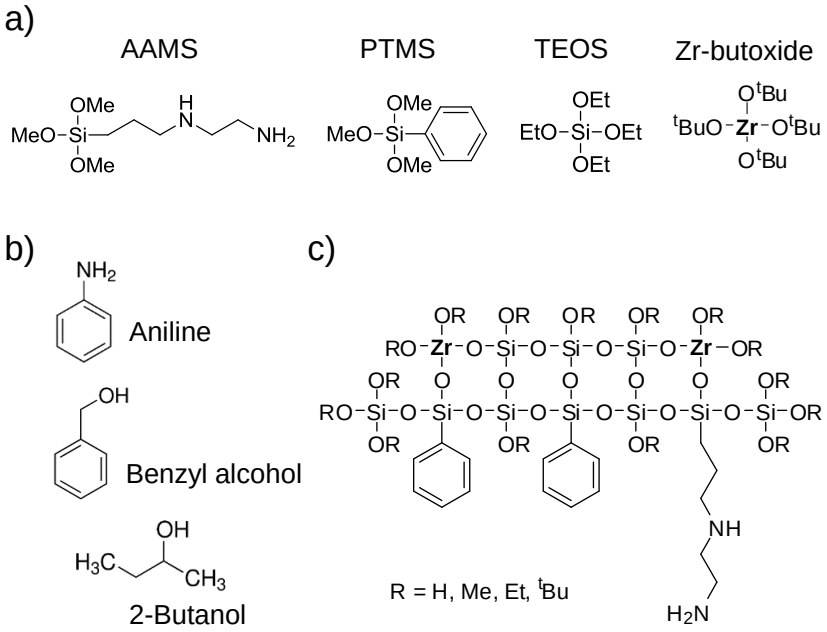

2.3 Results and Discussion

2.3.1 Impact of the Solvent on Structural Properties and CO_2 Physisorption

The influence of the pH on the hydrolysis and condensation in sol-gel processes has been widely discussed over the last decades.[65–68] The pK_a values of the solvents used decrease in the order of aniline (30.6), 2-butanol (17.0) and benzyl alcohol (15.4), inducing a strong dependence of the hydrolysis and condensation rates.[69–71] Under acidic conditions, the sol-gel process is dominated by a fast rate of hydrolysis, resulting in a high degree of branching,[66] while condensation is most prominent for a pH above 7 leading to a linear structure of the gel.[66] The pH of the precursor solution was in the basic region for all three solvents (aniline: 11.36, butanol: 11.00, benzyl alcohol: 10.64), because it was mainly controlled by the presence of the primary and secondary amine AAMS. A decrease in pH in this range slows down primarily the rate of hydrolysis rather than the condensation rate (see Equations below).

$$r_{hydrolysis} = k_{hydrolysis} \cdot [\mathrm{TEOS}] \cdot [\mathrm{OH^-}] \tag{2.1}$$

$$r_{condensation} = k_{condensation} \cdot [\mathrm{TEOS}_{hydrated}]^2 \tag{2.2}$$

$$\frac{d[\mathrm{TEOS}_{hydrated}]^2}{dt} = r_{hydrolysis} - r_{condensation} \approx 0 \tag{2.3}$$

$$[\mathrm{OH^-}] = \frac{k_{condensation}}{k_{hydrolysis}} \cdot \frac{[\mathrm{TEOS}_{hydrated}]^2}{[\mathrm{TEOS}]} \tag{2.4}$$

$$[\mathrm{H^+}] = \frac{K_w \cdot k_{hydrolysis}}{k_{condensation}} \cdot \frac{[\mathrm{TEOS}]}{[\mathrm{TEOS}_{hydrated}]^2} \qquad \text{with} \qquad [\mathrm{H^+}] \cdot [\mathrm{OH^-}] = K_w \tag{2.5}$$

$$pH = -\log\left[\frac{K_w \cdot k_{hydrolysis}}{k_{condensation}} \cdot \frac{[\mathrm{TEOS}]}{[\mathrm{TEOS}_{hydrated}]^2}\right] \tag{2.6}$$

Assuming stationary conditions for the concentration of the hydrated TEOS, a lower pH increases the concentration of the non-hydrated form of TEOS. Therefore, the overall rate of the formation of the solid gel was retarded, which favors the formation of a linear chain structure in the final polymerized material.The micro-, meso- and macropore volumes of the SiO_2 spheres are illustrated in Figure 2.2.

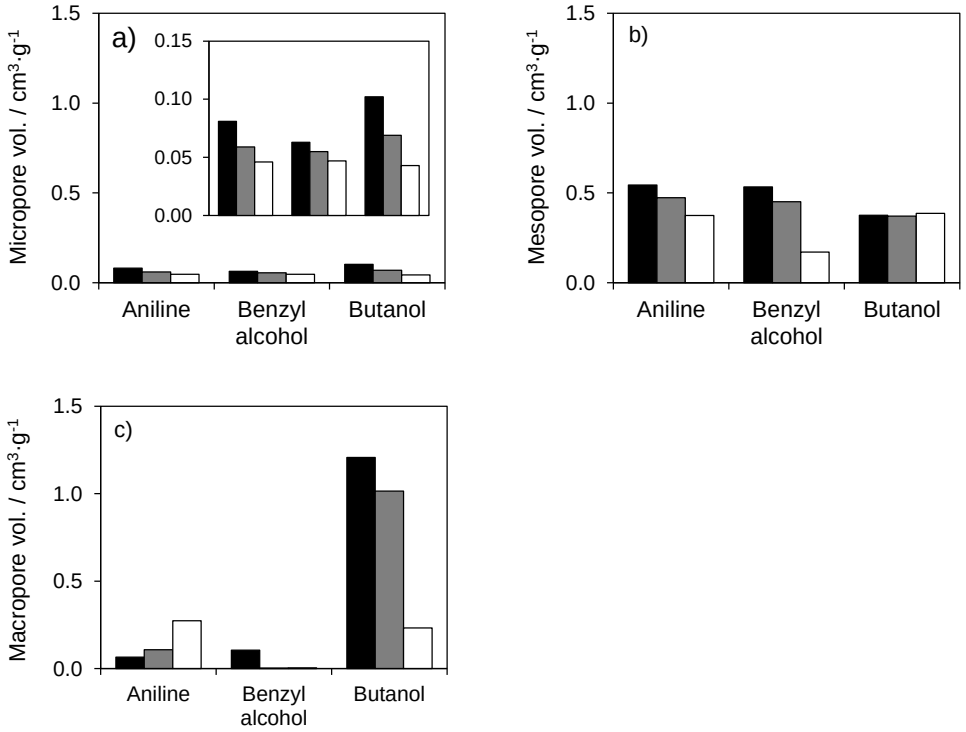

Figure 2.2: Micro[a] (a), meso[a] (b) and macro[b] (c) pore volume of aniline, benzyl alcohol and butanol Zr(0) (black), Zr(1) (grey) and Zr(7) (white). [a] Determined by N_2 physisorption, [b] determined by Hg porosimetry.

For further assignment, SiO_2 spheres are denoted as aniline, benzyl alcohol and butanol spheres dependent on the solvent employed during synthesis. Whenever a specification is required, SiO_2 spheres without incorporated Zr^{4+} are denoted as aniline, benzyl alcohol and butanol Zr(0). The micropore volume of all SiO_2 spheres was lower than the mesopore volume (Figure 2.2 a, b). A significant contribution of macropores was only observed for butanol Zr(0) (Figure 2.2 c). The mesopore volume was lower for butanol Zr(0) compared to aniline and benzyl alcohol Zr(0), due to pronounced hydrolysis leading to a more branched and less-defined mesopore distribution. The most significant impact on the rate of hydrolysis was, however, achieved via the solubility of the solvent in water, surrounding the micelle. It should be noted that two H_2O molecules are needed for the hydrolysis, which will later be regained in the condensation. The solubility of the solvents in water decreased in the order butanol ($125\,g\,L^{-1}$), benzyl alcohol ($40\,g\,L^{-1}$) and aniline ($36\,g\,L^{-1}$).[72] Thus, the solvents aniline and benzyl alcohol allow only a modest exchange of water and solvent via the surfactants on the outer side of the micelle and lead to very controlled hydrolysis. In contrast, *2*-butanol allows a rapid exchange of water molecules via the interface due to its high solubility in water, resulting in an accelerated hydrolysis.[60] Additionally, the strong diffusion gradient results in the formation of large channels, mainly in the interface layer that form macropores after calcination (Figure 2.2 c). The BET surface areas and the pore size distributions of the adsorbents are displayed as a function of the solvent and their Zr^{4+} content in Figure 2.3 and 2.4, respectively.

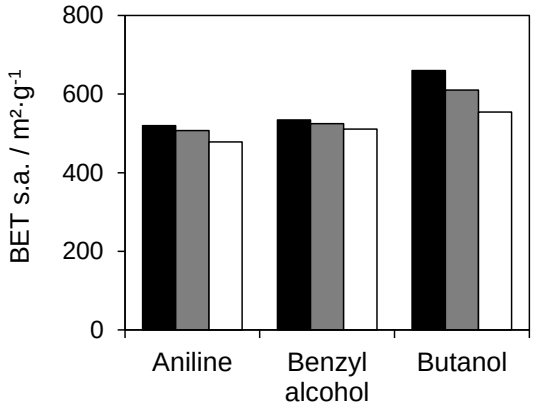

Figure 2.3: BET surface area of aniline, benzyl alcohol and butanol Zr(0) (black), Zr(1) (grey) and Zr(7) (white).

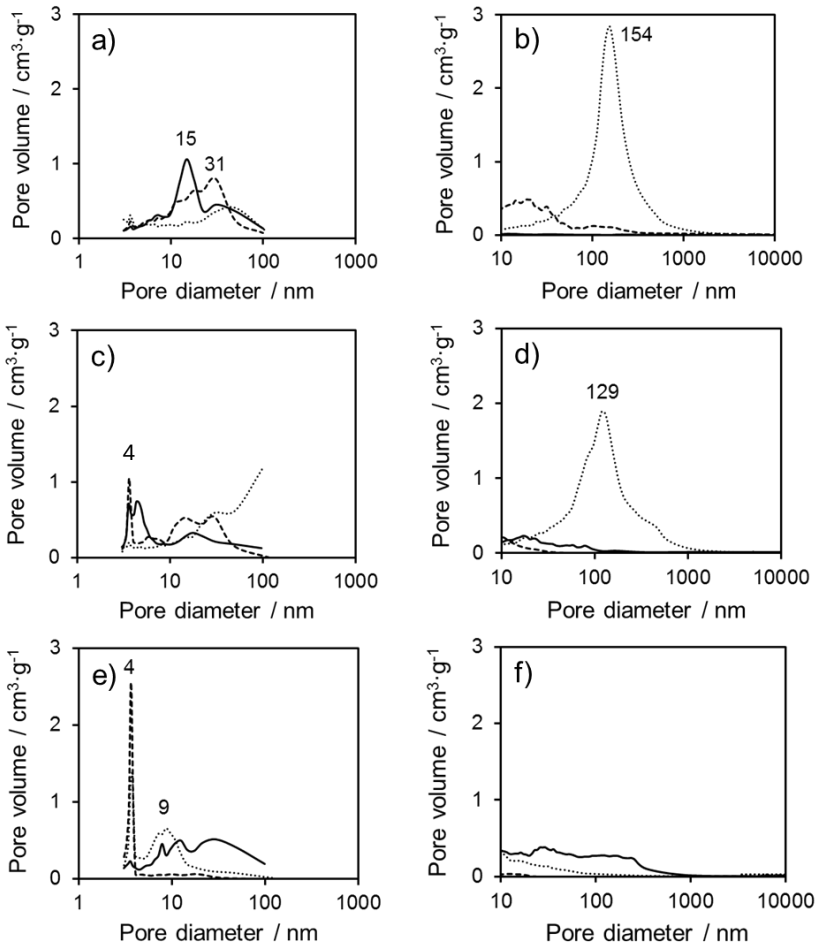

Figure 2.4: Pore size distribution of aniline (solid line), benzyl alcohol (dashed line) and butanol (dotted line) Zr(0) (a - b), Zr(1) (c - d) and Zr(7) (e - f) determined by N_2 physisorption (a, c, e) and Hg porosimetry (b, d, f).

The large contribution of macropores of butanol spheres leads to a high BET surface area ($660\,m^2\,g^{-1}$). SiO_2 spheres synthesized with aniline and benzyl alcohol show similar specific surface areas and mesopore volumes, because the solubility of these solvents in water is approximately identical. The micropore volume of the SiO_2 spheres correlates with the basicity of the solvent and was most pronounced for the solvent with the highest pK_a (Figure 2.2 a). The mesopore size distribution has a maximum at a larger diameter for benzyl alcohol Zr(0) (31 nm) compared to those prepared with aniline Zr(0) (15 nm), due to the slightly enhanced condensation rate because of the higher basicity of aniline (Figure 2.4 a). The CO_2 and N_2 sorption isotherms of the various SiO_2 spheres are compiled in Figure 2.5 and the according maximum uptakes are reported in Table 2.1.

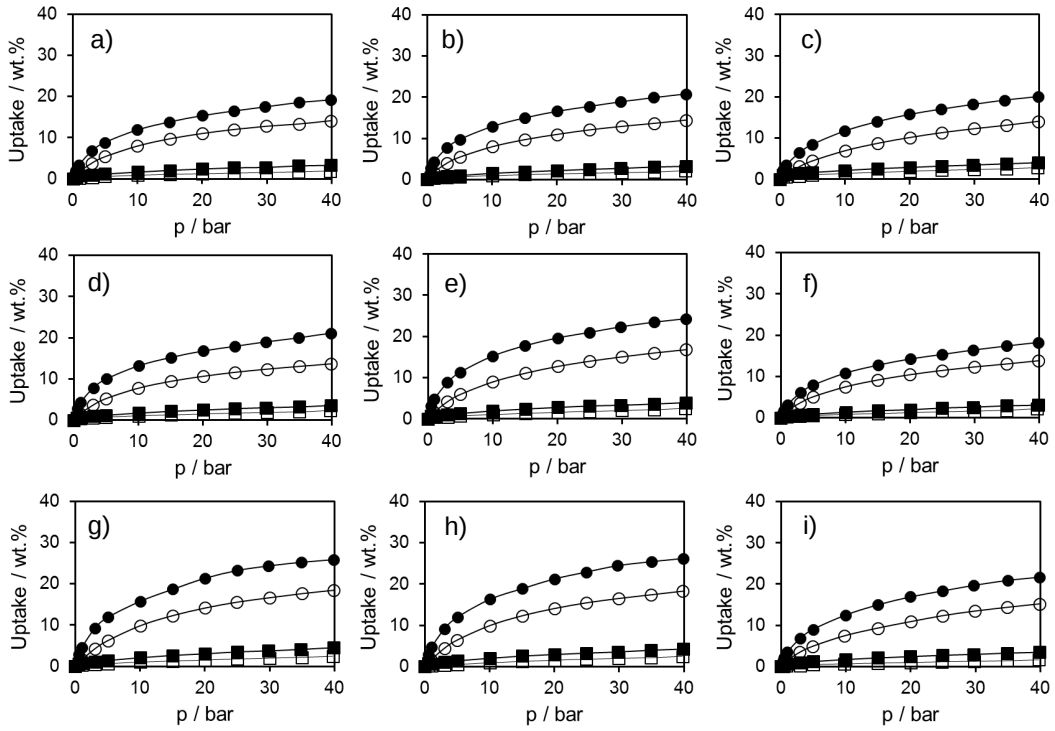

Figure 2.5: CO_2 adsorption (circles) and N_2 adsorption (squares) at 35 °C (filled symbols) and 70 °C (unfilled symbols). (a - c) Aniline, (d - f) benzyl alcohol and (g - h) butanol Zr(0) (a, d, g), Zr(1) (b, e, h) and Zr(7) (c, f, i).

Similar CO_2 adsorption characteristics were observed for aniline Zr(0) and benzyl alcohol Zr(0) (Figure 2.5 a, d). The slightly higher CO_2 uptake at 40 bar and 35 °C of benzyl alcohol Zr(0) is concluded to be a consequence of the higher surface area and micropore volume in comparison to aniline Zr(0) ((Table 2.1), Figure 2.2 a, b). Nevertheless, the CO_2 uptake at 70 °C of both sorbents showed only a negligible difference (Table 2.1).The most significant difference in the CO_2 uptake was observed for butanol Zr(0), exhibiting an increased CO_2 uptake capacity already at partial pressures below 20 bar, almost doubling the heats of adsorption compared to aniline Zr(0) (Figure 2.5, see (Table 2.2 for ΔH_{ads}). The enhanced CO_2 capacity of butanol Zr(0) is attributed to the highest surface area of all SiO_2 spheres resulting from the defined macroporous structure (Figure 2.2 a, c).

Please note that the mean free path length of CO_2 at 20 bar pressures is on the order of approximately 2 nm, which implies that the transport of CO_2 is in the regime of bulk diffusion and therefore pore diffusion limitations can be excluded inside the macropores that are 154 nm in diameter (Figure 2.4 b).

Table 2.1: CO_2 and N_2 uptake at 35 °C and 70 °C at 40 bar.

	CO_2 / wt.%		N_2 / wt.%	
	35 °C	70 °C	35 °C	70 °C
SBA-15	32.4	21.7	4.2	3.5
Zeolite 13X	32.5	25.6	7.5	4.9
Aniline Zr(0)	19.2	14.1	3.3	1.9
Aniline Zr(1)	20.8	14.4	3.2	2.2
Aniline Zr(7)	20.1	14.1	4.0	2.8
Benzyl alcohol (0)	21.1	13.7	3.5	2.3
Benzyl alcohol (1)	24.3	16.8	3.9	2.5
Benzyl alcohol (7)	18.3	13.8	3.0	2.2
Butanol (0)	32.5	18.4	4.5	2.4
Butanol (1)	32.5	18.3	4.2	2.5
Butanol (7)	32.5	15.2	3.5	1.6

Table 2.2: Heats of adsorption (ΔH_{ads}) and entropy (ΔS_{ads}) of the adsorption of CO_2 obtained by the Langmuir adsorption model.

	$\Delta H_{ads}(CO_2)$ / kJ mol^{-1}	$\Delta S_{ads}(CO_2)$ / J mol^{-1} K^{-1}
SBA-15	-8.6	-55.5
13X	-29.5	-86.0
Aniline Zr(0)	-9.3	-47.7
Aniline Zr(1)	-12.3	-56.9
Aniline Zr(7)	-15.4	-69.3
Benzyl alcohol Zr(0)	-12.8	-56.8
Benzyl alcohol Zr(1)	-16.8	-71.6
Benzyl alcohol Zr(7)	-7.7	-43.9
Butanol Zr(0)	-17.6	-74.2
Butanol Zr(1)	-16.0	-68.8
Butanol Zr(7)	-13.3	-62.9

2.3.2 Enhanced CO_2 Chemisorption and Structural Effects by Incorporation of Zr^{4+}

Zr^{4+} cations were incorporated in the SiO_2 spheres with approximately 1 wt.% (5 wt.% zirconium(IV) t-butoxide) and 7 wt.% (25 wt.% zirconium(IV) t-butoxide) (Table 2.3). In accordance to the pure adsorbents, the Zr^{4+} containing SiO_2 spheres are subsequently denoted as aniline, benzyl alcohol, butanol Zr(1) and Zr(7).

Table 2.3: Zr elemental analysis of SiO_2 spheres.

	Zr/wt.%
Aniline Zr(1)	1.17
Aniline Zr(7)	6.3
Benzyl alcohol Zr(1)	1.15
Benzyl alcohol Zr(7)	7.2
Butanol Zr(1)	1.19
Butanol Zr(7)	7.0

Addition of 25 wt.% zirconium(IV) *t*-butoxide (based on TEOS) to the precursor solution resulted in an instant drop of pH by approximately 0.2 for all precursor solutions independently of the solvent used. The full hydrolysis of zirconium(IV) *t*-butoxide, and the subsequent formation of more than four-coordinated Zr^{4+} complexes in an alkaline environment, results in the net consumption of hydroxyl groups and therefore a decrease in pH. Because the overall content of zirconium(IV) *t*-butoxide is rather low compared to the other silanes, cross-condensation is most likely favored over self-condensation. Moreover, in contrast to acid catalyzed hydrolysis, the hydrolysis rate increased with every additional hydrolysis per molecule.[68,73] Thus, zirconium(IV) *t*-butoxide leads to an accelerated hydrolysis of all alkoxides and, therefore, to a higher degree of crosslinking inside the SiO_2 particles due to the formation of pre-condensed units leading to significant decline in the accessibility of the pores of the SiO_2 spheres, independently of the solvent used.[66]

The marked decrease of the macropore volume from 1.207 to 0.233 $cm\,g^{-1}$ upon incorporation of 7 wt.% Zr^{4+} in SiO_2 spheres synthesized with butanol is shown in Figure 2.4. No defined macroporous structure was observed for benzyl alcohol SiO_2 spheres (Figure 2.4 b, d, f).

The macropore volume of aniline spheres increased with an increasing Zr^{4+} content, but still remained moderate without a defined distribution (Figure 2.4 b, d, f). Aniline and benzyl alcohol SiO_2 spheres underwent a significant decrease in mesopore volume from 0.544 to 0.374 $mL\,g^{-1}$ and 0.533 to 0.170 $mL\,g^{-1}$ with 7 wt.% Zr^{4+}. (Figure 2.2 b). Significant changes were not observed when Zr^{4+} was inserted in butanol SiO_2 spheres, because only a small percentage of macropores was transformed into mesopores for higher Zr^{4+} contents ((Figure 2.2 b). Increasing the Zr^{4+} content of aniline spheres also resulted

in a decrease of the mesopore size, whereas butanol Zr(1) and Zr(7) mainly retained an undefined structure (Figure 2.4 a, c, e). The mesopore size distribution of benzyl alcohol Zr(1) and Zr(7) spheres narrowed down drastically to approximately 4 Å (Figure 2.4 c, e). Incorporation of Zr^{4+} in aniline and benzyl alcohol SiO_2 spheres only resulted in a minor decline of BET surface areas, whereas the decrease was more obvious for butanol Zr(1) and Zr(7) (660 - 554 $m^2\,g^{-1}$) due to a strong collapse of the macroporous structure (Figure 2.3, Figure 2.4 f).

The X-ray diffractograms of all SiO_2 spheres showed only one broad peak at $2\Theta = 25°$ and sharp reflections were not observed (Figure 2.6). The diffractograms remained unchanged after incorporation of Zr^{4+} in the framework, which indicates that crystalline ZrO_2 domains with long-range order were absent.[73] Therefore, we conclude that Zr^{4+} cations were dispersed in the silica structure.

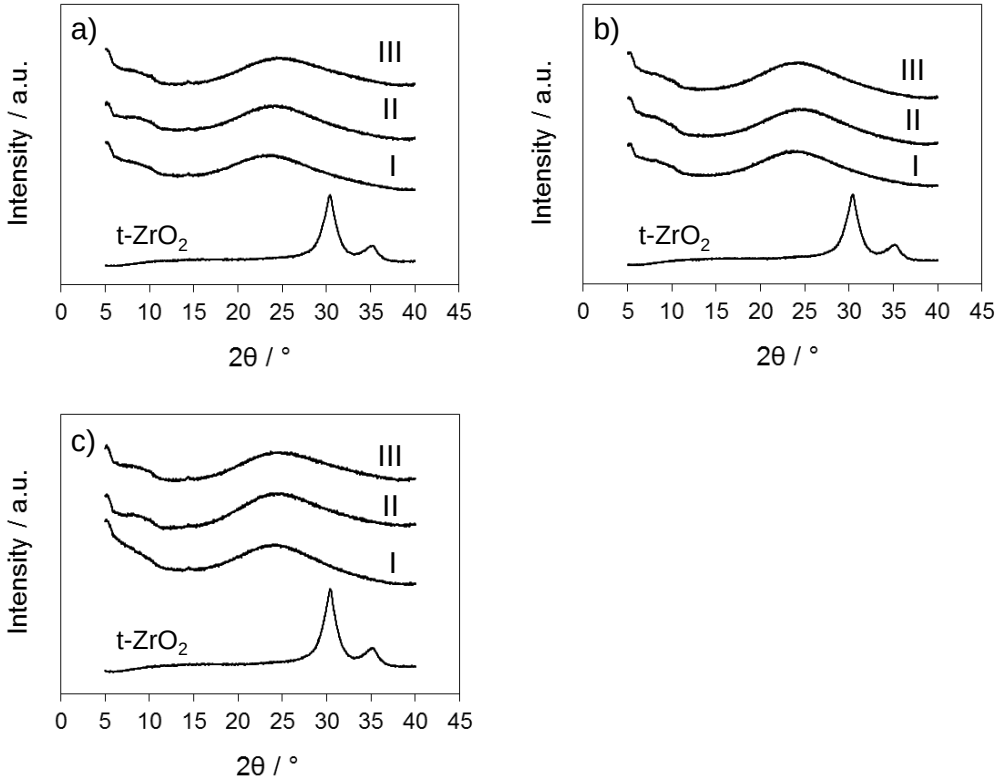

Figure 2.6: XRD of t-ZrO_2, (a) aniline, (b) butanol and (c) benzyl alcohol Zr(0) (I) , Zr(1) (II) and Zr(7) (III).

The SEM images of aniline, benzyl alcohol and butanol spheres with 0, 1 and 7 wt.% Zr^{4+} are shown in Figure 2.7. An undefined increase in pore size was observed by SEM for aniline SiO_2 spheres synthesized with aniline, when zirconium(IV) *t*-butoxide was added to the precursor solution. The loss of a defined pore structure pore structure for benzyl alcohol and butanol SiO_2 spheres synthesized with benzyl alcohol and butanol upon incorporation of 7 wt.% Zr^{4+} was observed. An ordered macroporous structure was solely observed for

spheres synthesized with butanol spheres at Zr^{4+} concentrations up to 1 wt.% (Figure 2.7) that was in accordance with the results of the macropore volume distribution (Figure 2.2, Figure 2.4).

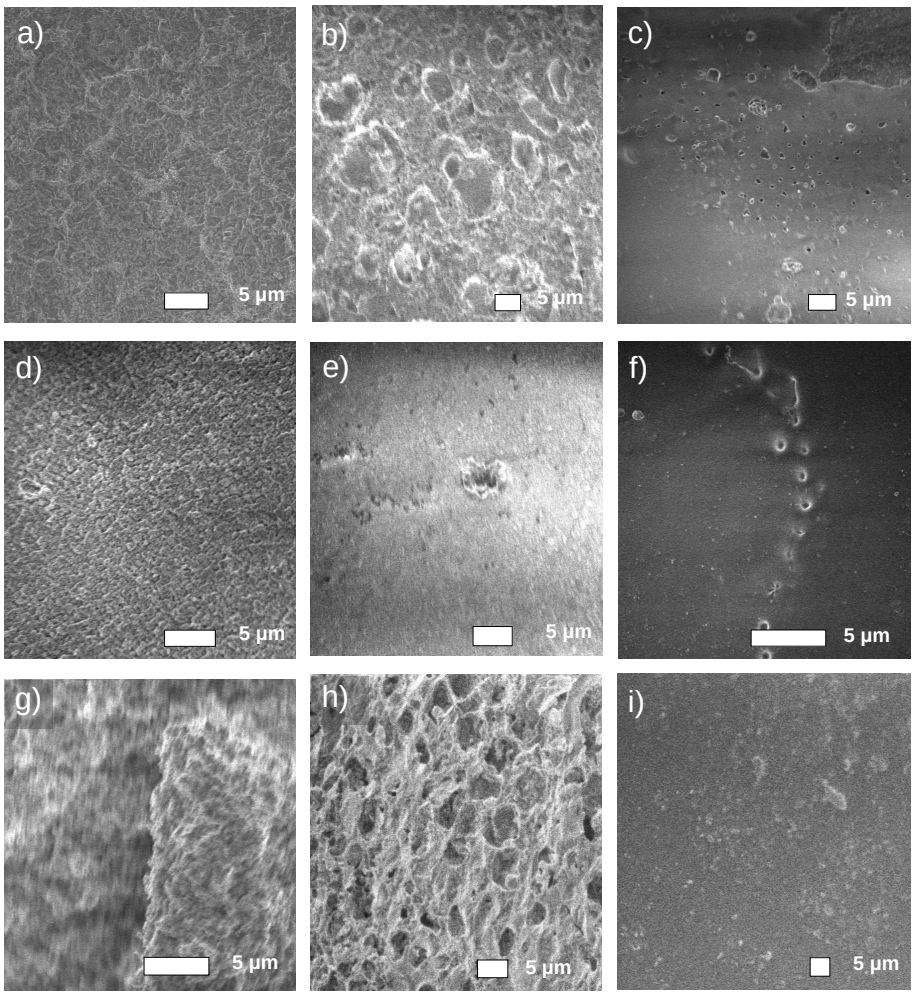

Figure 2.7: SEM images of (a - c) aniline, (d - f) benzyl alcohol and (g - i) butanol Zr(0) (a, d, g), Zr(1) (b, e, h) and Zr(7) (c, f, i).

The heats of CO_2 adsorption (ΔH_{ads}) were below 18 kJ mol^{-1} for all SiO_2 spheres.(Table 2.2 The determination of the heats of adsorption (ΔH_{ads}) for CO_2 from a Langmuir type isotherm did not correlate to the Zr^{4+} content of the sorbents. Structural changes of SiO_2 spheres prepared with different solvents influence the accessibility of Zr^{4+} cations and therefore ΔH_{ads}. Incorporation of Zr^{4+} resulted only in a marginal increase of CO_2 storage capacity for aniline spheres, whereas the uptake increased by 15% for benzyl alcohol spheres when 1 wt.% Zr^{4+} was incorporated and decreased significantly for 7 wt.% Zr^{4+} (Figure 2.5, Table 2.1). The highest CO_2 uptakes were observed for unmodified butanol Zr(0) (25.8 wt.%) and butanol Zr(1) (26.2 wt.%) at 35 °C and a pressure of 40 bar CO_2. Further incorporation of Zr^{4+} also resulted in a decrease of the maximum CO_2 storage capacity. Noteworthy, the uptake capacity for CO_2 still remained at reasonable capacity for

all adsorbents. The CO_2 uptake is linearly correlated to the BET surface area of all SiO_2 spheres independent of the Zr^{4+} content (Figure 2.8 a). Zeolite 13X showed an enhanced uptake due to strong interaction of CO_2 with the Na^+ cations (Figure 2.8 a, Figure 2.8 b), while SBA-15 followed the trend of the SiO_2 spheres. However, the CO_2 uptake capacity did not depend on the pore volume for all samples investigated (Figure 2.2, Figure 2.9).

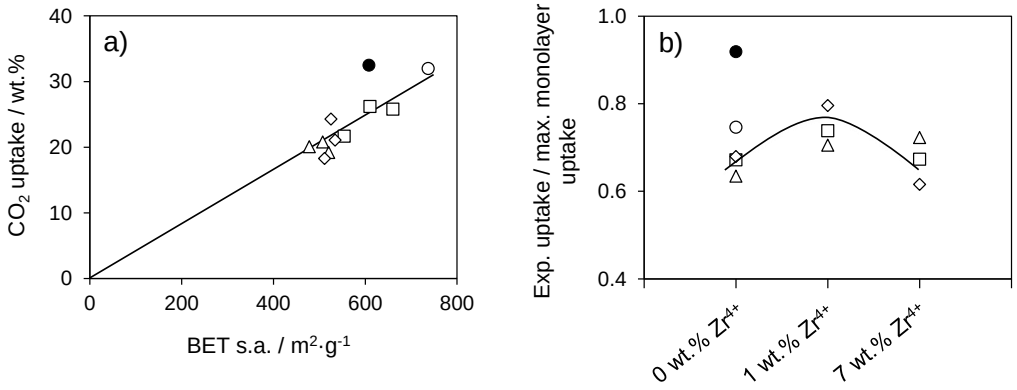

Figure 2.8: (a) Correlation between the CO_2 uptake (35 °C, 40 bar) and BET surface area and (b) influence of Zr^{4+} content on the normalized uptake capacity. SBA-15 (non-filled circle), zeolite 13X (filled circle) and aniline (triangle), benzyl alcohol (diamond) and butanol (square) spheres with varying Zr^{4+} concentrations.

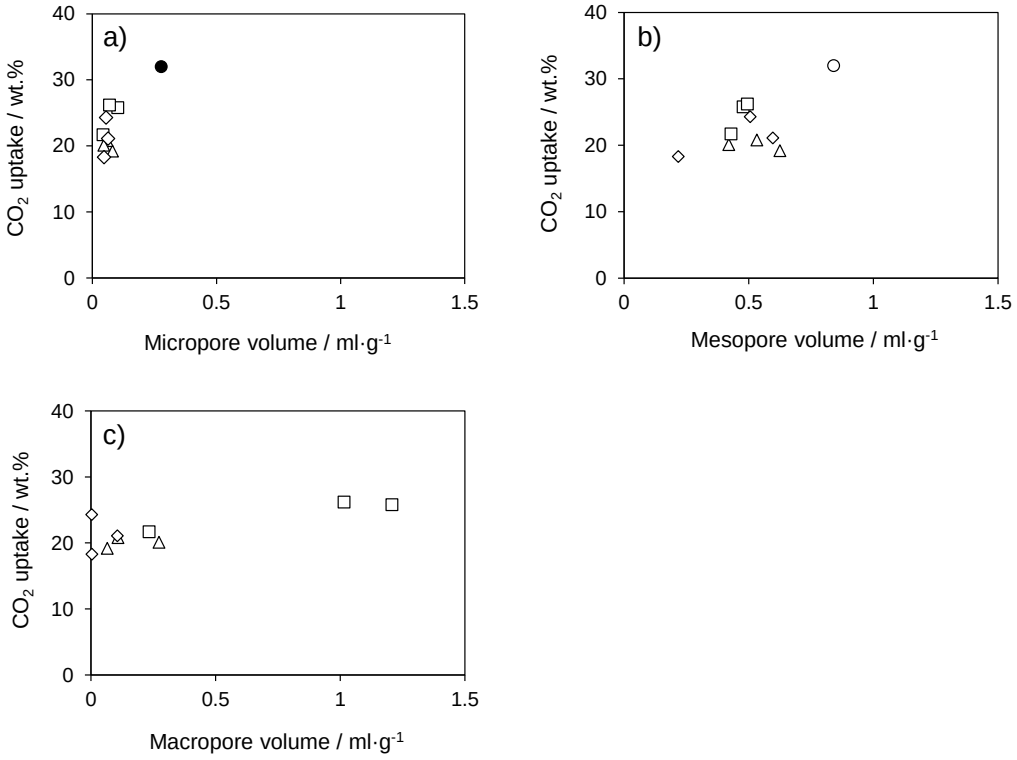

Figure 2.9: Correlation between CO_2 uptake (35 °C, 40 bar) and (a) micropore, (b) mesopore and (c) macropore volume. SBA-15 (non-filled circle), zeolite 13X (filled circle) and aniline (triangle), benzyl alcohol (diamond) and butanol (square) spheres with varying Zr^{4+} contents.

The general increase in adsorption capacity for low Zr^{4+} contents (1 wt.%) resulted in a moderate decrease in the free pore volume and surface area, but enhanced CO_2 physisorption due to the stronger interaction of CO_2 with the oxygen Lewis base sites neighboring Zr^{4+} (Figure 2.3, Figure 2.8 b). With increasing Zr^{4+} concentration, the decrease in the pore volume was more pronounced which led in turn to a decrease of the accessibility of Zr^{4+} sites and to a decrease of CO_2 adsorption capacity (Figure 2.3, Figure 2.8 b).

The differences in the interaction of CO_2 on pure and Zr^{4+} modified SiO_2 spheres with 0 and 7 wt.% Zr^{4+} as revealed by the IR spectra of adsorbed CO_2 are illustrated in Figure 2.10. Please note, that the CO_2 adsorption was performed only at 10 mbar, because at higher pressures sensitivity is lost due to an overlap with gas phase CO_2. The samples have been dried for 1 h at 373 K under vacuum prior to adsorption in order to exclude influences of adsorbed H_2O on the adsorption of CO_2. The difference between the IR spectra of activated aniline, benzyl alcohol and butanol unmodified SiO_2 spheres Zr(0) and SiO_2 in presence of 10 mbar CO_2 showed a band at 1633 cm^{-1} (Figure 2.10), which is assigned to the asymmetric stretching vibration of a bridged bidentate bicarbonate species (Scheme 2.3, III). [74–76]

Scheme 2.3: Simplified illustration of potential carbonate surface species of CO_2 bound on SiO_2 spheres. (I) Monodentate carbonate, (II) bidentate bicarbonate, (III) bridged bidentate bicarbonate. M represents the according metal site.

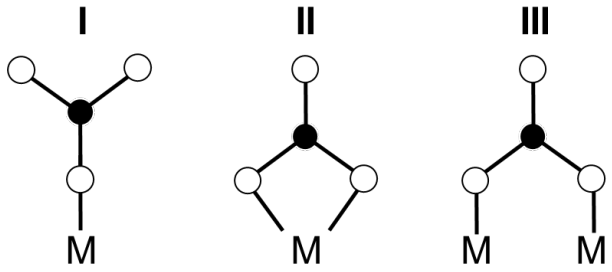

The corresponding symmetric stretching vibration is expected at a 400 cm^{-1} lower frequency and could, therefore, not be recorded due to the strong IR absorption of the SiO_2 matrix in this region. [74,76] Independently of the solvent used, the CO_2 adsorption was more pronounced for Zr^{4+} containing SiO_2 spheres. Incorporation of Zr^{4+} resulted in three additional bands in the range of 1505 - 1380 cm^{-1} that were most pronounced for benzyl alcohol Zr(7) (Figure 2.10) and the bands around 1500 cm^{-1} and 1460 cm^{-1} showed a significant overlap independent of the employed solvents. The band at 1633 cm^{-1} of b-HCO_3^- was strongly overlapped by an intense new peak at 1610 cm^{-1} that was assigned to the asymmetric stretching vibration of bidentate bicarbonates on Zr^{4+} (b-HCO_3^--Zr) (Scheme 2.3, II). [75–77] The symmetric stretching vibration of b-HCO_3^--Zr was observed at 1460 cm^{-1}. [75,76,78] In contrast to SiO_2 spheres without Zr^{4+}, b-HCO_3^- species can additionally be formed on one surface metal atom, resulting in a stronger bound surface species (Scheme 2.3). The bands at 1500 cm^{-1} (asymmetric) and 1380 cm^{-1} (symmetric) are assigned to monodentate carbonate species (m-CO_3^{2-}-Zr) as illustrated in Scheme 2.3 I. [74,76] In summary, only one Zr^{4+} surface site is needed for the adsorption of CO_2, whereas two Si atoms are required for the stabilization of a surface bound bicarbonate species.

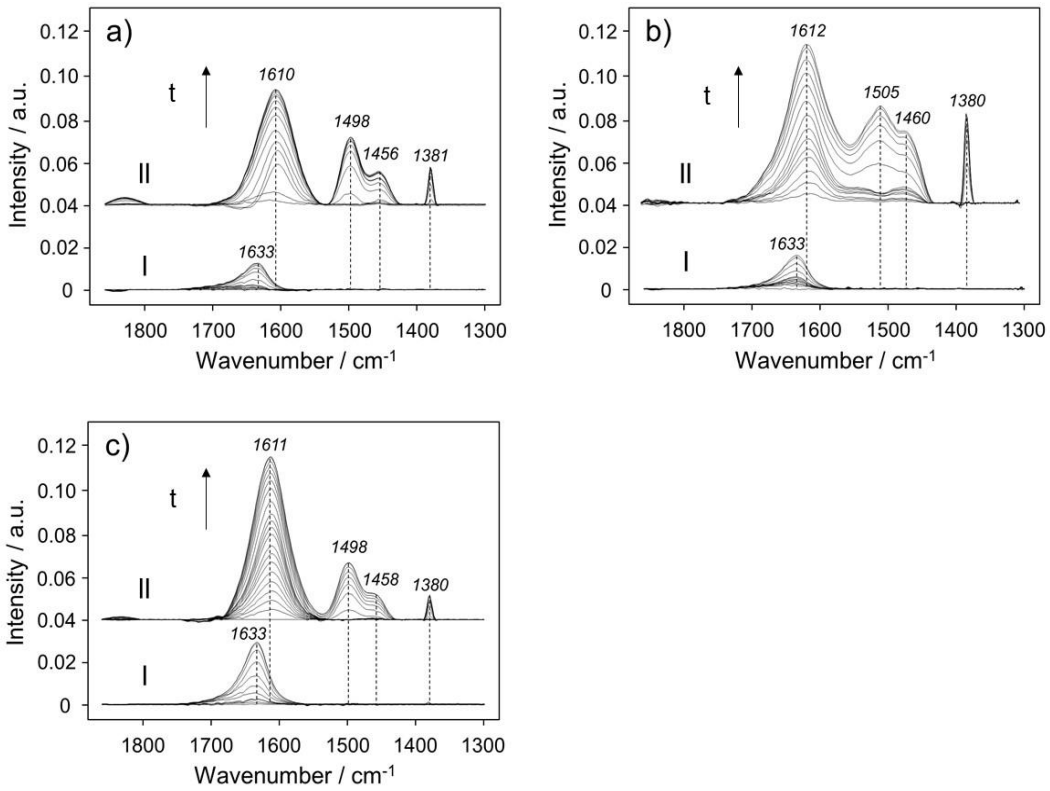

Figure 2.10: IR difference spectra of (a) aniline, (b) benzyl alcohol and (c) butanol Zr(0) (I) and Zr(7) (II) at 10 mbar CO_2 partial pressures. Spectra were taken every 120 s.

2.3.3 Applicability of SiO_2 Spheres for Pressure Swing and Temperature Swing Adsorption

SBA-15 and zeolite 13X were selected as benchmark materials to evaluate the potential of Zr^{4+} containing SiO_2 spheres for CO_2 pre-combustion adsorption processes. The uptake of CO_2 and N_2 over the benchmark materials is compared to the uptake of Zr^{4+} containing SiO_2 spheres in Figure 2.11. CO_2 adsorbed mainly via bidentate bicarbonate species (b-HCO_3^-) inside the pores of mesoporous SBA-15, whereas the microporous zeolite 13X interacts with CO_2 preferably via the oxygen Lewis base sites neighboring Na^+ cations.[79] It should be further noted, that SBA-15 has not only a higher surface area compared to microporous zeolite 13X (737 and 608 $m^2\,g^{-1}$, respectively), but also the total pore volume is roughly 3 times higher (Table 2.4). Both benchmark sorbents have a well-defined pore size distribution (see Appendix Figure A.2).

Table 2.4: BET surface area, pore volume and average pore size of SBA-15 and zeolite 13X. (a) Pore size smaller than 2 nm determined by t-plot method, (b) pore size of 2 to 50 nm determined by BJH method (desorption branch).

	BET surface area / $m^2\,g^{-1}$	Micropore volume[a] / $cm^3\,g^{-1}$	Mesopore volume[b] / $cm^3\,g^{-1}$	Average pore size[b] / nm
SBA-15	737	0	0.840	6.6
Zeolite 13X	608	0.277	0.018	0.78

The shape of the adsorption isotherms of SBA-15 exhibited a strongly preferred adsorption of CO_2 compared to N_2 over the entire pressure range up to 40 bar at 35 °C and 70 °C (Figure 2.11). The slope of CO_2 adsorption isotherms of zeolite 13X was steeper at partial pressures below 10 bar compared to SBA-15 and remained almost constant for higher pressures.

The heats of adsorption, determined from the sorption isotherms, for CO_2 were over three times higher for zeolite 13X (30 $kJ\,mol^{-1}$) than SBA-15 (9 $kJ\,mol^{-1}$). At 35 °C the sorption capacity for CO_2 was almost the same for SBA-15 (32.4 wt.%) and zeolite 13X (32.5 wt.%), whereas at 70 °C the CO_2 uptake of 13X is more than 10 % higher compared to SBA-15 (Table 2.1). Independent of the adsorption temperature, SBA-15 adsorbed less N_2 than zeolite 13X (Figure 2.12 and Table 2.1). The sorption isotherms of SiO_2 spheres indicate a high selectivity for CO_2 over N_2 and had a shape similar to the isotherms of SBA-15 (Figure 2.5, Figure 2.11).

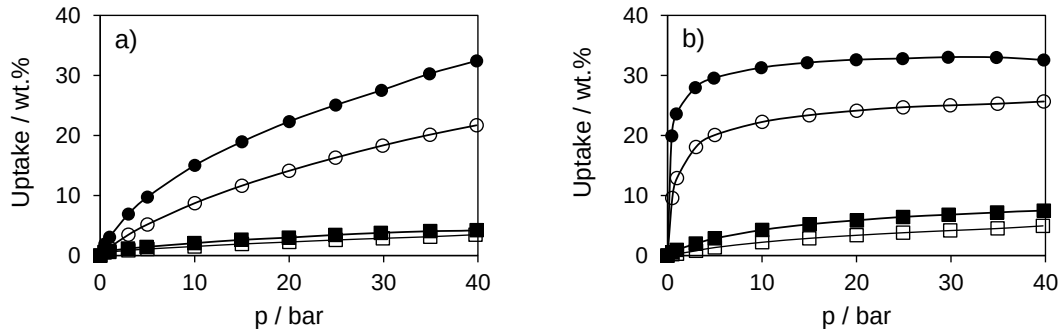

Figure 2.11: CO_2 adsorption (circles) and N_2 adsorption (squares) at 35 °C (filled symbols) and 70 °C (unfilled symbols) of (a) SBA-15 and (b) zeolite 13X.

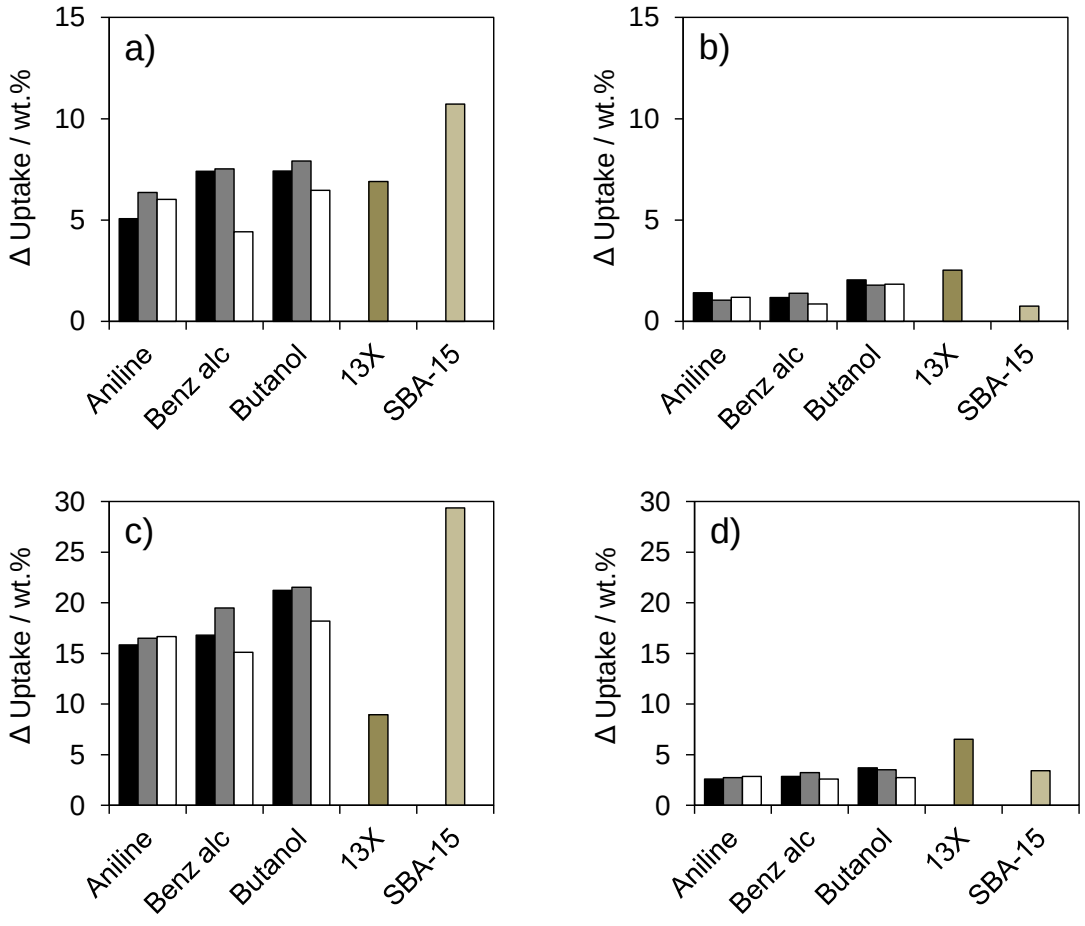

Figure 2.12: Difference in uptake of the sorbent for the desorption step in temperature swing adsorption (35 °C to 70 °C; (a) CO_2, (b) N_2) and pressure swing adsorption (40 - 1 bar; (c) CO_2 ,(d) N_2). Aniline, benzyl alcohol and butanol Zr(0) (black), Zr(1) (grey) and Zr(7) (white).

The performance of all sorbents was evaluated for pressure swing (PSA; 40 to 1 bar at 35 °C) and temperature swing (TSA; 35 °C to 70 °C at 40 bar) adsorption by calculating the difference in uptake from the CO_2 and N_2 sorption isotherms (Figure 2.5, Figure 2.11). As mentioned earlier, it was not possible to determine H_2 adsorption in our set-up up to 40 bar. However, it was possible to determine the adsorption of H_2 on one selected adsorbent (butanol SiO_2 spheres) up to a maximum pressure of 30 bar (Figure 2.13). The adsorption of H_2 was comparably low as the adsorption of N_2 and therefore the quantitative assumption of PSA and TSA operating methods are applicable in pre combustion applications (Figure 2.5, Figure 2.13). Because the heats of adsorption of CO_2 and hence the steepness of the isotherm were so much more pronounced than that of N_2, competitive gas adsorption of CO_2 and N_2/H_2 was not performed.

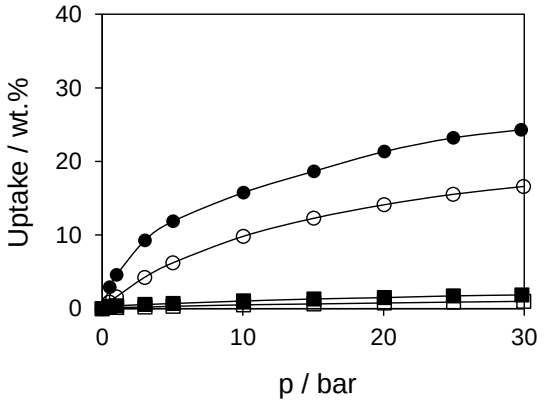

Figure 2.13: CO_2 adsorption (circles) and H_2 adsorption (squares) at 35 °C (filled symbols) and 70 °C (unfilled symbols) of butanol SiO_2 spheres.

The gas composition of a typical pre-combustion process of roughly 40 % CO_2 and 60 % H_2 results in a CO_2 to H_2 ratio of 2/3.[80] SBA-15 exhibits the best adsorption ratio of CO_2 over N_2 with 14.4 (TSA) and 8.6 (PSA). 13X zeolite on the other hand is not applicable under these high pressure separation conditions, because the steep isotherm results in a CO_2 over N_2 ratio of only 2.7 (TSA) and 1.3 (PSA).[81] The maximum CO_2 uptake of SiO_2 spheres increased for 1 wt.% Zr^{4+} and decreased for the materials with higher Zr^{4+} concentrations independently of the solvents used (Figure 2.12). The studied SiO_2 spheres had ratios of the adsorbed concentrations of CO_2 and N_2 of 3.6 (butanol Zr(0) and Zr(1)) to 6.4 (benzyl alcohol Zr(0)) for temperature swing separation and between 5.8 (aniline Zr(7)) and 6.6 (butanol Zr(7)) for pressure swing separation. The separation ratios were significantly higher on all SiO_2 spheres than on zeolite 13X, both in TSA and PSA applications, thus these adsorbents are a promising alternative to SBA-15 in PSA processes. While small concentrations of Zr^{4+} in the SiO_2 spheres appear to be beneficial, it is difficult to derive a generalized influence of the Zr^{4+} content on the separation performance of CO_2 over N_2, because in addition to the chemical modifications also structural changes (varying with

the solvent) were induced upon incorporation of Zr^{4+}.

The long-term stability of the sorbent is a key feature of a cost-effective separation process. Hence, the compressive strength of SiO_2 spheres is compiled for the solvents and Zr^{4+} contents applied (Figure 2.14, Table 2.5).

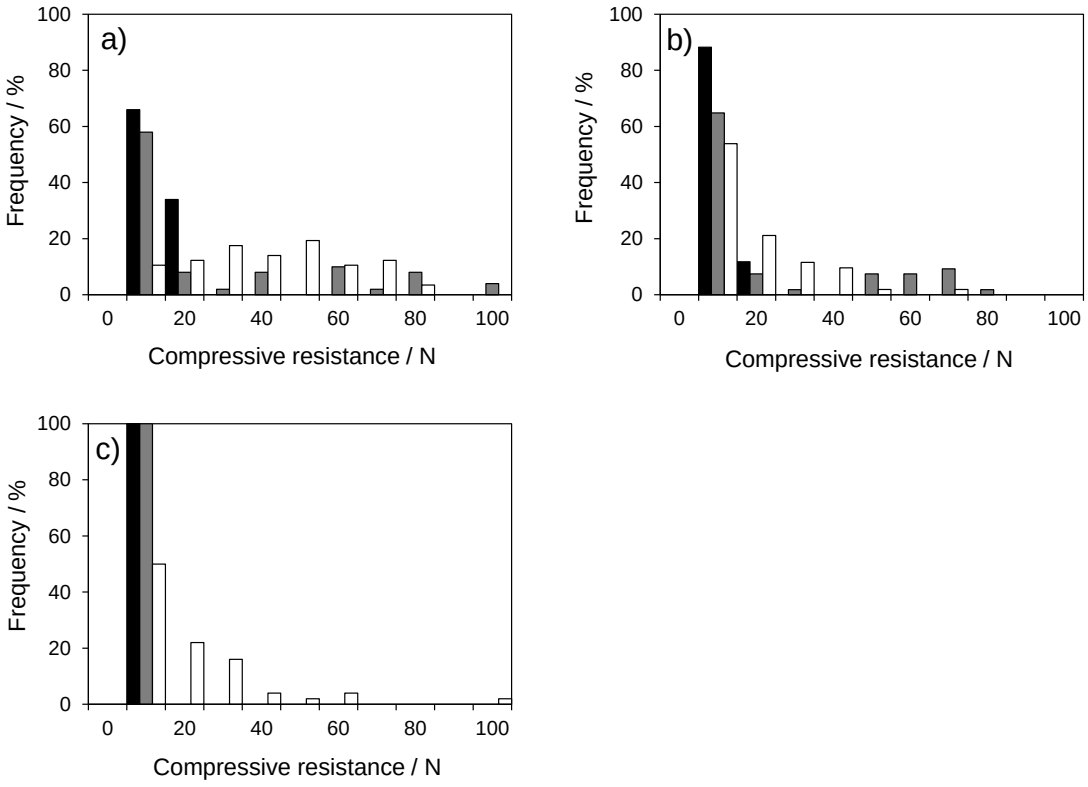

Figure 2.14: Compressive strength of (a) aniline, (b) benzyl alcohol and (c) butanol Zr(0) (black), Zr(1) (grey) and Zr(7) (white).

Additionally, the compressive strength was plotted over the according particle size of 50 SiO_2 spheres for each sorbent (Figure 2.15). The particle size distribution was symmetric for aniline and benzyl alcohol spheres with a maximum around 1.3 mm (Figure 2.15, Table 2.5). Butanol spheres had a less defined particle size distribution, which is attributed to the strong solvent exchange across the micelle interface (Figure 2.15). The average particle size, however, was also approximately 1.3 mm (Table 2.5). The average compressive strength of the SiO_2 spheres increased upon incorporation of Zr^{4+} independent of the used solvents (Table 2.5). Aniline spheres exhibited the highest mechanical stability of all sorbents because of the accelerated condensation induced by the solvent with the highest pKa (Figure 2.14, Table 2.5). The lowest compressive strength was observed for butanol spheres, because both butanol Zr(0) and Zr(1) have a compressive strength lower than 20 N (Figure 2.15). The significant increase in stability of butanol Zr(7) was in accordance with the total loss of the macroporous structure. Overall, the incorporation of Zr^{4+} led to a

larger differences between the compressive strengths. We speculate that the concentration of Zr^{4+} cations is too low to compensate for the lack of long range order, leading to reduced stability of the spheres. Thus, it can be concluded that a defined stability of the SiO_2 spheres is limited by the content of Zr^{4+} that can be incorporated in the SiO_2 framework.

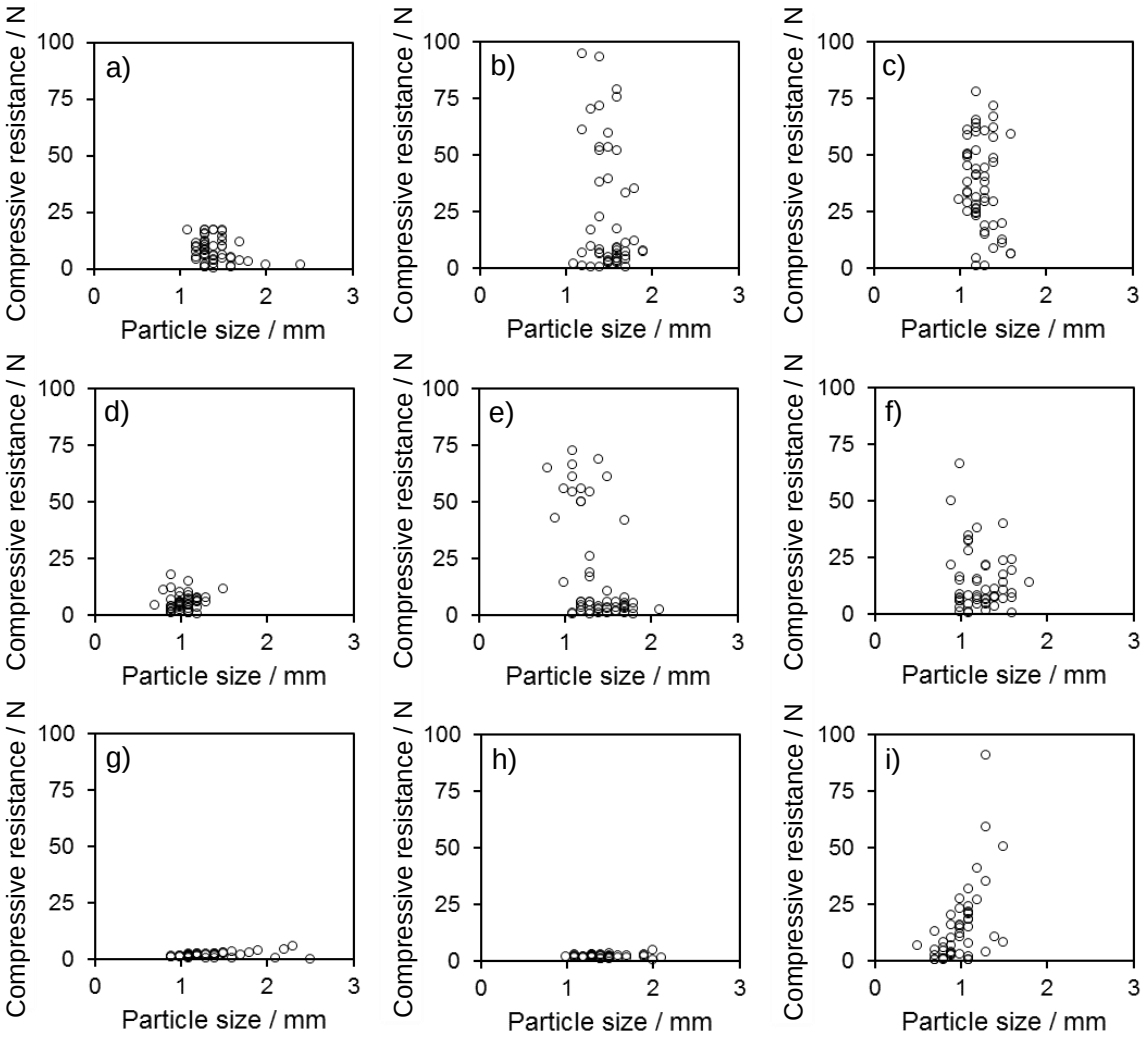

Figure 2.15: Compressive strength over the particle size of (a - c) aniline, (d - f) benzyl alcohol and (g - i) butanol Zr(0) (a, d, g), Zr(1) (b, e, h) and Zr(7) (c, f, i).

Table 2.5: Compressive strength and average diameter of SiO_2 spheres.

	Average compressive strength / N	Average spherical diameter / mm
Aniline Zr(0)	8.1	1.4
Aniline Zr(1)	23.5	1.5
Aniline Zr(7)	36.7	1.3
Benzyl alcohol Zr(0)	5.4	1.1
Benzyl alcohol Zr(1)	18.5	1.4
Benzyl alcohol Zr(7)	14.2	1.3
Butanol Zr(0)	1.8	1.3
Butanol Zr(1)	1.9	1.4
Butanol Zr(7)	14.8	1.0

2.4 Conclusion

Hierarchically structured spherical sorbent for the separation of CO_2 and N_2 for pre-combustion applications have been explored. The significant influence of the solvents on the morphology of the SiO_2 spheres did not only correspond to the solvents basicity, but also on the solubility in H_2O, which both strongly influenced the interactions via the borders of the micelles resulting in the formation of a macroporous structure. The use of aniline and benzyl alcohol as a solvent for the synthesis resulted in micro- and mesopores in the spherical sorbents, whereas butanol led to an additional and well-defined macroporous structure. SiO_2 spheres prepared with butanol combined a macropore volume of $1.2\,mL\,g^{-1}$ with micropore and mesopore volumes of $0.1\,mL\,g^{-1}$ and $0.4\,mL\,g^{-1}$, respectively. Zr^{4+} was successfully incorporated in the framework structure of the SiO_2 spheres. The presence of Zr^{4+} enhanced the CO_2 interaction, but the uptake capacity was limited because a lower micro- and mesopore volume reduced the sorption capacity. The accelerated hydrolysis caused by the Zr alkoxides resulted in a less ordered and more branched structure of the framework. Even as the pore volumes decreased with higher concentrations of Zr^{4+} cations, the still relatively large pore volumes make the spheres a highly interesting alternative to zeolite 13X and SBA-15 in pressure swing and temperature swing pre-combustion processes. The stability of the sorbents increases for higher Zr^{4+} contents improving the long-term stability of the SiO_2 spheres.

2.5 Experimental Section

2.5.1 Sorbent Preparation and Synthesis

SiO_2 spheres were synthesized according to Scholz et al. in a base catalyzed condensation reaction.[62–64] Phenyltrimethoxysilane (PTMS, purity $\geq$ 97 %), N [3 (trimethoxysilyl)propyl]ethylendiamine (AAMS, purity $\geq$ 97 %), zirconium(IV) t butoxide (80 wt.% in 1-butanol), aniline (purity $\geq$ 99.5 %), benzyl alcohol (purity $\geq$ 99 %) and 2-butanol (anhydrous, purity $\geq$ 99.5 %) were purchased from Sigma Aldrich. Tetraethylorthosilicate (TEOS) and the copolymer Pluronic RPE 1740 were provided by WACKER and BASF, respectively. All chemicals were used without any further purification. Deionized water was the reaction medium in the reactor column.

The surfactant containing precursor solution was prepared by mixing 6.50 g of the surfactant Pluronic RPE 1740 and 7.11 g of the solvent (aniline, benzyl alcohol or 2 butanol). 0, 5 and 25 wt.% of zirconium(IV) t butoxide based on the amount of TEOS were added to the structure directing precursor solution. The addition of zirconium(IV) t-butoxide reduced the amount of solvent accordingly. The Si precursor rich solution contained 7.20 g TEOS, 4.01 g AAMS and 5.18 g of PTMS. Both solutions were stirred separately for 15 min. Prior to injection, the two solutions were merged and mixed for additional 10 min. The pH of the final precursor emulsion was measured with a Mettler Toledo Seven CompactTM pH/ion meter S220 with a LoT 403-M8-S7/120 electrode.

The mixed precursor solution was injected directly into the injection flow on top of the reactor column (Figure 2.16). The temperature of the reactor column was constant at 65 °C. The precursor solution was injected with a syringe pump at a flow rate of 15 mL h^{-1}. The main flow in the column was 7 L h^{-1} and the injection flow was 2 L h^{-1}. Both flows have to be adjusted to the density of the Si^{4+} precursor solution in order to assure the sinking of the spheres to the bottom of the reactor. The length of the reactor column is 4m. The spheres were directly formed by micelle formation and base catalyzed condensation. The particle size of the SiO_2 spheres was perfectly spherical and mainly influenced by the injection rate of the mixed precursor solution and the bypass stream in the reactor column. After removing the SiO_2 spheres at the bottom of the column, they were washed three times with copious amount of deionized water. The SiO_2 spheres were aged in deionized water overnight under ambient conditions in order to assure full condensation of the spheres. Afterward, the SiO_2 spheres were washed with 3×30 mL of water and 3×30 mL of ethanol, then dried overnight. All adsorbents in this work were calcined in synthetic air (100 mL min^{-1}) at 600 °C for 3 h with a heating rate of 1 °C min^{-1} to ensure the removal of all remaining surfactants.

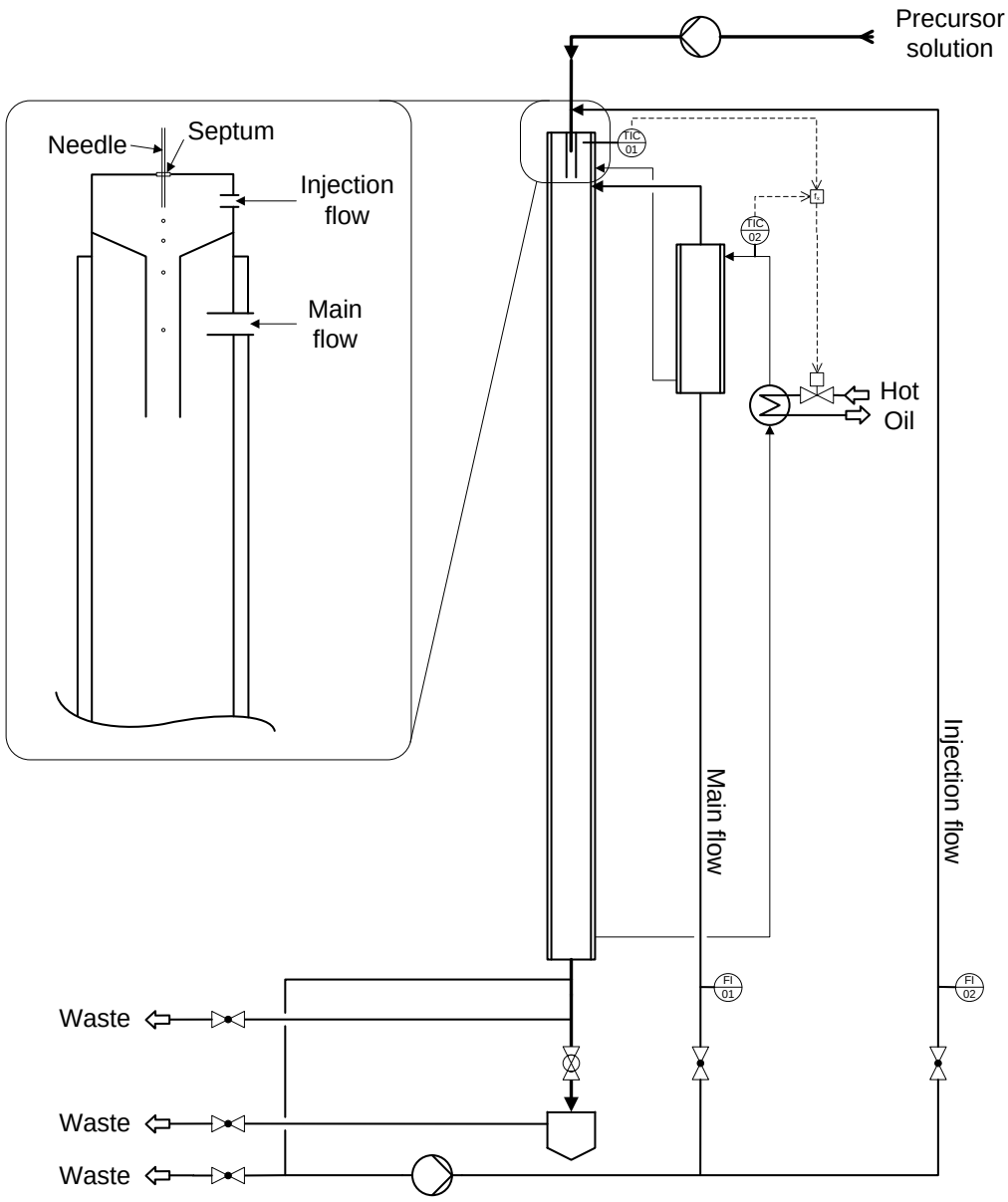

Figure 2.16: Flow sheet of the reactor column for synthesis of millimeter-scaled SiO_2 spheres.

SBA-15 was synthesized according to literature.[55,82] 6 g of hydrochloric acid (Sigma Aldrich, 37 wt.%) was added to 188.5 g of DI water and 10.25 g of poly(ethylene glycol)-block-poly(propylene glycol)-block-poly(ethylene glycol) (P123, BASF, M_w of 5750 Da) under rigid stirring. The solution was stirred for one day at 35 °C until a homogenous phase was obtained. After 2 h tetraethylorthosilicate (TEOS, Sigma Aldrich, purity $\geq$ 99 %) was added to the solution and the mixture was stirred at 35 °C for additional 24 h. The polymerized solution was aged in autoclaves at 80 °C for 24 h. The solution was filtered with deionized water three times and the precipitate was dried at 60 °C for 5 h prior to calcination in synthetic air (8 h at 600 °C, heating rate: 2.5 °C min^{-1}, total flow rate: 100 mL min^{-1}).

2.5.2 Sorbent Characterization

The C, H and N contents of SiO_2 spheres were determined by combustion analysis. The Zr^{4+} content of the sorbents was determined with inductively coupled plasma optical emission spectrometry (ICP OES). The C, H and N content of SiO_2 spheres were determined with a EURO EA elemental analyzer. 1 - 2 mg of each sample was weighed in a tin beaker. The samples were burned at 1000 °C in a He stream. After the reduction of NOx compounds, the gas stream was separated with a GC column. The products (CO_2, NO_2, H_2O) were analyzed with a thermal conductivity detector (TCD). Zr Elemental Analysis: 50 mg of each sample was digested in a solution of 2 mL deionized water, 2 mL HF and 0.5 mL of H_2SO_4. Sc_2O_3 was added as an internal standard. The acid digestion was conducted in a pressure resistant vessel at 85 °C until a clear solution was obtained. The Zr content was determined with inductively coupled plasma optical emission spectrometry (ICP OES). A $ZrClO_2$/HCl solution was used as an internal standard.

SEM images were recorded with a Jeol JSM 7500F microscope. Images were taken with a resolution from 1 μm to 100 μm with a lower electron image (LEI) and a yttrium aluminum garnet (YAG) detector. Sputter coating was not performed on all samples.

A Philips X'pert diffractometer equipped with an X'celerator module, using Cu Kα radiation, was used to measure powder X-ray diffraction (XRD) patterns. Diffractograms were obtained from $2\Theta = 5°$ to 40° with a step size of 0.033°.

The surface area, micro- and mesopore volume, as well as the according pore size distribution were determined by nitrogen physisorption at −196 °C using a QUADRASORB SI automated surface area and pore size analyzer. Prior to analysis, samples were evacuated at 200 °C for 3 h using a Quantachrome FloVac degasser. Surface area was determined using the Brunauer-Emmett-Teller (BET) method.[83] Pore volumes were divided into micropores (pore size < 2 nm) and mesopores (pore size: 2 - 50 nm). The micropore volume was determined via t plot method and micropore size distribution by the Dubinin-Astakhov (DA) model.[84] The mesopore volume and pore size distribution were determined using the Barrett-Joyner-Halenda (BJH) model on the desorption branch of the isotherm.[85] The meso- and macropore size distribution (0.0036 - 300 μm) of SiO_2 spheres sorbents were determined using a QUANTACHROME PoreMaster mercury intrusion porosimeter with a low-pressure and high-pressure station.

The compressive strength of SiO_2 spheres was measured on a Zwicki Z0.5 with a 20 N and 500 N pressure cell. The measurement was performed for 50 SiO_2 spheres of each sorbent. Prior to the measurement, the particle size of each SiO_2 spheres was determined.

2.5.3 High Pressure Thermogravimetric Analysis

N_2 and CO_2 isotherms were obtained at 35 °C and 70 °C in a range of 0.5 - 40 bar using a Rubotherm magnetic suspension balance (Figure 2.17). Approximately 100 mg (± 0.1 mg) of the sorbent was placed in a steel crucible and dried at 100 °C for 8 h under vacuum prior to adsorption. In order to correct for the buoyancy of the sample in N_2 and CO_2 at different temperatures and pressures, blank adsorption isotherms of non-adsorbing glass spheres (particle size 425 - 600 μm) were determined and subtracted from the isotherms.

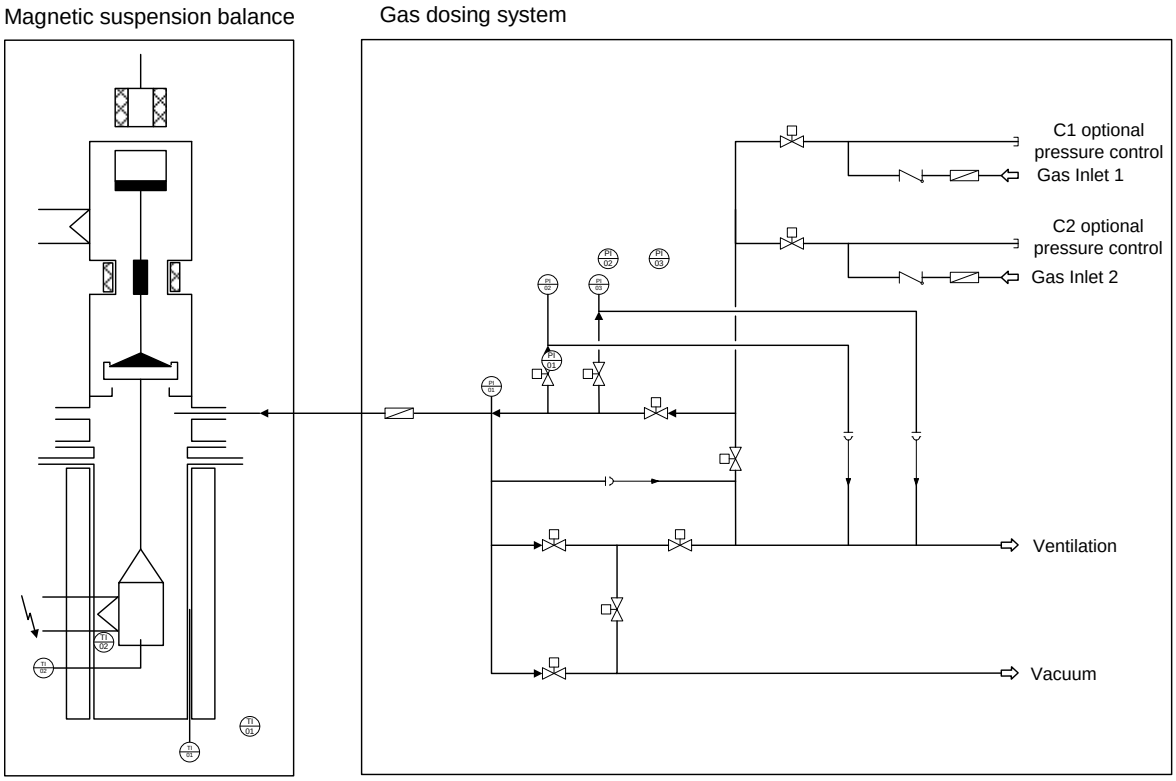

Figure 2.17: Flow sheet of the high-pressure magnetic suspension balance (Rubotherm).

Thermodynamic parameters of the adsorption were determined via the Langmuir adsorption model Equation 2.7:

$$\frac{\Theta}{\Theta_{max}} = \frac{K \cdot p}{1 + K \cdot p} \tag{2.7}$$

Origin was used to fit the coverage in equilibrium and the equilibrium constant K. After determination of the values of K for two different temperatures the Gibb's free enthalpy

was calculated with Equation 2.8 and 2.9.

$$\ln K(T_1) = -\frac{\Delta G_{ads}(T_1)}{R} \cdot \frac{1}{T_1} \quad \Rightarrow \quad \Delta G_{ads}(T_1) = -\ln K(T_1) \cdot T_1 \cdot R \tag{2.8}$$

$$\ln K(T_2) = -\frac{\Delta G_{ads}(T_2)}{R} \cdot \frac{1}{T_2} \quad \Rightarrow \quad \Delta G_{ads}(T_2) = -\ln K(T_2) \cdot T_2 \cdot R \tag{2.9}$$

The thermodynamic parameter ΔS_{ads} (postulating that ΔH_{ads} and ΔS_{ads} are temperature independent) were calculated with Equation 2.10 and 2.11:

$$\Delta G_{ads}(T) = \Delta H_{ads} - T\Delta S_{ads} \quad \Rightarrow \quad \Delta S_{ads} = \frac{\Delta G_{ads}(T_2) - \Delta G_{ads}(T_1)}{T_2 - T_1} \tag{2.10}$$

$$\Delta H_{ads} = \Delta G_{ads}(T) + T\Delta S_{ads} \tag{2.11}$$

2.5.4 Infrared Spectroscopy

IR spectra of SiO_2 spheres were measured on a Bruker VERTEX 70 spectrometer with a mercury cadmium telluride (MCT) detector. A self-supporting wafer (ca. 10 mg cm^{-2}) was placed in a vacuum IR cell with CaF_2 windows. Prior to measurements, the wafer was activated at 100 °C for 1 h under vacuum (p = 10^{-6} mbar). CO_2 was adsorbed on the sample at a partial pressure of 10 mbar and 40 °C. Spectra were taken every 120 sec. The IR spectra were obtained by collecting 128 scans with a resolution of 4 cm^{-1}, baseline corrected and normalized to the intensity of Si-O overtone resonances in the range of 2095 - 1755 cm^{-1}.

2.6 Associated Content

Additional Information

N_2 physisorption isotherms of the sorbents are listed in the Appendix A.1.

Peer-Reviewed Publication

This chapter is based on the following article: Maximilian W. Hahn, Matthias Steib, Andreas Jentys and Johannes Lercher, Tailoring Hierarchically Structured SiO_2 Spheres for High Pressure CO_2 Adsorption, *J. Mater. Chem. A.*, **2014**, Vol.2, 13624-13634.

Clearance by the Publisher

The Royal Society of Chemistry gave approval to non-commercially reproduce the accepted article (Green Open Access) both in print and online.

Notes and Author Contributions

The outstanding performance of Matthias Steib during his Master's thesis was acknowledged with Co-Authorship of the article as appeared in J. Mater. Chem. A..

Oral Presentations

M.W. Hahn, M. Steib , A. Berger, A. Jentys, J.A. Lercher, One-step synthesized hierarchically structured SiO_2 spheres for pre-combustion applications, presented at the 6^{th} *FEZA conference* **9/2014**. Leipzig, Germany.

M.W. Hahn, A. Jentys, J.A. Lercher, Novel solid sorbents for post- and pre-combustion applications, presented at the *BMBF iC*^{4} *Konsortium* **10/2013**. Munich, Germany.

Poster Presentations

M.W. Hahn, E. Ball, M. Steib, A. Jentys, J.A. Lercher, One-step synthesized mesoscale organized silica spheres for CO_2 adsorption, presented at the *COPS-X* **5/2014**. Granada, Spain.

3 The Role of Amine Functionality to the CO_2 Capture Mechanism on Silanol Surfaces

3.1 Abstract

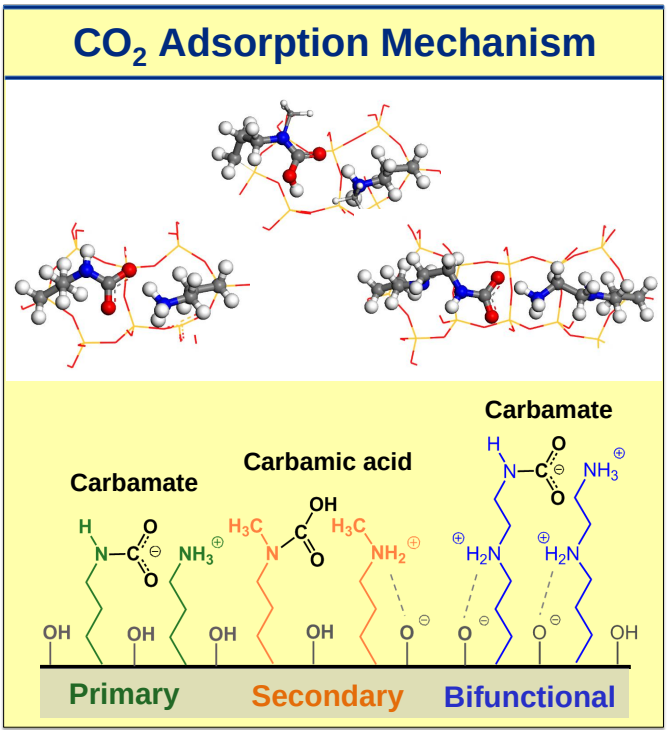

The adsorption of CO_2 was investigated on millimeter scale SiO_2 spheres that possess primary, secondary and bifunctional aminosilanes immobilized on the silanol surface.[1] Mechanistic insight in the interactions of CO_2 and amine groups was gained by monitoring the adsorption of CO_2 via IR spectroscopy and thermo gravimetry as well as quantum mechanical modeling.[2] Primary amines bonded CO_2 through the formation of carbamates, whereas carbamic acid was formed when CO_2 interacted with secondary amines. The adsorption of CO_2 is dependent on the functionality of the amine group, the spacing between the aminosilanes as well as access to stabilizing surface Si-OH groups. The intermolecular protonation of a second amine group is crucial for the stabilization of carbamates and thus two primary amine groups are required to capture one CO_2 molecule. The energetically favored protonation of secondary amine groups by surface silanol groups facilitates the formation of carbamic acid preventing their conversion to carbamates. Thus, stabilization of carbamic acid on silanol surfaces also requires two amine groups resulting in essentially the same amine efficiency for primary and secondary amine groups. However, limited accessibility to surface Si-OH groups at high amine loadings hinders the stabilization of carbamates

[1] This chapter is based on the article of the same title as submitted to the Journal of American Chemical Society. Copyright 2015 American Chemical Society.

[2] All results on quantum mechanical modeling were provided by Jelena Jelic and Karsten Reuter.

on primary amines leading to significantly higher uptake capacities for secondary amines. The adsorption inactive secondary amine group in bifunctional aminosilanes constrains intramolecular adsorption and lowers the maximum achievable amine efficiency down to 25 %.

3.2 Introduction

The most common way to obtain amine functionalized solid sorbents is the impregnation of highly-ordered porous supports with low molecular amines or amino polymers. [86–88] Although simple in preparation, the weakly adsorbed amines can easily degrade and desorb at higher temperatures. [89–91] CO_2 adsorption on solid amine-functionalized sorbents (prim. and sec.) follows predominantly the carbamate mechanism ($[RCH_3NH_3^+][RCH_3NHCOO^-]$) and does not proceed via formation of bicarbonates ($[RCH_3NH_3^+][HCO_3^-]$) as observed in aqueous solutions. [44] Bicarbonates are the only stable adsorption species for tertiary amines due to the absence of inter-amine protonation and thus always requires the presence of H_2O. [44] In the carbamate mechanism two amine groups are required to capture one CO_2 molecule. Thus, the maximum amine efficiency, defined as captured CO_2 molecules per amine group, is limited to 50 %. Higher amine efficiencies were reported in dimethyl sulfoxide (DMSO), polyethylenglycol (PEG) and ionic liquids by a change in the adsorption mechanism to formation of carbamic acid ($RCH_3NHCOOH$). [92–97]

The direct condensation of aminosilanes with surface OH groups, so called grafting, leads to immobilized aminosilanes on the surface and in the pores of the sorbent. [44,98–100] Brunelli et al. reported that the most dominant mechanism for the CO_2 adsorption of grafted primary and secondary amines was the cooperative amine-amine adsorption (intramolecular carbamate mechanism). [38] However, the stabilization of the carbamate by a surface Si-OH group also had a non-negligible influence on the amount of adsorbed CO_2 for linker lengths above two C atoms that allow for a sufficient flexibility of the hydrocarbon chain of the amine for an enhanced support interaction. [38]

In this chapter we investigate the influence of the amine functionality and concentration of in-situ immobilized primary (APTMS(1)) and secondary amines (MAPS(2)) with a C3 linker length (Scheme 3.1) on the water free CO_2 adsorption on silanol surfaces. Tertiary amines were not included in this study due to the necessity of the presence of H_2O to bind CO_2. [44] The amine functionalized, millimeter-scale spherical adsorbents were synthesized in an economical one-step procedure via a non-toxic green process. The intramolecular stabilization of a CO_2 molecule was studied by employing a bifunctional amine (AAMS(1,2), Scheme 3.1) in the synthesis. The interaction of amine groups with surface silanol groups during CO_2 adsorption at low amine contents is equally investigated as is the stabilization between two neighboring amines (intermolecular stabilization) at higher amine concentrations. The adsorption capacities of SiO_2 spheres were determined gravimetrically, and in-situ infrared spectroscopy and computational quantum mechanical modeling were combined to investigate the sorption mechanism of CO_2 on amines.

Scheme 3.1: Aminosilanes employed in synthesis.

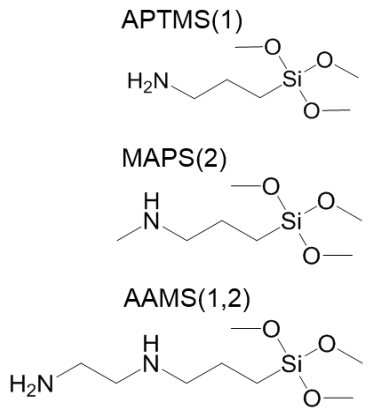

3.3 Results and Discussion

3.3.1 Structural Properties of SiO_2 Spheres and the Influence of Remaining Surfactants

The surface properties of SiO_2 spheres strongly depend on the removal of the surfactants and the according method chosen for the latter. Moreover, the functionality and the concentration of amines, employed in the synthesis, influence the morphology of the sorbents through base catalyzed condensation of TEOS.[101] No defined crystalline structure could be observed by XRD for all SiO_2 spheres and therefore, a well-defined long range order was excluded (Figure 3.1).

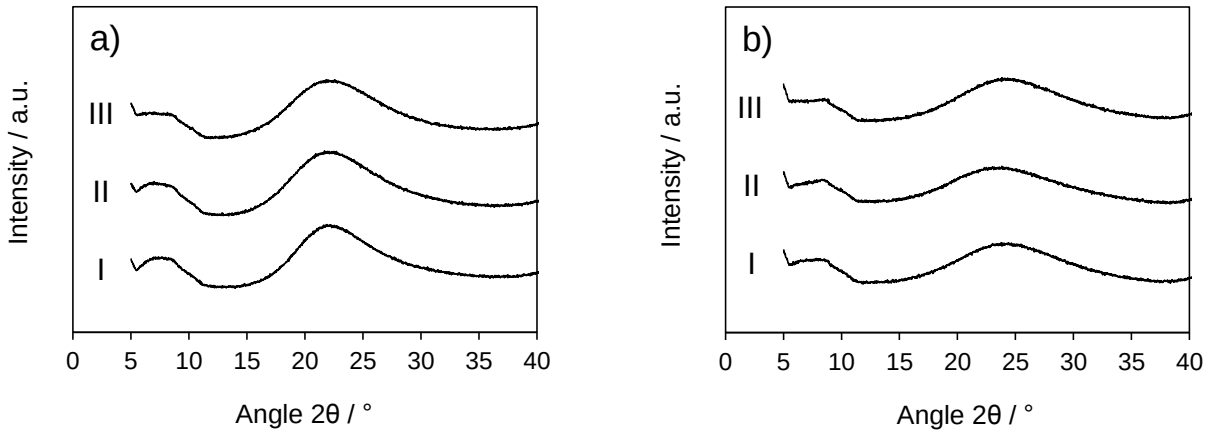

Figure 3.1: XRD of (I) APTMS(1), (II) MAPS(2) and (III) AAMS(1,2) (Table 3.1). Intensity in arbitrary units.

The degree of residual surfactants in the adsorbents after Soxhlet extraction was below 1 mol % based on the content of aminosilanes for APTMS(1), MAPS(2) and AAMS(1,2). The amine concentration of the SiO_2 spheres was in the range of 3.3 - 3.6 mmol g^{-1}. The pore volume was most pronounced for APTMS(1) and AAMS(1,2) that also exhibited the highest surface areas with 82 and 92 $m^2\,g^{-1}$, respectively (Table 3.1).

Table 3.1: Amine concentration, BET surface area and pore volume determined by N_2 physisorption of SiO_2 spheres. Mesopore volume determined by BJH method (desorption branch).

	Amine concentration / mmol g^{-1}	BET surface area / $m^2\,g^{-1}$	Mesopore volume / $cm^3\,g^{-1}$
APTMS(1)	3.31	82	0.27
MAPS(2)	3.30	40	0.13
APTMS(1,2)	3.29	92	0.41

The N_2 physisorption isotherms of mesoporous soxhleted SiO_2 spheres as well as the pore size distribution are displayed in Figure 3.2. The sorbents revealed a hierarchical distribution of the pores independent of the aminosilane employed in the synthesis (Figure 3.2). The hierarchical structure of the sorbents has been confirmed in our former studies by scanning electron microscopy (SEM).[62,64,101] The pore size distribution was well defined for APTMS(1) and AAMS(1,2) with average pore sizes at around 15 and 30 nm, respectively. In contrast, a significantly broader distribution was observed for MAPS(2) (Figure 3.2).

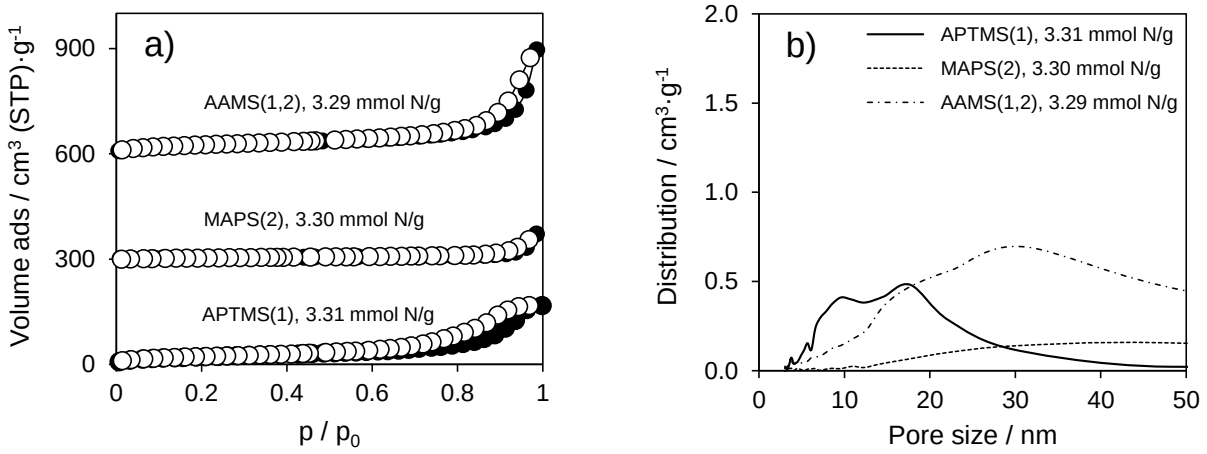

Figure 3.2: (A) Isotherms, adsorption (filled symbols) and desorption (unfilled symbols), and (B) pore size distribution (BJH method, desorption branch) of APTMS(1), MAPS(2) and AAMS(1,2) (Table 3.1) determined via N_2 physisorption.

The pK_a values, representing the Brønsted basicity, of primary and secondary amines are both between 10 and 11.[69] Nevertheless, secondary amines reveal a higher Lewis basicity because of an enhanced electron density, induced by the additional alkyl group neighboring the N atom.[102] Therefore, the base catalyzed condensation of TEOS was more rapid when secondary aminosilanes were employed in the synthesis due to their higher nucleophilicity.[70,103] Thus, the enhanced condensation rate of TEOS with MAPS(2) leads to cross-linking and a less-ordered SiO_2 framework. In agreement with the latter, the most ordered structure of all sorbents was achieved by the primary aminosilane, being the weakest Lewis base (Figure 3.2). Further, the high mesopore volume of soxhleted SiO_2 spheres synthesized with AAMS(1,2) is attributed to the enhanced length of the aminosilane, directing the structural alignment of the condensed TEOS molecules (Figure 3.2).

In summary, the structural properties of SiO_2 spheres were least evolved when synthesized with the strong secondary Lewis base MAPS(2) compared to APTMS(1) and AAMS(1,2).

3.3.2 Impact of the Amine Functionality on the CO_2 Capture Mechanism of Amines on Silanol Surfaces

The water-free adsorption mechanism of CO_2 on primary, secondary and bifunctional amines (Scheme 3.1) immobilized on silanol surfaces was experimentally investigated by infrared (IR) spectroscopy at medium amine concentrations ($3.30 \pm 0.01\,\mathrm{mmol\,g^{-1}}$) that allow intramolecular interaction between vicinal amine groups and sufficient access to surface Si-OH groups (Figure 3.3). For further notation, the sorbents are assigned according to the aminosilanes employed, followed by the functionality in brackets: APTMS(1), MAPS(2), AAMS(1,2). The relevant IR adsorption bands in the range of 1750 - 1300 $\mathrm{cm^{-1}}$ are listed in Table 3.2. Prior to adsorption of CO_2, partial protonation of the amine groups by surface silanol groups (Si−OH) already proceeds even under H_2O free conditions, as can best be illustrated by the observation of the band at 1660 - 1630 $\mathrm{cm^{-1}}$ characteristic for the asymmetric NH_3^+/NH_2^+ deformation (Figure 3.3, Table 3.2) The linker length of 3 C atoms was found to be sufficient for the amine groups to interact with Si-OH groups independent of the type of aminosilane. [38]

Table 3.2: Overview of relevant IR bands for the adsorption of CO_2 on amine functionalized SiO_2 supports in the range of 1750 - 1300 $\mathrm{cm^{-1}}$.

Wavenumber / $\mathrm{cm^{-1}}$	Assignment	References
1720 - 1670	CO stretching vibration (carbamic acid)	[104–108]
1660 - 1620	Asymmetric NH_3^+/NH_2^+ deformation	[109–111]
1565 - 1550	Asymmetric COO^- stretching vibration	[33,98,104,112]
1490 - 1480	Symmetric NH_3^+/NH_2^+ deformation	[110–112]
1430 - 1400	Symmetric COO^- stretching vibration	[110–112]
1380	OH deformation (carbamic acid)	[107,108]
1330 - 1300	NCOO skeletal vibration	[33,98,106]

The arrangement of the aminosilanes on the silanol surface obtained by density-functional theory (DFT) calculations is illustrated in Figure 3.4. A detailed description of the quantum mechanical modeling is presented in the experimental section. Please note that the adsorption of CO_2 proceeds in a water free environment, but the drying condition of the adsorbents is limited by the degradation of the aminosilanes. Thus, deprotonated Si-OH groups were stabilized by hydrated vicinal silanol groups that allow hydrogen bridging interactions (see Appendix Figure A.4 for IR spectra) A minimum of two vicinal amine groups is required to stabilize the protonation of one amine group by surface Si-OH groups via intermolecular hydrogen interaction (exemplarily illustrated for MAPS(2) in Figure 3.4).

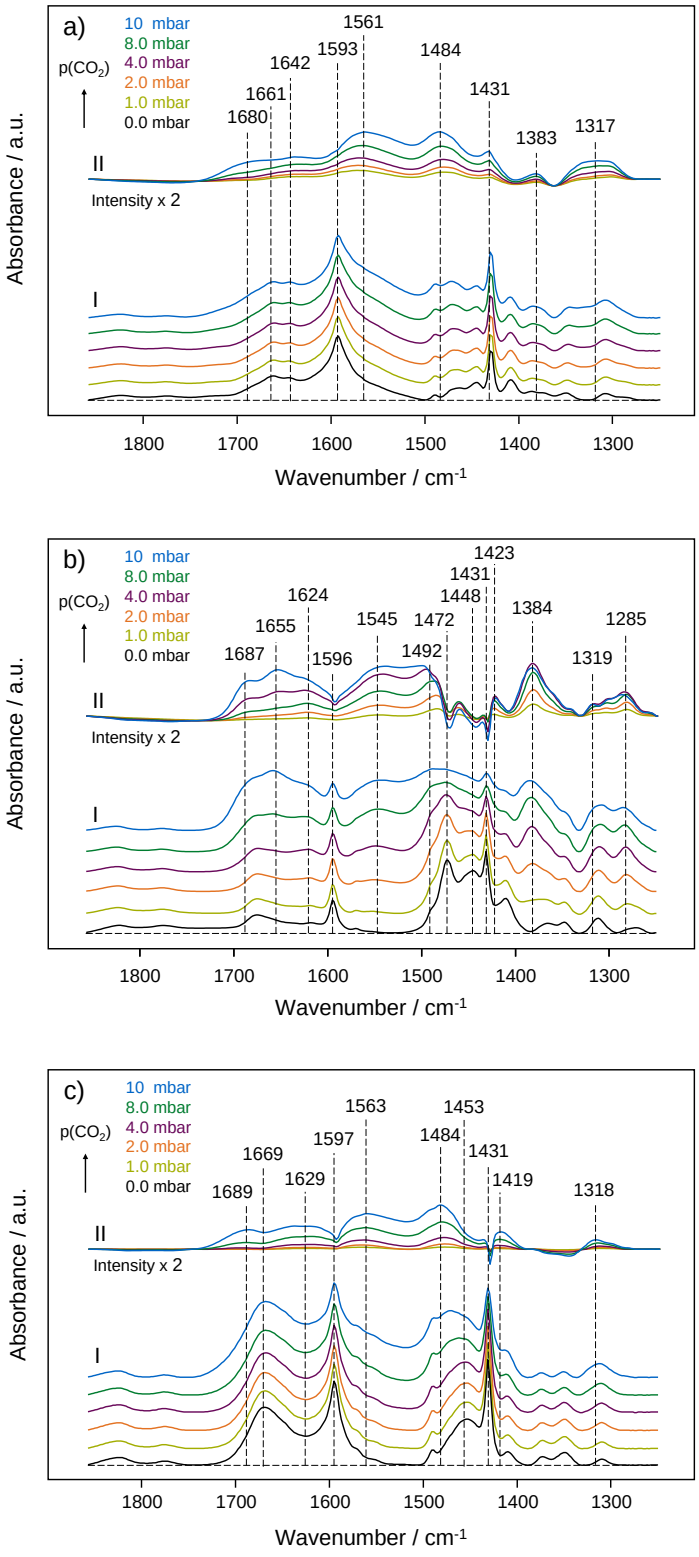

Figure 3.3: (I) Absolute and (II) difference IR spectra of (a) APTMS(1) (3.31 mmol g^{-1}), (b) MAPS(2) (3.30 mmol g^{-1}) and (c) AAMS(1,2) (3.29 mmol g^{-1}) at CO_2 partial pressures up to 10 mbar. Spectrum range from 1850 - 1250 cm^{-1}. Absorbance in absorption units.

It should be noted that the protonated amine and deprotonated surface silanol group do not undergo a complete charge separation under water free conditions and the amine species remain in close proximity to the surface (Figure 3.4b).

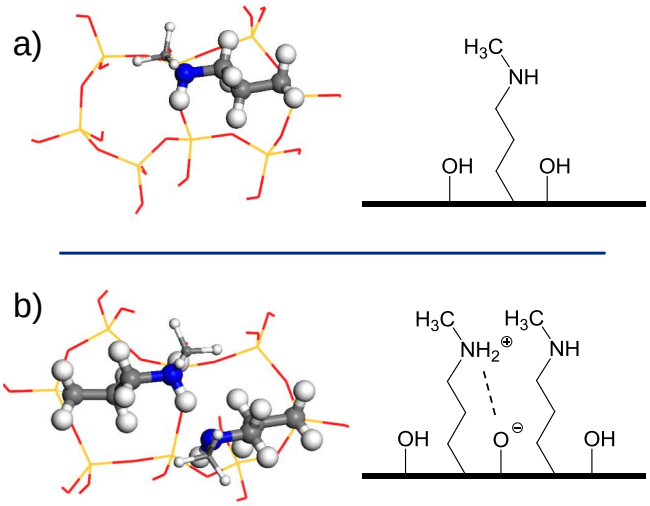

Figure 3.4: Influence of intermolecular amine interaction and protonation by surface silanol groups exemplarily for secondary aminosilanes. (a) Single site and (b) vicinal amine interaction of MAPS(2). Molecular structure is displayed in topview.

The proton affinity (determined by DFT) was 30 and 43 kJ mol^{-1} higher for secondary amines in MAPS(2) and AAMS(1,2) than for APTMS(1), in agreement with gas basicities reported for primary and secondary amines (Table 3.3). [113]

Table 3.3: Proton affinity (kJ mol^{-1}) of APTMS(1), MAPS(2) and AAMS(1,2). Determined by computational quantum mechanical modeling.

APTMS(1)	MAPS(2)	AAMS(1,2)	
		Primary	Secondary
-916	-946	-917	-959

Thus, protonation was most pronounced for the secondary amine group in AAMS(1,2) that is linked directly to a primary amine via a C2 linker (Figure 3.3). Hence, the lower amount of CO_2 adsorbed for AAMS(1,2) can be explained by predominately protonated secondary amine groups that cannot be deprotonated by surface Si-OH groups at adsorption temperatures and therefore do not interact with CO_2. Figure 3.5 shows the arrangement and interaction of vicinal aminosilanes during adsorption of CO_2. The sorption of

APTMS(1) and AAMS(1,2) follows the intermolecular carbamate mechanism as reported before between two primary amine groups in a water free environment (Equation 3.1). [114]

$$2\ R_1NH_2 + CO_2 \quad \rightleftharpoons \quad R_1NH_3^+ + R_1NH_2COO^- \tag{3.1}$$

$$R_1NH_3^+ + R_1NH_2 + CO_2 \quad \rightleftharpoons \quad R_1RNH_3^+ + R_1NHCOOH \tag{3.2}$$

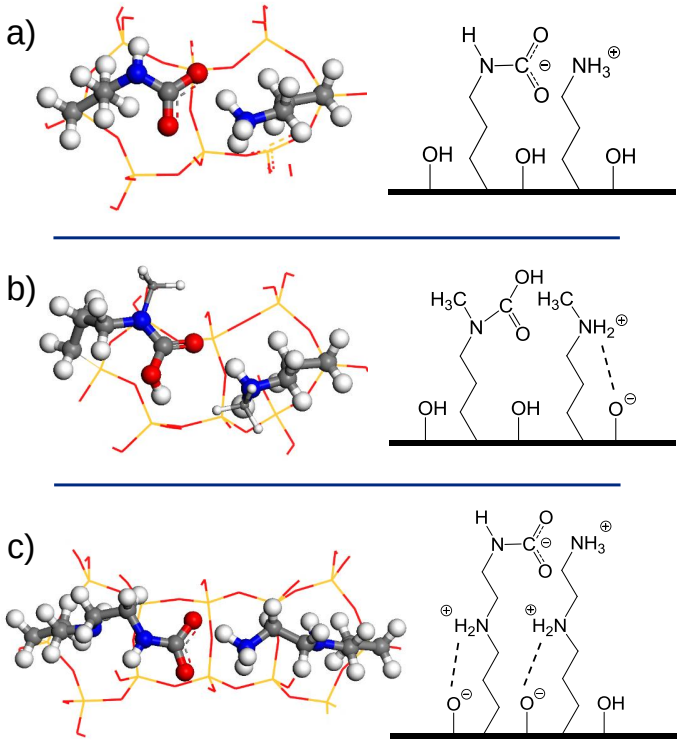

Figure 3.5: Adsorption of CO_2 on (a) APTMS(1), (b) MAPS(2) and (c) AAMS(1,2) via intermolecular stabilization of carbamates (a, c) and formation of carbamic acid (b) on a silica cluster with vicinal aminosilane interaction. Molecular structure is displayed in topview.

It is important to point out that the DFT calculations suggest that the stabilization of the carbamate requires not only protonation of a second amine group, but also the presence of vicinal Si-OH groups. Carbamic acid can only be stabilized when the formation of a carbamate is suppressed by surrounding protonated amines that prevent further protonation (Equation 3.2). As mentioned above, the protonation and deprotonation via Si-OH groups is reversible for primary amines, thus allowing a permanent exchange of protons with the surface. Therefore, the binding energies of APTMS(1) and AAMS(1,2) are significantly higher for carbamates than carbamic acid (Table 3.4). The IR spectra of APTMS(1)

and AAMS(1,2) only exhibit a weakly defined band around 1690 cm^{-1} characteristic for C=O stretching vibration in carbamic acid. The corresponding OH deformation band at 1380 cm^{-1} is little pronounced in APTMS(1) and not even existing for AAMS(1,2). In conclusion, the low binding energy for protonation of primary amines facilitates protonation deprotonation via surface Si-OH groups and thereby limits the possibility to stabilize carbamic acid.

Table 3.4: Binding energies of CO_2 on vicinal aminosilanes that allow intermolecular amine interactions. Determined by computational quantum mechanical modeling.

APTMS(1)	MAPS(2)	AAMS(1,2)	
		Primary	Secondary
-66	-52	-60	-
-43	-68	-42	29

In contrast, the higher activation energy for the deprotonation of secondary amines (Table 3.3), enables the stabilization of carbamic acid for MAPS(2) (Equation 3.3) by protonated amines that is evident in the IR spectra by the pronounced bands at 1687 and 1384 cm^{-1} (Figure 3.3).

$$R_1R_2NH_2^+ + R_1R_2NH + CO_2 \quad \rightleftharpoons \quad R_1R_2NH_2^+ + R_1R_2NCOOH \tag{3.3}$$

$$2\ R_1R_2NH + CO_2 \quad \rightleftharpoons \quad R_1R_2NH_2^+ + R_1R_2NHCOO^- \tag{3.4}$$

The formation of a limited amount of carbamates for MAPS(2) cannot be totally excluded by IR spectroscopy. However, the binding energy of carbamic acid is 16 kJ mol^{-1} higher compared to the formation of carbamates (Table 3.4). It is conceivable that carbamic acid is further stabilized to carbamates when the protonation of secondary amine groups is limited by access to surface Si-OH groups at low amine spacing (Equation 3.4). In summary, two amine groups are required for the adsorption of one CO_2 molecule for both APTMS(1) and MAPS(2) on silanol surfaces at medium amine concentrations, resulting in a maximum efficiency of 50 %. Higher amine efficiencies were only reported by formation of carbamic acid with sterically hindered amines structures in solvent environments that prohibit excessive deprotonation.[92–97] The inactivity of the secondary amine group in AAMS(1,2) leads to the necessity to provide four amine groups within two bifunctional aminosilanes to capture one carbon dioxide molecule and therefore are not suitable for efficient CO_2 capture with a limited maximum amine efficiency of only 25 %.

3.3.3 Effect of the Amine Concentration on the Amine Efficiency

Adsorption isotherms and heats of adsorption (ΔH_{ads}) were recorded for APTMS(1), MAPS(2) and AAMS(1,2) at medium amine concentrations ($3.30 \pm 0.01\,\mathrm{mmol\,g^{-1}}$) at increasing CO_2 partial pressures (Figure 3.6). According to the mechanistic assumptions, the adsorption isotherms of APTMS(1) and MAPS(2) exhibit a similar trend with a maximum uptake at 100 mbar, which is about 50 % higher compared to AAMS(1,2). The higher sorption capacities for mono-functionalized amines compared to bifunctional amines is in agreement to the spectroscopic data and the results of the DFT calculations.

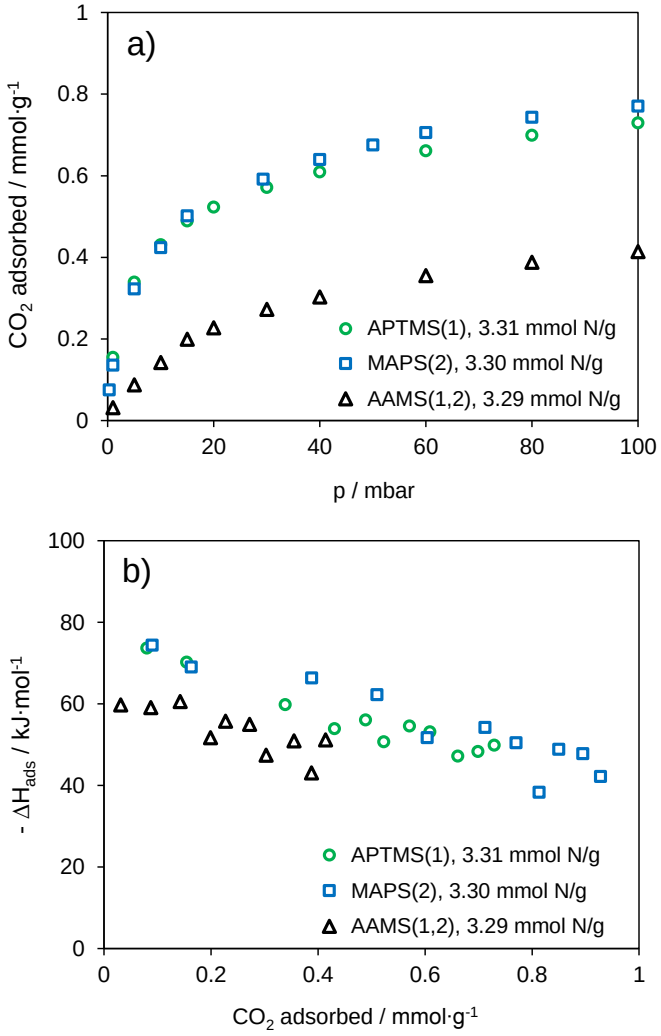

Figure 3.6: (a) Adsorbed CO_2 over the CO_2 partial pressure and (b) heats of adsorption versus adsorbed CO_2. Values determined by TGA DSC out of vacuum at 50 °C.

The initial heats of adsorption of both APTMS(1) and MAPS(2) were approximately $75\,\mathrm{kJ\,mol^{-1}}$, which is in the range of values reported for these partial pressures.[114] Alkhabbaz et al. also observed essentially identical heats of adsorption for primary and secondary amine groups.[114] The decrease of initial heats of adsorption for increasing concentrations

of CO_2 adsorbed is most likely a result of sterical hindrances between adsorbed species. It should be noted that the heats of adsorption are below $30\,kJ\,mol^{-1}$ for bare SiO_2 spheres due to physical adsorption only (Table 3.5). The heats of adsorption for AAMS(1,2) were $60\,kJ\,mol^{-1}$, which can be associated to the higher amine spacing and lower concentration of the capture active primary amines, thus decreasing the binding energy of intermolecular CO_2 adsorption. [114]

Table 3.5: Adsorbed CO_2 and heats of adsorption on calcined APTMS(1), MAPS(2) and AAMS(1,2) determined by TGA under flow conditions (quasi equilibrium).

	CO_2 adsorbed / $mmol\,g^{-1}$	ΔH_{ads} / $kJ\,mol^{-1}$
APTMS(1)_calc	0.10	-28
MAPS(2)_calc	0.07	-23
AAMS(1,2)_calc	0.04	-24

The CO_2 equilibrium uptake normalized to the amine concentration (i.e. the amine efficiency) for APTMS(1), MAPS(2) and AAMS(1,2) for amine concentration between 1.3 and $3.6\,mmol\,g^{-1}$ determined at 100 mbar under flow conditions is illustrated in Figure 3.7. The non-normalized equilibrium uptake is illustrated in the Appendix Figure A.3. The amine efficiencies of APTMS(1), MAPS(2) and AAMS(1,2) at an amine loading of $3.3\,mmol\,g^{-1}$ were 23 %, 21 % and 12 %, respectively. As discussed above, the functionality of the amines determines the maximum efficiency, which is 50 % for APTMS(1) and MAPS(2) and only 25 % for AAMS(1,2). However, the encapsulation of amine groups into the SiO_2 spheres during synthesis cannot be excluded, which would significantly lower the achievable amine efficiency by a limited access of CO_2 to the adsorption sites (see Section 3.3.1). At low amine concentrations (below 10 %) the amine efficiency significantly decreased to roughly 6 % independent of the employed aminosilanes (Figure 3.7). Moreover, the heats of adsorption (ΔH_{ads}) dropped to values as low as $40\,kJ\,mol^{-1}$ (Figure 3.7). At large distances between the amine groups on SiO_2 (i.e., low amine density) CO_2 adsorption via intermolecular amine stabilization is not possible for monofunctional amines and computational quantum mechanical modelling reveals that CO_2 can only be captured on APTMS(1) and MAPS(2) by the formation of energetically less preferred carbamic acid (Figure 3.8, Table 3.6).

Table 3.6: Binding energies of CO_2 on single aminosilanes with no intermolecular amine interaction. Determined by computational quantum mechanical modeling.

APTMS(1)	MAPS(2)	AAMS(1,2)	
		Primary	Secondary
-	-	-39	-
-20	-25	-23	29

The DFT calculations also show that intramolecular carbamate formation is energetically favored for AAMS(1,2) when intermolecular amine interaction is not possible (Table 3.6). However, the majority of the secondary amine groups is protonated by surface silanol groups and thus formation of carbamic acid is also the predominant adsorption mechanism for AAMS(1,2) (Figure 3.8 c, d).

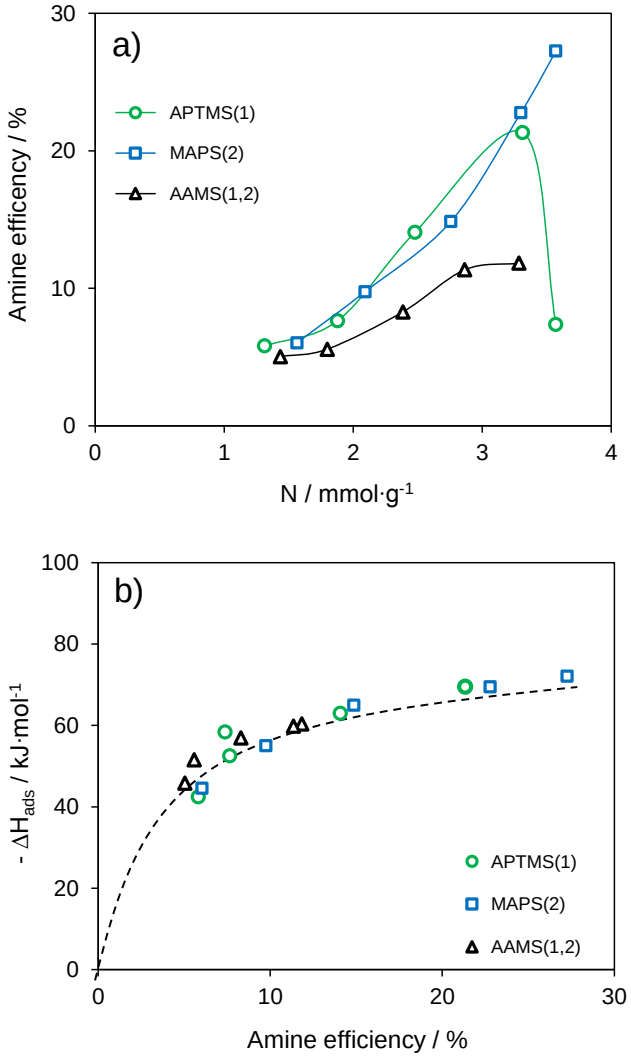

Figure 3.7: (a) Amine efficiency over the amine concentration of the adsorbents and (b) correlation between the heats of adsorption and amine efficiency. Values determined by TGA DSC under flow conditions at 50 °C.

Carbamic acid cannot be sufficiently stabilized due to a lack of vicinal amines, resulting in lower binding energies compared to the sorption on samples with higher amine densities (Table 3.6). Hence, missing intermolecular amine interaction limits the amine efficiency for low amine densities. At higher amine concentrations, CO_2 adsorption is not restricted by intermolecular amine interaction. However, high amine densities decrease and sterically restrict the access to surface Si-OH groups (see Appendix Figure A.5 for IR spectra). As a

consequence, protonation and deprotonation of the amine groups are hindered. As noted above, formation of carbamates, the dominant capture mechanism for primary amines, requires a second non protonated amine group in close proximity in order to be stabilized. Without charge compensation via the surface, the energetically non-favored formation of carbamic acid prevails for the CO_2 sorption of primary amines, which results in an overall decrease of adsorption capacity. A similar transition in the adsorption mechanism is proposed for AAMS(1,2) at higher amine loadings. However, the long alkyl chain of AAMS(1,2) strongly affects the morphology and restricts the formation of structured sorbents for higher amine concentrations (see Section 3.3.1). The CO_2 adsorption capacity of MAPS(2) further increases with higher amine concentrations, as the stabilization of carbamic acid does not require deprotonation of neighboring amine groups by the surface. The lack of access to the surface silanol groups limits the amine efficiency for primary amine groups in APTMS(1) and AAMS(1,2) at high amine densities. Hence, solid sorbents functionalized with secondary amine groups are most applicable to achieve adsorbents combining high amine loadings with high CO_2 uptake capacities.

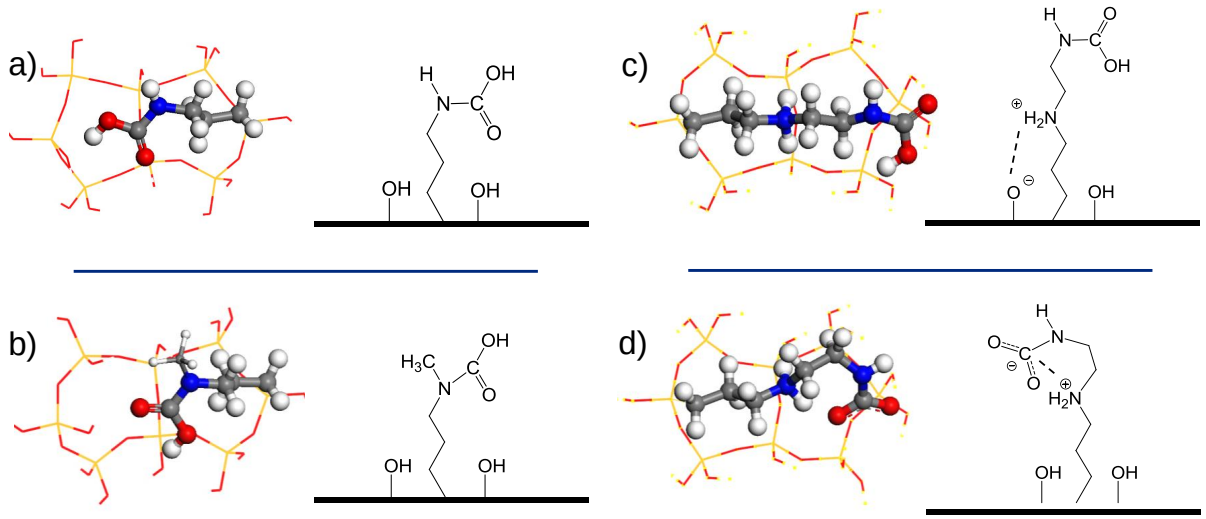

Figure 3.8: Adsorption of CO_2 on (a) APTMS(1), (b) MAPS(2) and (c, d) AAMS(1,2) via carbamic acid (a, c, b) and carbamate (d) on a silica cluster without intermolecular aminosilane interaction. Molecular structure is displayed in topview.

3.3.4 Adsorption-Desorption Properties and Long Term Cycle Stability

The long term stability of an amine functionalized adsorbent is strongly influenced by the level of flue gas contamination (SO_x, NO_x, H_2O etc.) and the desorption conditions applied. Sayari reported that secondary amines exhibit a higher resistance against thermal degradation compared to primary amines when no H_2O is present in the adsorption process.[89] The gaseous H_2O content in industrial flue gas streams (up to 15 vol.%) hinders thermal degradation via hydrolysis independent of the amine functionality.[115] The amine content of the sorbents for long term studies was selected to yield the highest CO_2 uptake capacities (Figure 3.7). 10 adsorption desorption cycles were conducted for each adsorbent (Figure 3.10). The amine efficiency remained constant over 10 cycles and was 20 % for APTMS(1), 25 % for MAPS(2) and 10 % for AAMS(1,2). The hierarchical structure of APTMS(1), MAPS(2) and AAMS(1,2) allowed the complete desorption of the sorbents in a stream of nitrogen already at 75 °C (Figure 3.9). In contrast to well ordered supports with a narrow and uniform pore size distribution (e.g. SBA-15, MCM-41) the hierarchical structure of the applied sorbents facilitate fast desorption kinetics and minimize re adsorption (see Section 3.3.1).[64,101] No changes were observed for the heats of adsorption (ΔH_{ads}) over time and thus degradation and changes in adsorption mechanism can be excluded. In summary, the amine functionalized SiO_2 spheres achieve excellent adsorption-desorption long term properties for all employed aminosilane even without the presence of H_2O.

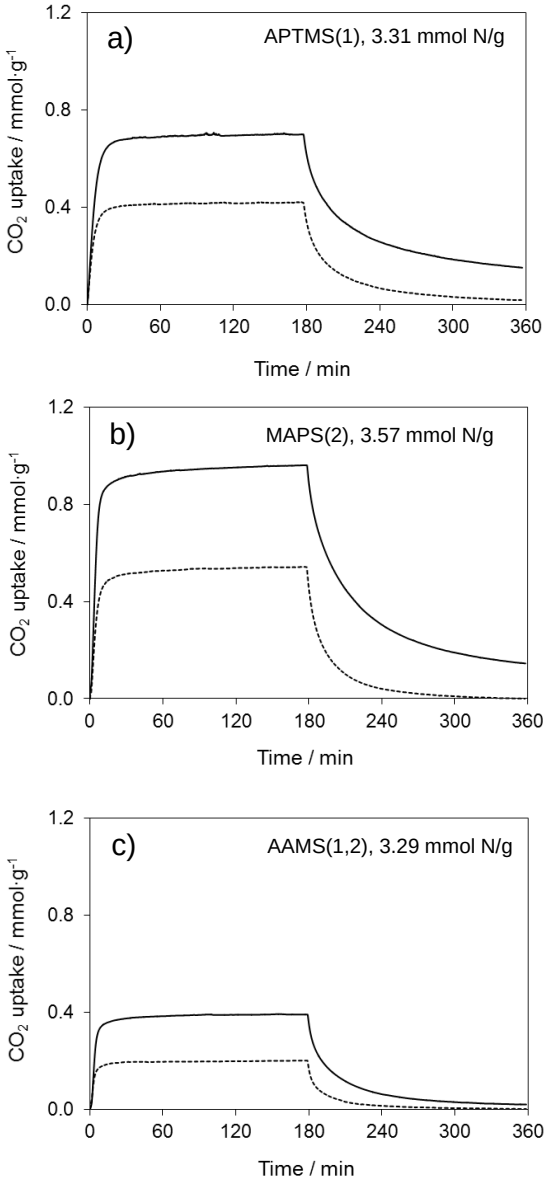

Figure 3.9: CO_2 adsorption-desorption of (a) APTMS(1), (b) MAPS(2) and (c) AAMS(1,2). Adsorption for 180 min under atmospheric flow conditions (50 °C, 10 vol.% CO_2 in N_2) followed by a 180 min desorption section in pure N_2. Constant adsorption-desorption temperature of 50 °C (solid line) and 75 °C (dotted line).

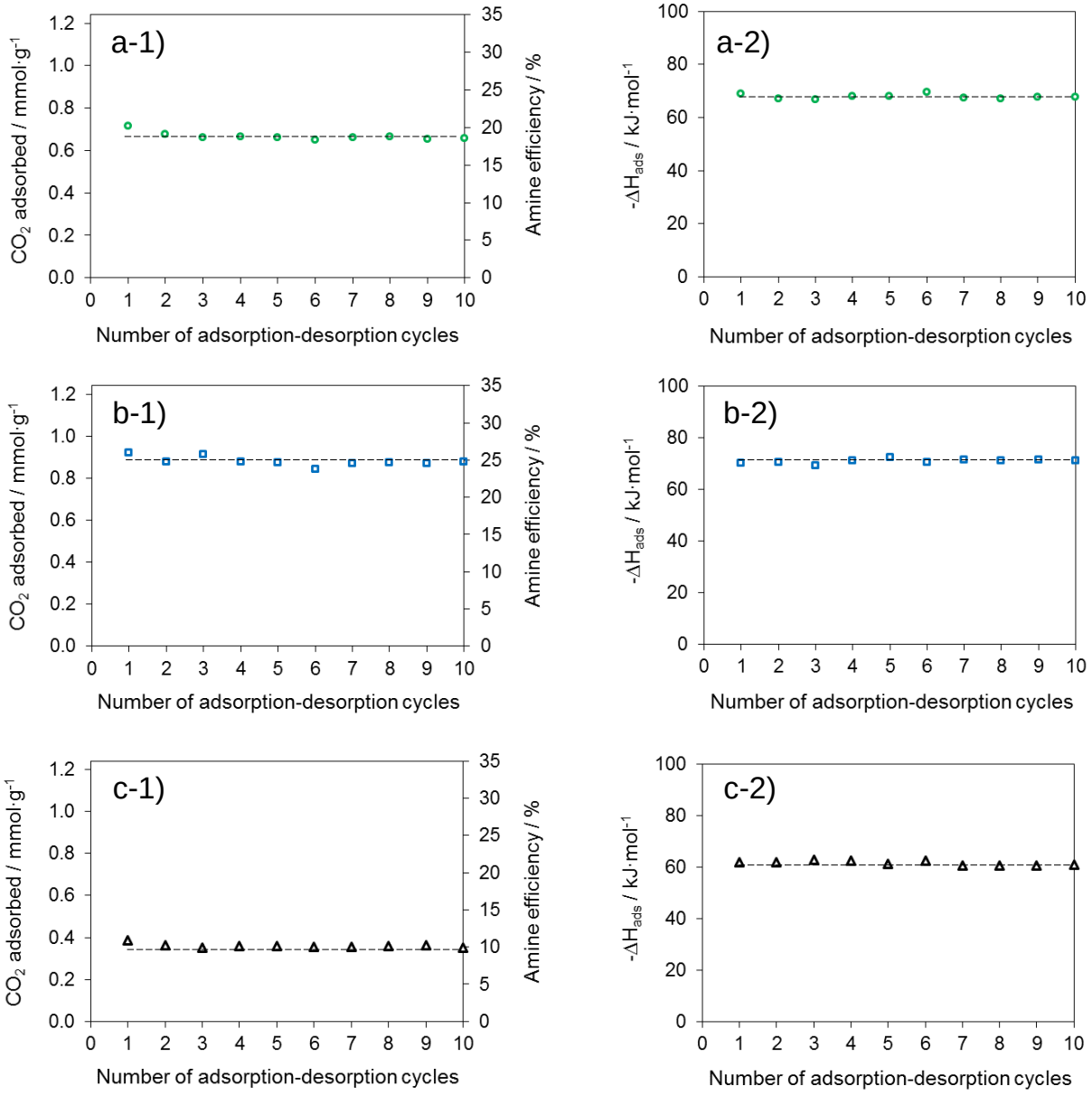

Figure 3.10: Temperature-swing multicycle CO_2 adsorption of (a) APTMS(1), (b) MAPS(2) and (c) AAMS(1,2) over 10 cycles. Values determined by TGA DSC under flow conditions at 50 °C and desorption at 75 °C in a flow of pure N_2. (1) Adsorbed CO_2 and (2) heats of adsorption.

3.4 Conclusion

The concept of amine functionalized, hierarchically structured adsorbents for CO_2 capture facilitates the full recovery of the adsorption capacity already at low temperature (75 °C) and thereby the thermal degradation of the adsorbents could be prevented. The water free CO_2 adsorption mechanism of aminosilanes, immobilized on silanol surfaces, is dependent on the functionality of the amine as well as on the interaction between the amine groups with a sufficient access to Si-OH groups. Small amine spacing enhances the amine efficiency by facilitating intramolecular stabilization of the adsorption species and, therefore, it is crucial to provide a minimum number of vicinal amine groups in the adsorbent for CO_2 capture materials. Under these conditions, intermolecular stabilized carbamates and carbamic acid are the predominant adsorption species for monofunctional primary and secondary aminosilanes on silanol surfaces, respectively. The requirement of two amine groups to capture one CO_2 molecule limits the maximum achievable water-free amine efficiency of primary and secondary amine groups in a protic environment to 50 %. Large spacing between the amine groups restrict intermolecular amine interaction and therefore limit CO_2 adsorption to the formation of energetically non favored carbamic acid stabilized via surface Si-OH groups independent of the amine functionality. Bifunctional aminosilanes are restricted to carbamate formation solely via primary amines because the close proximity of the amine groups enhances the protonation of the energetically favored secondary amine group by surface Si-OH groups prior to the adsorption of CO_2. Therefore, intramolecular carbamate formation is hindered and the amine efficiency is reduced to a maximum of 25 % by leaving the primary amines as the only active species. When the amine densities exceeds a certain level of accessibility of aminosilanes to the surface, protonation-deprotonation of amine groups by surface Si-OH is significantly constrained. Stabilization and especially deprotonation of the adsorption species is crucial for primary amines and leads to a rapid drop once the level of amine spacing is exceeded. In conclusion, the low access to surface silanol groups at higher amine densities constrains the formation of carbamates on primary amines and , therefore, secondary amines are more suitable when high CO_2 uptake capacities are required.

3.5 Experimental Section

3.5.1 Synthesis

SiO_2 spheres were synthesized by the base catalyzed condensation reaction reported before.[101] Phenyltrimethoxysilane (PTMS, purity $\geq$ 97 %), (3-aminopropyl)trimethoxysilane (APTMS, purity $\geq$ 97 %), trimethoxy[3-(methylamino)propyl]silane (MAPS, purity $\geq$ 97 %), N-[3-(trimethoxysilyl)propyl]ethylendiamine (AAMS, purity $\geq$ 97 %) and benzyl alcohol (purity $\geq$ 99 %) were purchased from Sigma Aldrich. Tetraethylorthosilicate (TEOS) and the copolymer Pluronic RPE 1740 were provided by WACKER and BASF, respectively. All chemicals were used without any additional purification. The reactor column was filled with deionized (DI) water. The surfactant containing precursor solution was prepared by mixing 5.4 g of the surfactant Pluronic RPE 1740 ($(PO)_{11}(EO)_{27}(PO)_{11}$)[62] and 5.9 g of benzyl alcohol. The Si precursor rich solution contained 6.0 g tetraethylorthosilicate (TEOS), 4.3 g of phenyltrimethoxysilane (PTMS) and the according concentration of (3-aminopropyl)-trimethoxysilane (APTMS), trimethoxy[3-(methylamino)propyl]silane (MAPS) and N [3-(trimethoxysilyl)propyl]ethylendiamine (AAMS). Both solutions were merged and mixed prior to injection to the water filled reactor column. The reaction conditions as well as a detailed description of the synthesis steps are also presented in the previous chapter.[101] The spheres were directly formed by micelle formation and base catalyzed condensation.[101] Afterwards they were aged in deionized (DI) water and washed with copious amounts of DI water and ethanol. In order to remove residual solvents, the SiO_2 spheres were dried overnight (as-prepared SiO_2 spheres). Soxhlet extraction was performed for 24 h at 90 °C in ethanol to decrease the amount of residues surfactants (soxhleted SiO_2 spheres). Calcination in synthetic air (100 mL min^{-1}) at 600 °C for 6 h with a heating rate of 2 °C min^{-1} ensured the total removal of all remaining organic compounds (calcined SiO_2 spheres).

3.5.2 Characterization

The C, H and N contents of the SiO_2 spheres were determined by combustion analysis with a thermal conductivity detector (TCD). Powder X-ray diffraction (XRD) patterns were measured on a Philips X'pert diffractometer with an X'celerator module (Cu Kα radiation). All diffractograms were measured with a step size of 0.033 ° in the specific range of 2Θ = 5° - 40°. A QUADRASORB SI automated surface area and pore size analyzer was used to determine surface area, micro- and mesopore volume as well as the pore size distribution by nitrogen physisorption at −196 °C. All sorbents were outgassed under vacuum at 100 °C for 1 h on a Quantachrome FloVac degasser. The Brunauer-Emmett-Teller (BET) method[83] was applied to quantify the surface area and the micropore volume (pore size < 2 nm) was determined via the t plot method[116]. The mesopore volume (pore size: 2 - 50 nm) and pore size distribution were calculated by the Barrett-Joyner-Halenda

(BJH) model[85] on the desorption branch of the isotherm. IR spectra of SiO_2 spheres were obtained from self-supporting wafers in a vacuum set-up. A detailed description of the method is presented below.

3.5.3 In-Situ Infrared Spectroscopy

IR spectra of SiO_2 spheres were recorded on a Bruker VERTEX 70 spectrometer with a mercury cadmium telluride (MCT) detector. A self-supporting wafer (ca. 10 mg cm^{-2}) was placed in a vacuum IR cell with CaF_2 windows. Before each measurement, the wafer was activated at 100 °C for 1 h under vacuum (p = 10^{-6} mbar). CO_2 was adsorbed on the sample at 50 °C and 1.0, 2.0, 4.0, 8.0 and 10 mbar. 128 scans were collected with a resolution of 4 cm^{-1} for each spectrum. All spectra were baseline corrected and normalized to the intensity of Si-O overtone resonances in the range of 2095 - 1755 cm^{-1}.

3.5.4 CO_2 Adsorption

CO_2 adsorption isotherms and the heats of adsorption, determined by differential scanning calorimetry (DSC), were obtained under static conditions on a Seteram TG DSC 111 thermo gravimetric analyzer (TGA) at 50 °C and up to CO_2 partial pressures of 100 mbar. Before each measurement, all samples were heated at 100 °C for 1 h under vacuum to ensure the removal of residual water and solvents. Additionally, a Setaram Sensys Evo TGA was used to detect the heats of adsorption (DSC) and adsorbed amount of CO_2 under atmospheric flow conditions. Roughly 20 mg of each sample was placed in a platinum crucible and dried under a N_2 flow of 16 mL min^{-1} at 100 °C for 1 h. The sample was cooled down to the adsorption temperature of 50 °C and 10 vol.% CO_2 was added to the N_2 stream while the total flow remained constant. The adsorption time to obtain quasi equilibrium adsorption isotherms was set to 60 min.

The adsorption and desorption experiments (concentration swing with N_2) were carried out for 180 min at constant temperatures of 50 °C and 75 °C in a Setaram Sensys Evo, respectively. Additionally, adsorption was carried out for 3 h at 50 °C under atmospheric flow conditions (10 vol.% CO_2 in N_2) followed by a 3 h desorption section in pure N_2 at 75 °C for 10 times to obtain multi cycle experiments.

3.5.5 DFT Calculations

The interactions of CO_2 with grafted aminosilanes were determined by density functional theory (DFT) calculations applying the all-electron full-potential code FHI-aims.[117,118] Electronic exchange and correlation was treated on the level of the generalized gradient approximation (GGA) BLYP functional as well as on the level of the hybrid B3LYP functional.[119–121] Dispersive interactions not considered at these levels of theory were taken into account by applying the dispersion-correction scheme by Tkatchenko and Scheffler

(TS).[122] Geometry optimization was performed at the BLYP+TS level and using tight tier1 basis sets until residual forces fell below 10^{-4} eV Å^{-1}. Subsequent, single point calculations on these geometries at hybrid B3LYP+TS level yield the finally presented numbers. The surface of the SiO_2 spheres was modeled with two clusters: a small one consisting of 8 SiO_2 units, and a larger one consisting of 12 SiO_2 units. The small cluster is large enough to host two APTMS(1) or MAPS(2), as well as one AAMS(1,2). The larger cluster was used to represent higher loadings of AAMS(1,2). During the geometry optimization, all of the atoms in the clusters were allowed to relax.

The proton affinity (p_a), defined as the negative reaction enthalpy, is calculated for primary, secondary and bifunctional aminosilanes by Equation 3.5 below:

$$p_a = -\Delta H = -\Delta E + R \cdot T = -\Delta E_{el} - \Delta ZPE + \frac{5}{2} R \cdot T \tag{3.5}$$

ΔE_{el} is defined as the change in the electronic energy and ΔZPE as the change of the zero point energy of the normal modes.

3.6 Associated Content

Additional Information

CO_2 adsorption data, IR spectra and the according peak assignment are listed in the Appendix A.2.

Peer-Reviewed Publication

This chapter is based on the following article: Maximilian W. Hahn, Jelena Jelic, Edith Berger, Karsten Reuter, Andreas Jentys and Johannes Lercher, The Role of Amine Functionality to the CO_2 Capture Mechanism on Silanol Surfaces, *submitted to J. Am. Chem. Soc.*, **2015**

Clearance by the Publisher

Notes and Author Contributions

Quantum mechanical modeling was performed by Jelena Jelic and Karsten Reuter. Edith Berger was acknowledged with Co-Authorship of the article, because of her contribution to the fundamental understanding of the adsorption processes in her earlier work.

Poster Presentations

M.W. Hahn, J. Jelic, E. Ball, K. Reuter, A. Jentys, J.A. Lercher, The role of amine functionality to the CO_2 capture mechanism of anhydrous solid sorbents, presented at the 48^{th} *Jahrestrefffen Deutscher Katalytiker* **3/2015**. Weimar, Germany.

4 Mechanism and Kinetics of CO_2 Adsorption on Surface Bonded Amines

4.1 Abstract

The impact of H_2O on the mechanism and kinetics of CO_2 adsorption by amine-impregnated SBA-15 has been investigated.[1] The H_2O-free adsorption mechanism proceeds predominantly via formation of carbamates stabilized between two amine groups. Bicarbonates and surface stabilized carbamates were formed on hydrated sorbents. Film diffusion limitations were not observed during adsorption of CO_2 at high amine loadings. Gaseous water decreased the adsorption rate but increased the maximum equilibrium uptake as well as the uptake before breakthrough of the reactor bed. A water film is formed on the adsorbent particles in gas streams containing more than 5 vol.%, gaseous H_2O limiting the interaction of CO_2 with the active amine sites and constraining the rates of adsorption. The higher uptake of CO_2 in the presence of H_2O vapor is a result of a change in the adsorption mechanism that increases the amine efficiency, thus leading to a higher adsorption capacity. The adsorption was fully reversible for all adsorbents at a maximum desorption temperature of 100 °C.

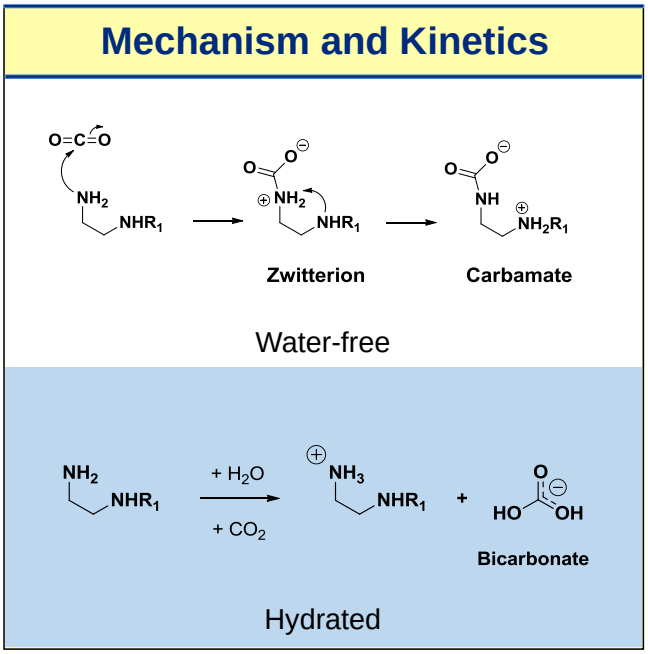

[1] This chapter is based on the article of the same title as currently in press at the Journal of Physical Chemistry C. Copyright 2015 American Chemical Society.

4.2 Introduction

The high cost of the amine wash based post-combustion capture (PCC) lead to an increased research in the development of solid, mostly SiO_2 based, sorbents that allow a less energetic regeneration step by lowering the overall heat capacity of the adsorbents ($c_p(H_2O) = 4.18\,kJ\,kg^{-1}\,K^{-1}$, $c_p(SiO_2) = 0.8\,kJ\,kg^{-1}\,K^{-1}$).[26,27,29–36] The use of solid sorbents impregnated with primary and secondary amines is still the economically most promising option. The adsorption of CO_2 on amine functionalized solid sorbents proceeds predominantly by the carbamate mechanism; the formation of carbamic acid is also a widely discussed possibility (Scheme 4.1).[44,110]

Scheme 4.1: CO_2 adsorption on bifunctional amines (primary and secondary amine groups) via (a) the carbamate mechanism and by (b) the formation of carbamic acid.

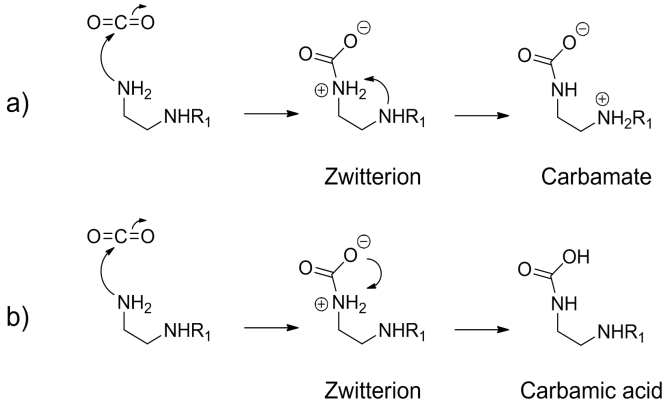

Highly-ordered adsorbents like zeolite 13X and most metal organic frameworks (MOFs) that achieve high CO_2 uptakes are not suitable for PCC because the CO_2 capture capacities are decreased by the strong adsorption of 5 - 15 vol.% H_2O vapor in the exhaust gas formed in the combustion process.[51,101,123–125] Moreover, the lack of thermal stability constitutes a limitation for the application due to thermal degradation during desorption when H_2O is present.[123,126,127] In contrast, it has been widely reported that the CO_2 uptake by solid amine-based systems increases in the presence of H_2O due to the formation of bicarbonates (Scheme 4.2).[115,128]

Scheme 4.2: CO_2 adsorption on bifunctional amines via formation of bicarbonates by a (a) primary and (b) secondary amine group.

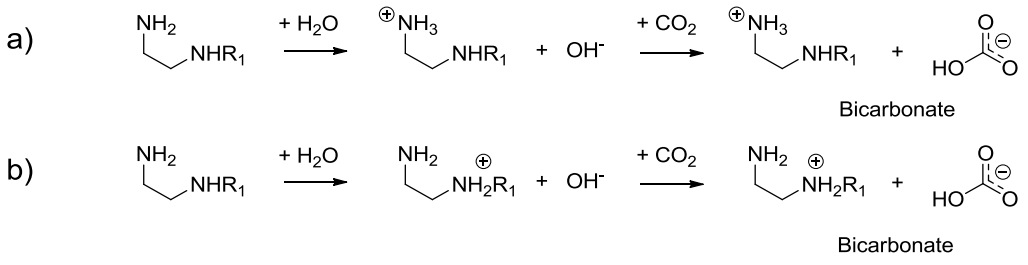

The presence of H_2O will strongly influence the heat and mass transfer of the sorbents. The formation of a water film on the adsorbent particles is likely when H_2O is present in the flue gas. Therefore, it is critical to understand the influence of water on CO_2 capture by amine-functionalized solid adsorbents.

In the present work, we studied the impact of amine type and loadings on the CO_2 adsorption mechanism and capacity of impregnated solid sorbents (Scheme 4.3). The adsorption mechanism and effect of diffusion limitations in non-hydrated sorbents was investigated by in-situ adsorption of CO_2 monitored by IR spectroscopy. Ex situ ^{13}C MAS NMR spectroscopy of adsorbed CO_2 was used to differentiate the adsorption mechanism of water-free and fully-hydrated adsorbents. The influence of H_2O on the adsorption kinetics was explored by performing breakthrough experiments with varying gaseous water contents of the simulated flue gas.

Scheme 4.3: Amines impregnated on SBA-15.

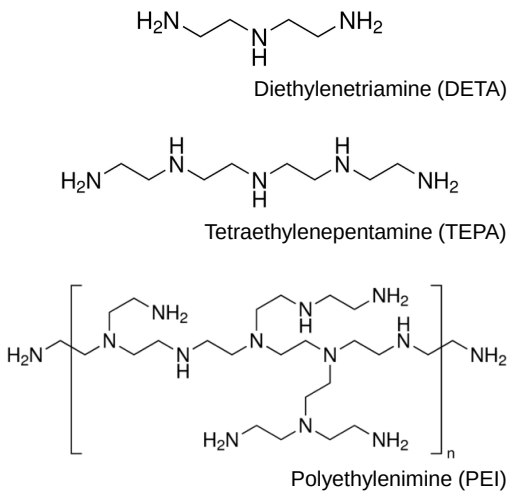

4.3 Results and Discussion

4.3.1 Structural Properties of Amine Impregnated SBA-15

The amine loadings of adsorbents were adjusted to achieve low and a high amine values for each of the three employed amine molecules. The resulting impregnated SBA-15 is denoted by the name of the amine followed by the amine loading in wt.% (e.g. TEPA 23) as illustrated in Table 4.1.

Table 4.1: Amine loading of impregnated SBA-15.

	Amine concentration -NH_x / mmol g^{-1}	Amine loading / wt.%
DETA 9	2.6	9.0
DETA 23	6.5	22.5
TEPA 9	2.6	9.0
TEPA 23	6.5	22.5
PEI 5	1.3	5.4
PEI 18	4.3	18.4

The low and high amine loadings were identical for SBA-15 impregnated DETA and TEPA and in both cases impregnation of PEI yielded lower amine contents (Table 4.1). The pores of SBA-15 have a sharp size distribution about 7 nm and only contain mesopores with a total volume of 0.84 mL g^{-1} (Figure 4.1, Table 4.2). The loss of amines after the drying procedure prior to N_2 physisorption can be neglected for all impregnated sorbents as illustrated in Table A.2 of the Appendix to this chapter.

Table 4.2: BET surface area, pore volume[a] and average pore size[a] of SBA-15 and amine impregnated SBA-15. [a] Determined by BJH method (desorption branch).

	BET surface area / $m^2\,g^{-1}$	Mesopore volume[a] / $cm^3\,g^{-1}$	Residual pore volume / %	Average pore size[a] / nm
SBA-15	737	0.84	100	6.6
DETA 9	303	0.75	89	6.1
DETA 23	272	0.61	73	5.3
TEPA 9	218	0.36	43	3.6
TEPA 23	65	0.28	33	3.3
PEI 5	429	0.66	79	4.9
PEI 18	257	0.48	58	4.6

The bulky polymeric structure of PEI (Scheme 4.3) was too large to enter the pores, which led to overall lower PEI loadings. The decrease in average pore size and mesopore volume compared to pure SBA-15 was tentatively attributed to a partial blocking of the pore entrances by the PEI molecules adsorbed on the outer surface of SBA-15 (Table 4.2). The pore size distributions narrowed when TEPA was used in the synthesis, but was unaffected for DETA and PEI impregnated sorbents (Figure 4.1, Figure A.6). The smallest amine, DETA, could easily enter the pores of SBA-15, whereas PEI preferably deposited on the outer surface of the support particles. The linear chain length of TEPA is approximately 1.5 nm and approximately 25 % of the average pore diameter of the support. Hydrogen bonding between TEPA and support terminal silanol groups will result in gradual deposition of TEPA already at the pore entrance. This results in an agglomeration of TEPA molecules in the pore mouth region for higher amine concentrations. As a direct consequence, the decreases in surface area, pore volume and average pore size are most pronounced for TEPA impregnated sorbents as shown in Table 4.2. The residual mesopore volume of TEPA 23 was only 33 % of the mesopore volume of pure SBA-15. DETA impregnated SBA-15 retained the highest residual pore volume with 89 % for the low and 73 % for the high amine loading (Table 4.2). The approximately 50 % smaller linear chain length of DETA compared to TEPA allowed an easy access to the pores and a homogenous deposition without pore blockage.

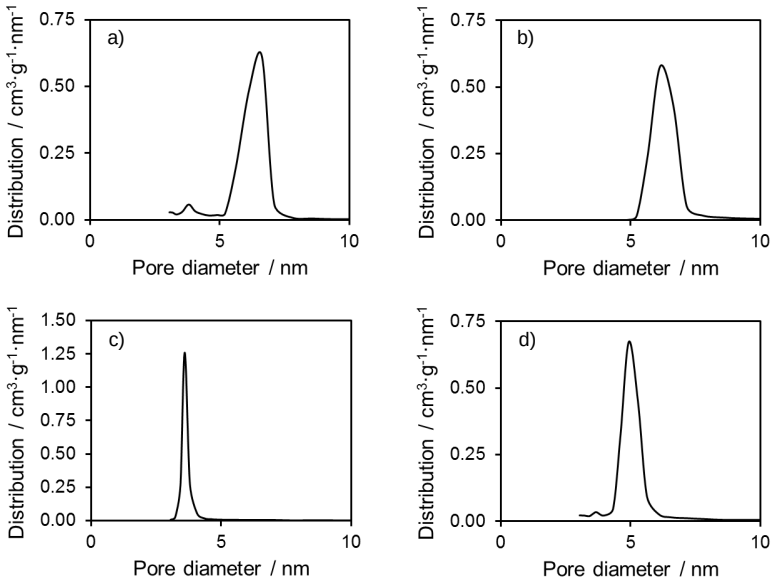

Figure 4.1: Pore size distribution (N_2 physisorption) of (a) SBA-15, (b) DETA 9, (c) TEPA 9 and (d) PEI 5.

4.3.2 Adsorption Mechanisms on Water-free and Fully-Hydrated Adsorbents.

CO_2 adsorption isotherms to a maximum pressure of 150 mbar of all amine impregnated adsorbents were recorded at 35 °C and 70 °C (Figure 4.2). The highest uptakes were observed by DETA and TEPA impregnated SBA-15. When PEI was used in the synthesis the resulting CO_2 uptake capacity was only one third compared to DETA and TEPA impregnated sorbents.

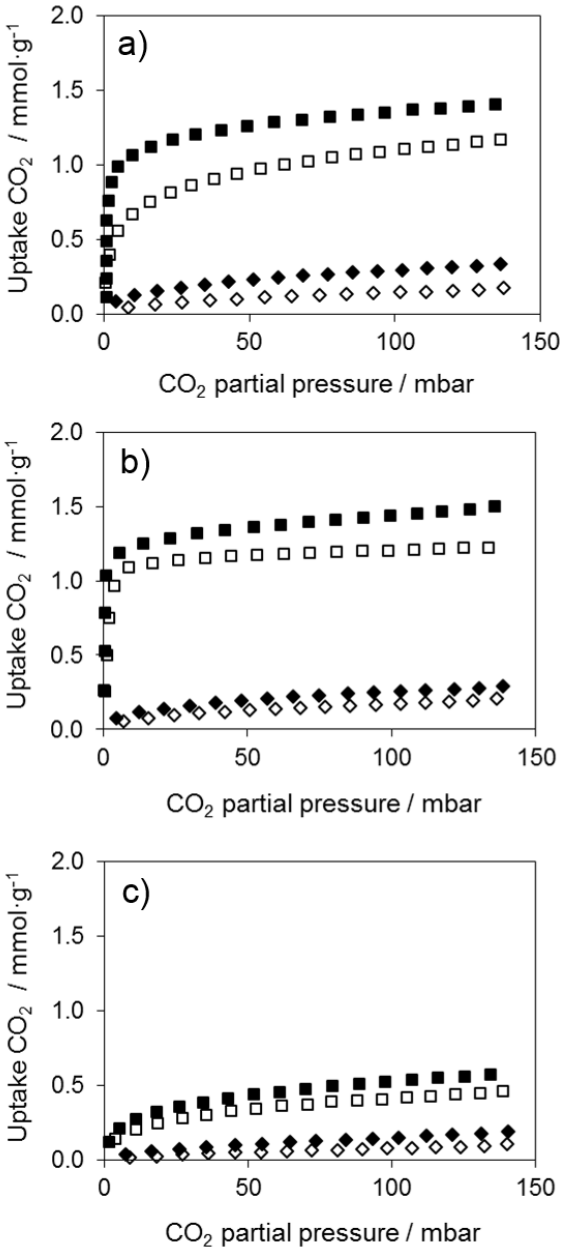

Figure 4.2: CO_2 Adsorption isotherms at 35 °C (filled symbols) and 70 °C (open symbols) of (a) DETA 9 (◇) and DETA 23 (□), (b) TEPA 9 (◇) and TEPA 23 (□), (c) PEI 5 (◇) and PEI 18 (□)

Those two amines with the shorter, linear chains present primary and secondary amine groups that are known to adsorb CO_2 via the carbamate mechanism under dry conditions (Scheme 4.1).[44] The molecular structure of PEI includes additional tertiary amines that link the chains containing primary and secondary amine groups on a branched structure (Scheme 4.3). Tertiary amine groups can only adsorb CO_2 via the bicarbonate mechanism and only when H_2O is present in the flue gas.[44] Moreover, tertiary amines cannot be protonated by primary and secondary amine groups, which leads to a further decrease in the adsorption capacities of PEI in a water-free environment by steric hindrance (Scheme 4.3).[44] As anticipated, the highest CO_2 uptakes were achieved by sorbents with the highest concentrations of amine equivalents. The amine efficiency (ratio of captured CO_2 per amine molecule) of DETA 23 and TEPA 23 was almost twice as high compared to the sorbents impregnated with lower amine loadings (Table 4.3).

Table 4.3: Temperature dependent amine efficiencies of amine impregnated SBA-15 at 100 mbar CO_2.

	Amine efficiency / %	
	35 °C	70 °C
DETA 9	11.5	5.4
DETA 23	21.0	17.0
TEPA 9	9.8	6.1
TEPA 23	18.3	14.4
PEI 5	11.9	6.4
PEI 18	12.2	9.6

Amines with a short molecular chain length tended to capture and stabilize adsorbed CO_2 between the amine molecules (intermolecular CO_2 adsorption) whereas the CO_2 adsorption proceeded via intramolecular stabilization for PEI (Scheme 4.3).[32,33,35,106] The higher the loadings of DETA and TEPA on the sorbent, the higher the degree of interaction, which in turn led to a higher amine efficiency (Table 4.3). The uptakes and amine efficiencies were higher at 35 °C than at 70 °C for all sorbents, as the regime was thermodynamically controlled under these conditions (Figure 4.2, Table 4.3).[129] The reverse trend is only possible when the maximum amine loading is very high and amine molecules in the pores are excluded from CO_2 interaction at low temperature because of severe pore mouth blockage.[130] The increase in temperature facilitates the mass transfer and together with a higher mobility of the amines the access by otherwise excluded amines is enhanced.[34] Overcoming this diffusion kinetic barrier then leads to a higher amine efficiency at higher temperatures.[130] The adsorption mechanism of CO_2 under water-free conditions on all sorbents was investigated by adsorption of CO_2 monitored by IR spectroscopy. The region between 1750 cm^{-1} and 1350 cm^{-1}, characteristic for the vibrations of the formed species,

is displayed in Figure 4.3. Additionally, the NH stretching bands of primary and secondary amines are shown in the Appendix Figure A.10. The spectra presented were obtained by subtracting the spectra of the activated samples before CO_2 adsorption from the equilibrated spectra. Please note, that the presented IR spectra give a qualitative information of the CO_2 adsorption mechanism. A quantitative argumentation is only valid for TEPA and PEI impregnated sorbents which were stable under the activation conditions. For DETA a partial desorption cannot be excluded when the activation temperature exceeds 70 °C (Figure A.7). The spectra could only be recorded up to a maximum pressure of 10 mbar CO_2 due to the strong overlapping absorbance of gas phase CO_2 around 2300 cm^{-1}. [131]

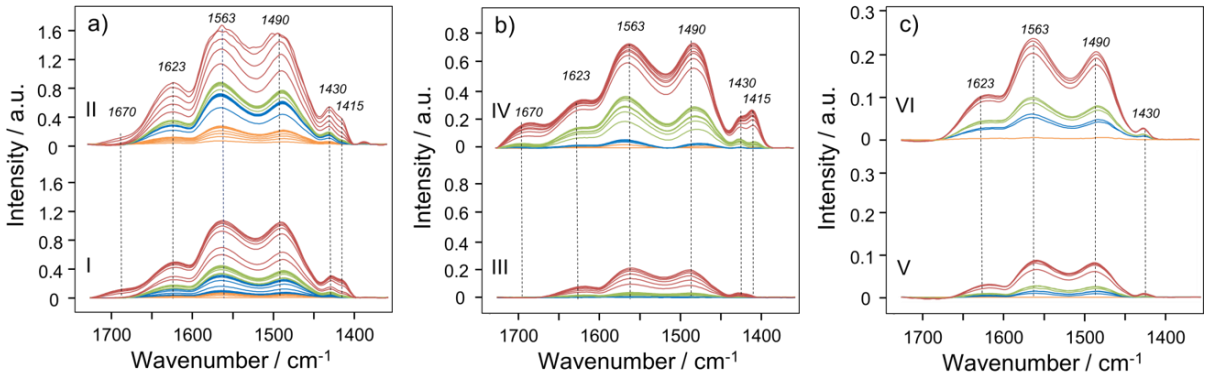

Figure 4.3: Differences IR spectra (1750 - 1350 cm^{-1}) taken every 120 s in a pressure range of 0.05 mbar-10 mbar: 0.05 mbar (-), 0.5 mbar (-), 1.0 mbar (-) and 10 mbar (-). (a) DETA 9 (I) and DETA 23 (II), (b) TEPA 9 (III) and TEPA 23 (IV), (c) PEI 5 (V) and PEI 18 (VI). Intensity in absorption units (a.u.).

The IR assignments of relevant peaks in the range of 1750 - 1350 cm^{-1} are listed in Table 3.2. A detailed peak assignment of the total adsorption spectra is given in the Appendix (Table A.3). The intensity of the peaks is higher for the sorbents with higher amine loadings independent of the amine used (Figure 4.3), which is in accordance with the results of the CO_2 adsorption isotherms (Figure 4.2). The peaks that are characteristic for the adsorption of CO_2 via the carbamate mechanism (1623 cm^{-1}, 1563 cm^{-1}, 1490 cm^{-1}, 1430 - 1415 cm^{-1}) were observed for all adsorbents and only TEPA 23 exhibited a peak at 1670 cm^{-1} that can be assigned to the CO stretching vibration of carbamic acid (Figure 4.3, Table 3.2). However, the corresponding band of the OH deformation in carbamic acid at 1380 cm^{-1} could not be observed. The CO stretching vibration at 1670 cm^{-1} was much less pronounced compared to the asymmetric COO^- stretching vibration at 1563 cm^{-1} and therefore formation of carbamic acid can be neglected (Figure 4.3, Table 3.2). Please note, that the exact surface coverage cannot be accessed without the knowledge of the extinction coefficients. Further confirmation of the formation of carbamic acid at wavenumbers below 1350 cm^{-1} was not possible due to the strong IR absorption by the SiO_2 matrix in this region. [74,76]

In order to determine the possible diffusion limitation of the CO_2 uptake capacity, caused either by the molecular weight of the amine or by the loading, the peaks of the species formed during dry adsorption were integrated in a pressure range between 0.05 mbar - 10 mbar CO_2 and plotted as a function of time (Figure 4.4). Diffusion coefficients were only calculated for TEPA and PEI impregnated sorbents, because the decrease in the amine loading for DETA after the activation step did not allow a further qualitative description. However, a diffusion coefficient similar to TEPA impregnated sorbents is anticipated according to a comparable size and structure. The resulting diffusion coefficients do not vary strongly and are 1-2·10^{-12} $m^2\,s^{-1}$ for TEPA and PEI impregnated sorbents with a standard deviation below 10 % (Table 4.4).

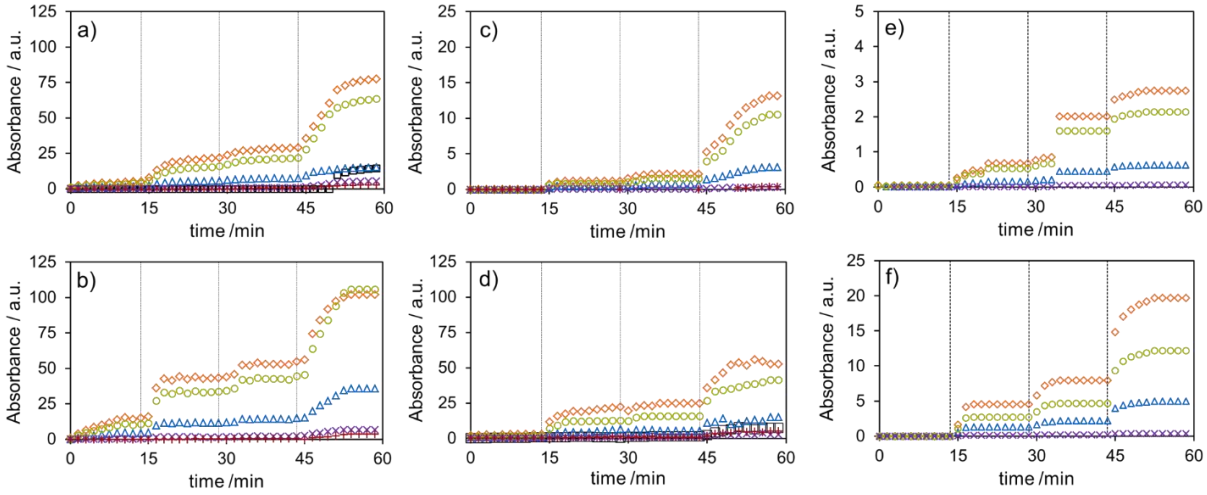

Figure 4.4: Time resolved IR peak areas of (a) DETA 9, (b) DETA 23, (c) TEPA 9, (d) TEPA 23, (e) PEI 5, (f) PEI 18. CO_2 partial pressures of (I) 0.05 mbar, (II) 0.5 mbar, (III) 1 mbar and (IV) 10 mbar. Resonances at (□) 1670 cm^{-1}, (Δ) 1630 cm^{-1}, (◇) 1463 cm^{-1}, (○) 1490 cm^{-1}, (×) 1430 cm^{-1} and (+) 1415 cm^{-1}.

Table 4.4: Diffusion coefficients of CO_2 in amine impregnated SBA-15.

	Diffusion coefficient / 10^{-12} $m^2\,s^{-1}$	Standard deviation / 10^{-12} $m^2\,s^{-1}$
TEPA 9	1.70	0.12
TEPA 23	1.69	0.09
PEI 5	1.97	0.05
PEI 18	2.13	0.02

External diffusion limitations could be neglected due to very low adsorption pressures. Therefore, the diffusion coefficients only account for bulk and pore diffusion. The diffusion coefficient of CO_2 in solid amine impregnated sorbents is by a factor of 1000 lower

compared to diffusion in amine solutions.[132] Bollini et al. investigated the time resolved adsorption of CO_2 in impregnated amines with low and high amine loadings but no diffusion coefficients have been reported to our knowledge so far.[133]

The proposed changes in the adsorption mechanism from carbamate formation under water-free conditions to bicarbonates in presence of H_2O has been explored by ^{13}C NMR as illustrated in Figure 4.5. TEPA 23 was selected, because the TEPA molecule has a low vapor pressure and contains only primary and secondary amine groups. CO_2 was ex situ adsorbed on non hydrated (Figure 4.5a) and fully hydrated (Figure 4.5b) TEPA 23 prior to the measurements. The NMR peak at 164.7 ppm of non hydrated TEPA 23 was assigned to the formation of carbamates on amine functionalized solid sorbents.[37,134] Park et al. investigated the adsorption species in monoethanolamine (MEA) solutions and assigned the peak at 162.4 ppm to bicarbonates.[135] However, a second peak with a higher chemical shift than of a carbamate, as observed in Figure 4.5b, was not observed in the aqueous phase.

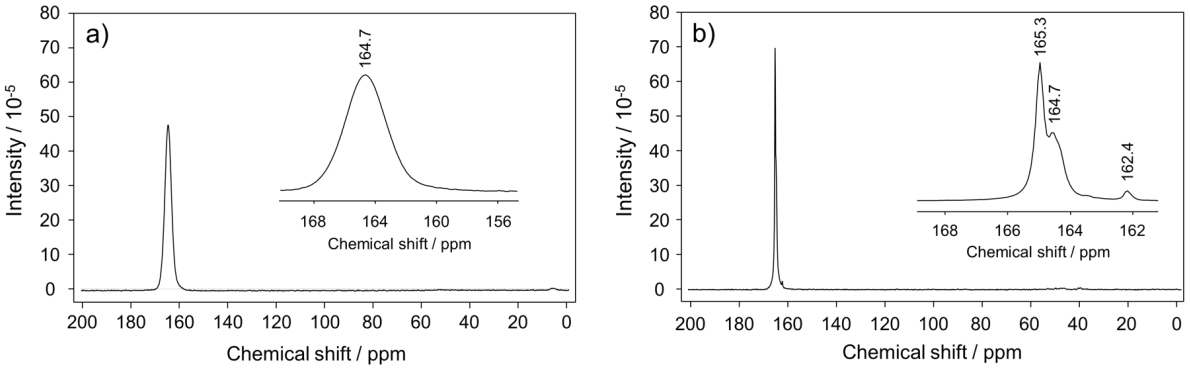

Figure 4.5: ^{13}C solid state NMR of $^{13}CO_2$ ex-situ adsorbed on (a) water-free and (b) fully-hydrated TEPA 23.

It should be noted that the F1 shift of carbamates formed in the liquid phase is about 1 ppm higher compared to carbamates formed on dry amine functionalized solid sorbents.[135] Therefore, we propose that an additional carbamate species is formed on fully hydrated sorbents that is not stabilized by the deprotonation of another amine group but rather by the protonation of available hydrogen bridging silanol groups and adsorbed H_2O of the hydrated support (Scheme 4.4).

Scheme 4.4: Schematic description of fully-hydrated amine impregnated SBA-15.

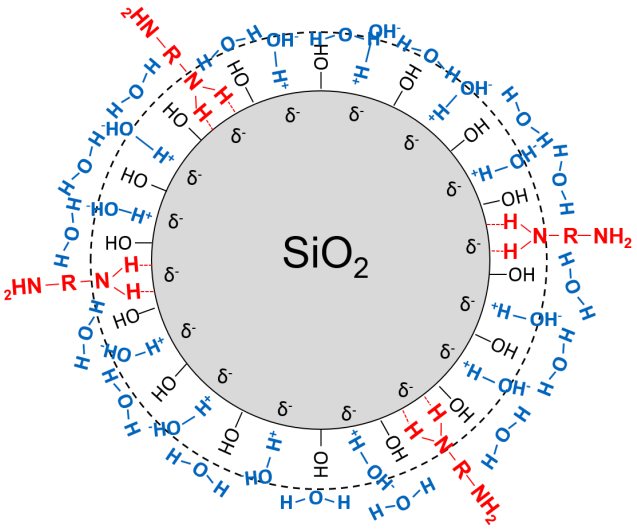

4.3.3 Kinetics of Water-Free and Fully-Hydrated Adsorbents.

Breakthrough curves of TEPA 23 were recorded using a gas mixture of 10 vol.% CO_2 in N_2 at ambient pressure and 50 °C. In order to obtain insight of the influence of H_2O on the adsorption kinetics 5, 10 or 12 vol.% of H_2O vapor were added to the mixture while keeping the CO_2 concentration constant. The breakthrough curves of TEPA 23 are displayed below.

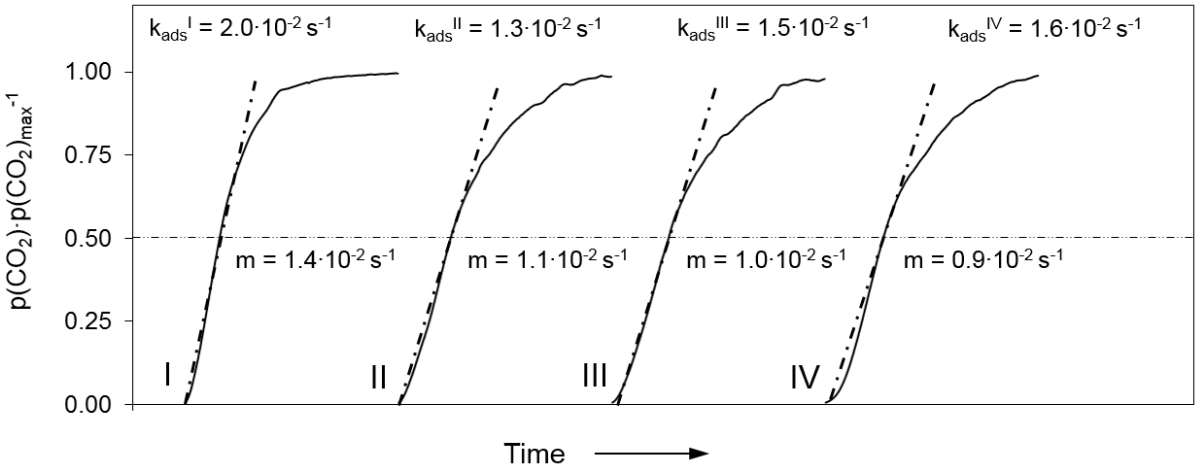

Figure 4.6: Breakthrough curves of TEPA 23 (I) without H_2O present and with (II) 5 vol.%, (III) 10 vol.% and (IV) 13 vol.% gaseous H_2O.

The slope (m) at 50 % uptake of each breakthrough curves was used to calculate the rate constant of adsorption (k_{ads}) as shown in Figure 4.6. The rate constant of non hydrated TEPA 23 agrees well with the calculated rate constants reported by Bollini et al. (0.012-0.02 s^{-1}) for water free adsorption of CO_2 on SBA-15 grafted with 3-aminopropylsilane. [133] The slope of the breakthrough curve constantly decreased for increasing gaseous water contents (Figure 4.6). Water adsorbing on the surface and in the pores of the adsorbent leads to an additional barrier between the gas phase and the bulk, because the solubility of CO_2 in H_2O is limited and, hence the adsorption is retarded. However, k_{ads} only decreased significantly for the lowest H_2O content and rose up to 80 % of the value for the rate constant of the non hydrated sorbent. This complex change is tentatively explained by variations in the adsorption mechanism from carbamates to bicarbonates and Si-OH stabilized carbamates that require only one amine group to adsorb one CO_2 molecule. The increase in amine efficiency led to an enhanced CO_2 uptake capacity that resulted in longer breakthrough times (t_{front}) and in turn higher rate constants (Equation 4.4). Thus, the diffusion coefficient was only calculated for non hydrated TEPA 23, because changes in the adsorption mechanism influence the calculated rate constant k_{adsII}, k_{adsIII}, k_{adsIV}, leading only to apparent values. The effective diffusion coefficient $D_{eff}(CO_2)$ was calculated to be $8.7{\cdot}10^{-11}\,m^2\,s^{-1}$, which is in good agreement with the value of $D_c(CO_2)$ of $1.66{\cdot}10^{-12}\,m^2\,s^{-1}$ obtained by the analysis of the time resolved IR spectra. By calcu-

lating the Thiele modulus ϕ, it can be further assessed whether the regime is kinetically controlled ($\phi < 0.3$) or limited by pore diffusion ($\phi > 3.0$).[136] First order kinetics are presumed for CO_2 adsorption via formation of carbamates with primary and secondary amines (Equation 4.1).[129]

$$\phi = \frac{V_{particle}}{A_{particle}} \sqrt{\frac{k_{ads}}{D_{eff}(CO_2)}} \tag{4.1}$$

The obtained value for the Thiele modulus of 0.45 is in the transition regime between microkinetics and limitation by pore diffusion. For a spherical particle the effectiveness factor η is defined as a function of the Thiele modulus as shown in Equation 4.2.[136] The effectiveness factor was calculated to be 0.99 and therefore effects of pore diffusion limitation of TEPA impregnated SBA-15 with amine loadings of 23 wt.% and lower can be excluded.

$$\eta = \frac{3}{\phi} \left(\frac{1}{tanh(\phi)} - \frac{1}{\phi} \right) \tag{4.2}$$

The CO_2 uptakes for different H_2O contents in the CO_2 N_2 gas mixture are illustrated in Figure 4.7. The uptakes before breakthrough and the total CO_2 uptakes both increased for higher H_2O pressures, mainly caused by a change in the adsorption mechanism. However, the question arises whether the increase in uptake could be also associated with the absorption of CO_2 in the adsorbed water layer.

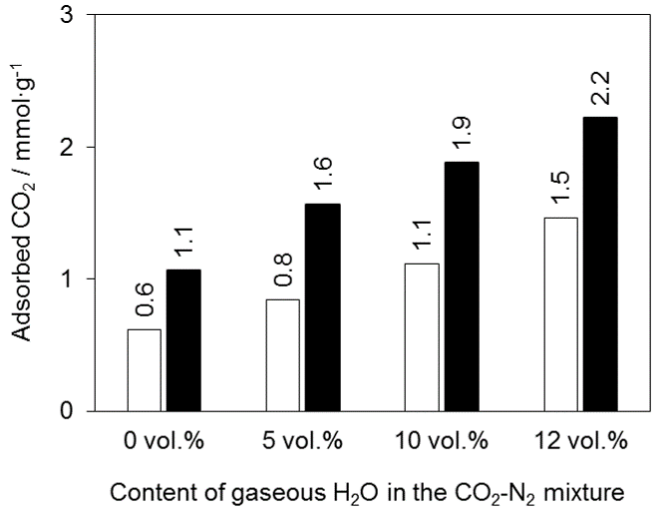

Figure 4.7: CO_2 uptakes before breakthrough (unfilled bars) and total uptakes (filled bars) of TEPA 23 at different contents of H_2O vapor in the CO_2-N_2 mixture at 50 °C.

Therefore, the influence of adsorbed H_2O on the capacity of TEPA 23 was investigated as displayed in Table 4.5. A significant influence of transport resistance in the liquid film and thus a decrease in the interaction between the bicarbonate and the active amine sites has only been reported for water vapor concentrations as high as 20 vol.%.[137] A water film covering the total surface of the adsorbent particle is achieved for gaseous water contents of 10 vol.% and higher. The CO_2 uptake of the adsorbed water is by a factor 1000 lower compared to the adsorption capacity of the non hydrated samples determined by CO_2 adsorption isotherms. Therefore, the CO_2 uptake of the adsorbed water layer can be neglected and a change in the adsorption mechanism is the main driving force for increased uptake capacities.

Table 4.5: Physical properties of TEPA 23 after exposure to H_2O vapor for 12 h.

	H_2O uptake / μL	Thickness of H_2O film / μm	CO_2 uptake of H_2O / μmol
5 vol% H_2O	84	0.0	0.0
10 vol% H_2O	224	1.3	0.15
12 vol% H_2O	270	2.0	0.24

The desorption properties at 50 °C or 100 °C in N_2 flow are displayed in Figure 4.8. The CO_2 uptake on TEPA 23 was fully reversible at 100 °C independent of the H_2O vapor content. The amount of CO_2 that was desorbed by concentration swing at 50 °C increased from 38 % (0 vol.% H_2O) to 58 % (0 vol.% H_2O) with increasing water content.

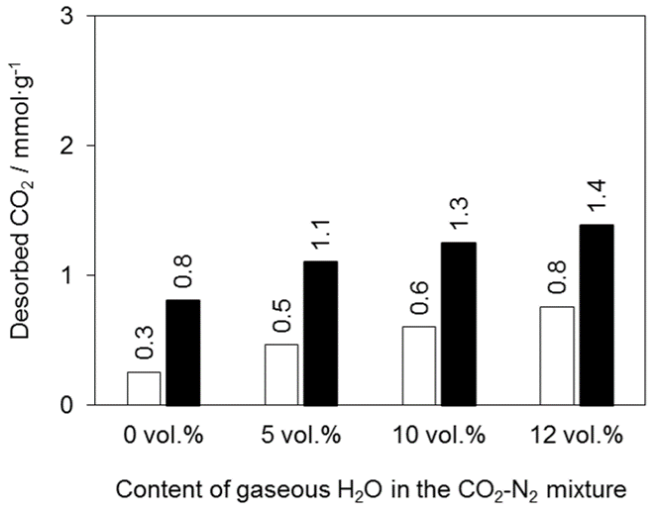

Figure 4.8: Desorption by concentration swing at 50 °C (unfilled bars) and temperature swing (100 °C, filled bars) of TEPA 23 at different contents of H_2O vapor in the CO_2-N_2 mixture.

We hypothesize that the oversaturated water layer, present during the concentration swing, will not favor re-adsorption of CO_2 due to the concentration gradient between the gas phase and the water phase. Thus, we conclude that the presence of H_2O vapor increases the efficiency of the adsorption as well as the desorption step.

4.4 Conclusion

The present investigation demonstrates that not only the nature of the amine group (primary, secondary or tertiary) has to be considered in the synthesis of amine-loaded solid CO_2 sorbents, but also the size of the amine molecule will influence the activity for the adsorption of CO_2. Highly ordered mesoporous metal oxides like SBA-15 contain pores with a diameter that exclude large and bulky amines like PEI from entering, whereas smaller molecules such as DETA can be stabilized. When the linear chain length of amines exhibits approximately 25 % of the pore diameter (e.g. TEPA), amines are seen to accumulate on the pore walls and cause a blockage. Although the decrease in CO_2 adsorption capacity was significant, pore diffusion limitations for the adsorption of CO_2 were hardly observed. The water free adsorption of CO_2 proceeds predominately via formation of carbamates, with a maximum amine efficiency of 50 %. The presence of H_2O changes the adsorption mechanism and also enables bicarbonates and carbamates to be stabilized by the hydrated support. The initial decrease in adsorption kinetics for low H_2O vapor contents in the gas stream is attributed to the limited solubility of CO_2 in the adsorbed H_2O film. Nevertheless, the rate constants increase for higher amounts of adsorbed H_2O caused by changes in the mechanism resulting in enhanced uptake capacities for increasing H_2O content. The adsorption was fully reversible at 100 °C in N_2 independent of the amount of H_2O vapor in the gas mixture. Desorption of CO_2 was facilitated for hydrated adsorbents even at lower temperatures due to suppressed re-adsorption by the H_2O film. Overall, the present contribution shows that highly efficient capture materials can be prepared with high amine loadings when the chain length of the amines does not exceed the accessible pore diameter of the support. The content of H_2O vapor in industrial flue gas streams does not impair the performance of the amine impregnated adsorbents because the moderate decrease in uptake rates is compensated by an increase in uptake capacity.

4.5 Experimental Section

4.5.1 Synthesis

SBA-15 was synthesized according to literature.[55,82] 6 g of hydrochloric acid (Sigma Aldrich, 37 wt. %) were added to 188.5 g of DI water and 10.25 g of the surfactant P123 (BASF, Mw of 5750 g mol^{-1}) under rigid stirring. The solution was stirred for 1 day at 35 °C until a homogenous phase was obtained. Tetraethylorthosilicate (TEOS, Sigma Aldrich, $\geq$ 99.0 %) was added to the solution and the mixture was kept stirring at 35 °C for additional 24 h. The polymerized solution was aged in autoclaves at 80 °C for 24 h. The solution was filtered with deionized (DI) water for 3 times and the precipitate was dried at 60 °C for 5 h prior to calcination in synthetic air (8 h at 600 °C, heating rate: 2.5 °C min^{-1}, total flow rate: 100 mL min^{-1}). Diethylenetriamine (DETA), tetraethylenepentamine (TEPA) and polyethyleneimine (PEI) (Sigma Aldrich, purity $\geq$ 99.0 %, M_w of 800 g mol^{-1}) were immobilized on SBA-15 by wet impregnation with methanol (Sigma Aldrich, purity $\geq$ 99.8 %). All chemicals were used without further purification. The desired amounts of DETA, TEPA or PEI were dissolved in methanol under N_2 atmosphere with a ratio of amine to methanol of 1:50. SBA-15 was added to the solution under vigorous stirring. After 2 h at room temperature, the solvent was removed by vacuum evaporation at 40 °C to a minimum pressure of 350 mbar. The pressure was reduced stepwise (10 mbar) below 450 mbar to avoid evaporation of the amines. The recovered powders were pulverized and stored in opaque vials under Ar atmosphere to prevent degradation of amine-functionalized sorbents.

4.5.2 Characterization

The C, H and N content of SBA-15 impregnated with MEA, DEA, DETA, TEPA and PEI were determined by a EURO EA elemental analyzer. 1 - 2 mg of each sample were weight in a tin beaker for each sample. The samples are burned at 1000 °C in a stream of He. After the reduction of NOx compounds the gas stream was separated with a GC column. The products (CO_2, NO_2, H_2O) were analyzed with a thermal conductivity detector.

Surface areas, pore volumes and pore size distributions were determined by N_2 physisorption at 196 °C using a Quadrasorb SI automated surface area and pore size analyzer. Prior to analysis, the samples were evacuated at 100 °C and 10^{-2} mbar for 2 h by a Quantachrome FloVac Degasser. The surface areas were calculated with the Brunauer-Emmett-Teller (BET) model.[83] Pore volumes and pore sizes were estimated using the Barrett-Joyner-Halenda (BJH) model.[85]

IR spectra with a resolution of 4 cm^{-1} of impregnated samples were taken on a Bruker Vertex 70 spectrometer using a MCT detector. The samples were prepared as self-supporting wafers (approximately 10 mg cm^{-1}) and placed in a vacuum IR cell equipped with CaF_2 windows. Before starting the measurement, each wafer was activated at 100 °C for 1 h un-

der vacuum ($p = 10^{-6}$ mbar). CO_2 was adsorbed on the wafers at partial pressures between 0.05 and 10 mbar at 40 °C. The spectra were taken every 120 s (128 scans each), baseline corrected and normalized to the integrated intensity of Si O overtones (2095 - 1755 cm^{-1}). Diffusion coefficients $D_c(CO_2)$ for adsorbents were calculated by Fick's law applying the short time solution by Kärger and Ruthven for slab-shaped particles (Equation 4.3). [138]

$$\frac{m_t}{m_\infty} = \frac{2}{\sqrt{\pi}}\sqrt{\frac{D_c(CO_2)\cdot t}{l_c^2}} \tag{4.3}$$

According to Equation 4.3, the ratio of the absorbance m_t/m_∞ versus the square root of the time leads to a linear slope that yields the diffusion coefficient $D_c(CO_2)$. All species which exhibit absorbtion bands between 1700 - 1400 cm^{-1} were considered for the calculations. The characteristic length l_c is defined as the half-thickness of the slab that was half the average particle size (180 μm/2) of the sorbent. The thickness of the self-supporting wafer was between the diameter of one to two particles. Thus, the influence of external transport limitation was excluded.

^{13}C CP-MAS solid state NMR was performed on a Bruker Avance 300 MHz spectrometer at a resonance frequency of 75.486 MHz. The spectra were recorded from dry and fully-hydrated adsorbents that were purged with $^{13}CO_2$ overnight ex-situ prior to the measurement. The samples were packed into 4 mm zirconia rotors and spun at 12 kHz. For each spectrum a minimum of 32 000 scans was accumulated. Adamantane was used as a reference compound ($\delta = 1.76$ ppm).

4.5.3 Adsorption of CO_2 and H_2O

CO_2 adsorption isotherms were measured in vacuum up to 100 mbar CO_2 partial pressure at 35 °C and 70 °C on a Porotec Sorptomatic 1990 series chemisorption station. Before each measurement, the samples were heated at 80 °C under vacuum in order to remove residual H_2O. Heats of adsorption were measured by differential scanning calorimetry (DSC) on a Setaram Sensys Evo thermo gravimetric analyzer (TGA). CO_2 was adsorbed out of a mixture of 10 vol.% CO_2 in N_2 (total flow 16 mL min^{-1}) on approximately 20 mg sorbent. Prior to adsorption, all samples were dried in N_2 (16 mL min^{-1}) at 100 °C for 2 h. Breakthrough curves were obtained in a tubular reactor (8 mm diameter) operated at 50 °C and a total flow of 100 mL min^{-1}. The gas mixture for the adsorption step contained 89 vol.% N_2, 10 vol.% CO_2 and 1 vol.% Ar tracer. Additionally, 5, 10 or 12 vol.% H_2O vapor was mixed into the adsorption gas stream, decreasing the fraction of N_2 accordingly. When H_2O was added to the adsorption gas stream, the sorbents were pre-treated with the same H_2O partial pressure in N_2 at 50 °C for 12 h. The concentrations of all components were determined with a Pfeiffer OmniStar GSD 320 mass spectrometer (MS). The gas hourly space velocity (GHSV) and weight hourly space velocity (WHSV) in the reactor were

240 h^{-1} and 2.4 $g(CO_2) \cdot g(Ads)^{-1}h^{-1}$, respectively. The catalyst bed comprised 0.5 g of the adsorbent (100 μm < dp < 255 μm) mixed with 4 g of SiC (255 μm < dp < 425 μm). After reaching equilibrium conditions, the adsorbent was regenerated by setting the flow to 100 mL min^{-1} of N_2 while the temperature remained constant at 50 °C (concentration swing desorption). Full regeneration of the adsorbent was achieved by increasing the temperature to 100 °C with a heating rate of 10 °C min^{-1} (temperature swing desorption). The kinetic parameters for the adsorption of CO_2 with different amounts of H_2O present were determined by the correlation of Kast shown in Equation 4.4. [139]

$$\frac{d\left[\frac{p(CO_2)}{p(CO_2)_{max}}\right]}{dt} = \sqrt{\frac{k_{ads}}{t_{front}}} \tag{4.4}$$

The equation was deducted based on the assumption of a steep and linear adsorption isotherm that is an adequate approximation for chemisorption at low partial pressures. The equation is valid for the point when 50 % of the maximum equilibrium partial pressure ($p(CO_2)_{max}$) of the reactant gas is reached ($p(CO_2)$ = 50 mbar). The residence time of the adsorption front t_{front} is estimated by the breakthrough time of the adsorbent bed. The rate constant of adsorption k_{ads} yields the efficient diffusion coefficient $D_{eff}(CO_2)$ in dependence of the particle diameter dp (180 μm) as given below in Equation 3. [139]

$$k_{ads} = \frac{15 D_{eff}(CO_2)}{\pi d_p^2} \tag{4.5}$$

The thickness of the adsorbed film of H_2O (β) on the adsorbent particles was calculated by the water uptake of the particle V_{film} (determined by MS), the pore volume of the adsorbent V_{pore} and the average particle diameter d_p of 80 μm. The film thickness β is defined as the radius of the film (r_{film}) minus the radius of the particle (r_p).

$$V_{film} = \frac{4}{3}\pi \left[r_{film}^3 - \left(\frac{d_p}{2}\right)^3 \right] = \frac{V_{H_2O,ads} - V_{pore}}{n_{particle}} \tag{4.6}$$

$$r_{film} = \sqrt[3]{\frac{3}{4\pi}\frac{V_{H_2O,ads} - V_{pore}}{n_{particle}} + r_p^3} \tag{4.7}$$

The number of particles ($n_{particle}$) is defined by the ratio of total adsorbent particle volume ($V_{ads,total}$) to the volume of one adsorbent particle ($V_{particle}$) as shown by the following

equation.

$$n_{particle} = \frac{V_{ads,total}}{V_{particle}} = \frac{\frac{m_{ads}}{\rho_{ads}}}{\frac{4}{3} r_p^3 \pi} \tag{4.8}$$

This leads to the final expression for the film thickness below.

$$\beta = \left\{ \sqrt[3]{\left[\frac{\rho_{ads}}{m_{ads}} \left(V_{\mathrm{H_2O}} - V_{pore} \right) + 1 \right]} - 1 \right\} \cdot r_p \tag{4.9}$$

The solubility of CO_2 in the water film x(CO_2) was calculated by Henry's law for a CO_2 partial pressure y(CO_2) of 100 mbar (Equation 4.10). The Henry coefficient of 2795 bar was used for the absorption of CO_2 into H_2O $k_H(CO_2, H_2O)$ at 50 °C. [140]

$$x\left(\mathrm{CO_2}\right) = \frac{y\left(\mathrm{CO_2}\right)}{k_H(\mathrm{CO_2}, \mathrm{H_2O})} \tag{4.10}$$

4.6 Associated Content

Additional Information

Pore size distributions, IR spectra and the according peak assignment are listed in the Appendix A.3.

Peer-Reviewed Publication

This chapter is based on the following article: Maximilian W. Hahn, Matthias Steib, Andreas Jentys and Johannes Lercher, Mechanism and Kinetics of CO_2 Adsorption on Surface Bonded Amines, in press, *J. Phys. Chem. C.*, **2015**.

Clearance by the Publisher

Notes and Author Contributions

The outstanding performance of Matthias Steib during his Master's thesis was acknowledged with Co-Authorship of the article.

Oral Presentations

M.W. Hahn, E. Ball , A. Jentys, J.A. Lercher, Role of residual H_2O on the adsorption mechanism and kinetics of solid amine-functionalized sorbents for CO_2 capture, presented at the 249^{th} *ACS National Meeting* **3/2015**. Denver, CO, USA.

M.W. Hahn, M. Steib, A. Jentys, J.A. Lercher, Mechanism and kinetics of CO_2 adsorption on surface bonded amines, presented at the 27^{th} *Deutsche Zeolithtagung* **2/2015**. Oldenburg, Germany

M.W. Hahn, M. Steib, A. Jentys, J.A. Lercher, Adsorptive removal of CO_2 from simulated flue gas streams by functionalized novel solid sorbents, presented at the *MuniCat Scientific Update* **5/2013**. Munich, Germany

Poster Presentations

M.W. Hahn, M. Steib, A. Jentys, J.A. Lercher, Mechanism and interactions of amines impregnated on SBA-15 during CO_2 separation, presented at the 47^{th} *Jahrestreffen deutscher Katalytiker* **3/2014**. Weimar, Germany.

M.W. Hahn, M. Steib, A. Jentys, J.A. Lercher, A Mechanistic study of amine impregnated sorbents for post-combustion applications, presented at the 26^{th} *Deutsche Zeolithtagung* **2/2014**. Paderborn, Germany

5 Summary and Conclusion

Summary and Conclusion

The potential of solid sorbents for atmospheric and high-pressure CO_2 capture has been systematically investigated and discussed in Chapter 2 to 4. The synthesis, characterization, and experimental validation of hierarchically structured, millimeter-sized SiO_2 spheres for high-pressure CO_2 adsorption has been explored in Chapter 2. The new sorbents exhibited lower heats of adsorption compared to the benchmark zeolite 13X making them more applicable for temperature swing adsorption applications. The less intense CO_2 adsorption at lower partial pressures compared to zeolite 13X lead also to an increased CO_2 uptake capacity in pressure swing adsorption processes. Addition of Zr^{4+}cations to SiO_2 even further increased the CO_2 uptake of the SiO_2 spheres by generating Lewis acid-base sites.

The adsorption of CO_2 at atmospheric pressures was investigated in Chapter 3 on millimeter scale SiO_2 spheres that possess primary, secondary and bifunctional aminosilanes immobilized on a silanol surface. The concept of amine functionalized, hierarchically structured adsorbents for CO_2 capture facilitates the full recovery of the adsorption capacity already at 75 °C and thereby the thermal degradation of the adsorbents could be prevented. The water free CO_2 adsorption mechanism of aminosilanes, immobilized on silanol surfaces, is dependent on the functionality of the amine as well as on the interaction between the amine groups with a sufficient access to Si-OH groups. Overall, the limited access to surface silanol groups at higher amine densities constrains the formation of carbamates on primary amines and therefore secondary amines are more suitable when high CO_2 uptake capacities are required.

The impact of H_2O on the mechanism and kinetics of CO_2 adsorption by amine-impregnated SBA-15 has been addressed in Chapter 4. Highly efficient capture materials can be prepared with high amine loadings when the chain length of the amines does not exceed 25 % of the accessible pore diameter of the support. Bicarbonates and surface stabilized carbamates were formed on hydrated sorbents. Gaseous water decreased the adsorption rate but increased the maximum equilibrium uptake. The higher uptake of CO_2 in the presence of H_2O vapor is a result of a change in the adsorption mechanism that increases the amine efficiency, thus leading to a higher adsorption capacity. The adsorption was fully reversible for all adsorbents at a maximum desorption temperature of 100 °C.

In summary, high pressure capture processes like pre-combustion or oxyfuel require

highly porous sorbents with low binding energies for CO_2 in the regime of physisorption to allow efficient pressure and temperature swing applications (Chapter 2). In contrast, strong binding of CO_2 via chemisorption is eminent for atmospheric post-combustion capture (Chapter 3). Furthermore, the main by-product of a coal-fired power plant H_2O does not impair the performance of the amine impregnated adsorbents because the moderate decrease in uptake rates is compensated by an increase in uptake capacity. (Chapter 4). In conclusion, solid sorbents are promissing candidates for large-scale CO_2 capture and an alternative to applied aqueous amine wash processes.

Zusammenfassung und Schlussfolgerung

Das Potential fester Adsorbentien zur Abtrennung von CO_2 bei atmosphärischen Druck und Hochdruck war Hauptgegenstand der hier präsentierten Forschung. Die Synthese, Charakterisierung und das Verhalten unter experimentellen Bedingungen hierarchisch-strukturierter, millimetergroßer SiO_2 Kugeln für die Hochdruck CO_2 Abtrennung wurde in Kapitel 2 näher untersucht. Die neuartigen Sorbentien besitzen niedrigere Adsorptionwärmen im Vergleich zu dem Referenzmaterial Zeolith 13X. Dadurch eignen sich diese Materialien besser für Prozesse mit thermischer Regenerierung. Zudem führt die geringere CO_2 Aufnahme bei niedrigeren Partialdrücken ebenso zu einer verbesserten Regenerierbarkeit bei Anwendungen von zyklischen Druckänderungen. Das Einbringen von Zr^{4+}-Kationen in die SiO_2 Matrix erhöhte zudem die Abtrennleistung der SiO_2 Kugeln durch Entstehen Lewis-saurer Zentren.

Die CO_2 Adsorption auf millimetergroßen, mit primären und sekundären Aminen funktionaliserten SiO_2 Kugeln bei atmosphärischen Drücken war zentraler Schwerpunkt der Arbeiten in Kapitel 3. Amin-funktionaliserte hierarchische Adsorbentien ermöglichen vollständige Desorption von CO_2 bei einer Temperatur von nur 75 °C, wodurch thermische Degeneration unterdrückt wird. Der CO_2 Adsorptionsmechanismus der verankerten Aminosilane ist von der Aminfunktionalität, der Wechselwirkung zwischen den Aminen sowie ausreichender Interaktion zu Si-OH Gruppen abhängig. Der eingeschränkte Zugang zu oberflächennahen Silanolgruppen bei höheren Aminbeladungen behindert die Bildung von Carbamaten auf primären Aminen. Hierdurch stellen sekundäre Amine einen klaren Vorteil dar, wenn hohe CO_2 Aufnahmen angestrebt werden.

Der Einfluss von H_2O auf den Mechanismus und die Kinetik der CO_2 Adsorption mittels Amin imprägniertem SBA-15 wurde in Kapitel 4 behandelt. Hocheffiziente Adsorbentien mit hohen Aminbeladungen können synthetisert werden, wenn die Kettenlänge der Amine ein Viertel des Porendurchmesser des Trägers nicht überschreitet. Hydrogencarbonate und oberflächenstabilisierte Carbamate sind die bevorzugt aufzufindende adsorbierte Spezien, wenn H_2O im Abgas vorhanden ist. H_2O in der Gasphase verringerte die Adsorptionsrate bei gleichzeitiger Zunahme der Gleichgewichtsbeladung. Die erhöhte Aufnahme von CO_2 in der Gegenwart von H_2O resultiert aus einem Wechsel des Adsorptionsmechanismus. Dies hat eine Erhöhung der Amineffizienz zur Folge, wodurch die Aufnahmekapzität für CO_2 erhöht wird. Für Temperaturen von 100 °C war die Adsorption für alle untersuchten Sorbentien vollständig reversibel.

Zusammenfassend lässt sich sagen, dass Hochdruck Adsorptionsprozesse wie Pre-Combustion oder Oxyfuel hoch poröse Adsorbentien mit geringeren Bindungsenergien von CO_2 benötigen. Die Physisorption ermöglicht effiziente Regeneration durch Temperatur- und Druckänderung und damit reversible Adsorptionsprozesse. Im Gegensatz dazu sind hohe Bindungsenergien (Chemisorption) bei Post-Combustion Prozessen erforderlich (Kapitel 3). Des Weiteren führt H_2O als Hauptnebenprodukt der Verbrennung nicht zu einer signifikanten Verschlechterung der Abtrennleistung von CO_2 mittels Amin-funktionalisierten

Adsorbentien. Der moderate Abfall in der Adsorptionskinetik wird durch eine erhöhte Aufnahme durch Wechsel des Adsorptionsmechanismus kompensiert (Kapitel 4). Abschliessend hat sich das Konzept fester Sorbentien zur CO_2 Abtrennung als vielversprechende Alternative zu den derzeit angewandten flüssigen Absorptionsprozessen bewährt.

Chances for CO_2 Capture in the Future

These days, no economic and large-scale coal-fired power plant equipped with a carbon capture unit is in operation. So the question arises, whether we will require CO_2 capture from large point source emitters in the future or, if CO_2 capture from ambient air is a more applicable process?

Current developments in enhanced oil recovery and the lowering demand for gasoline in the economic countries will strongly shift the importance of oil in the energy sector. The increasing oil production by the United States of America was not counterbalanced by a reduction in oil production by the countries belonging to the Organization of the Petroleum Exporting Countries (OPEC). As a consequence, the oil price dropped by 40 % in six months, between June 2014 and November 2014, down to a critical price below 60 dollar per barrel at which the profitability of enhanced oil recovery technologies is at a tipping point. [141,142]

Prices of CO_2 certificates are strongly regulated for European's industry. [143,144] However, a bill for CO_2 certificates for private car owners is already under preparation and will strongly exceed the costs per gram of CO_2 compared to industrial prices. [145,146] A directly related rise of electro mobility and fuel cell driven cars is also a chance to create new market potentials for established technologies: A total shift from fossil fuels resources to fully-renewable energy resources will have to pass a transition state. Currently, the price of H_2 produced by electrolysis by far exceeds the price of H_2 produced from steam reforming that requires vast amounts of natural gas that is cheaply accessible from EOR. [147,148] The decentralized supply from renewable energy resources like wind and solar energy results in a storage dilemma of green electricity and significantly limits the development of new energy technologies. [149,150] A shift in the transportation sector from combustion engines to electro mobility will provide a huge decentralized storage capacity that cannot fully be covered by the amount of renewable energy sources installed, yet. [151] Conventional energies like electricity, most notably from coal-fired power plants, will be crucial to cover that gap. Also the production of H_2 from natural gas leads to vast amounts of CO_2 that have to be separated out of the process. [148]

The dominant role of the combustion engine in the transportation sector, will rather be curbed by a limited profit margin than thermodynamic limitations of the engine itself. As a direct consequence, the strong decrease of decentralized CO_2 emissions will not require excessive CO_2 capture from ambient air and the focus is rather to be shifted to CO_2 capture from large point source emitters.

References

[1] D. J. Hofmann, J. H. Butler, P. P. Tans. *Atmospheric Environment*, 43, **2009**, 2084–2086.

[2] F Manzano-Agugliaro, A Alcayde, F. Montoya, A Zapata-Sierra, C Gil. *Renewable and Sustainable Energy Reviews*, 18, **2013**, 134–143.

[3] H. Liming. *Renewable and Sustainable Energy Reviews*, 13, **2009**, 1096–1103.

[4] A. J. Ragauskas, C. K. Williams, B. H. Davison, G. Britovsek, J. Cairney, C. A. Eckert, W. J. Frederick, J. P. Hallett, D. J. Leak, C. L. Liotta, et al. *Science*, 311, **2006**, 484–489.

[5] D. Carpenter, T. L. Westover, S. Czernik, W. Jablonski. *Green Chemistry*, 16, **2014**, 384–406.

[6] S. Zinoviev, F. Müller-Langer, P. Das, N. Bertero, P. Fornasiero, M. Kaltschmitt, G. Centi, S. Miertus. *ChemSusChem*, 3, **2010**, 1106–1133.

[7] G. Centi, S. Perathoner. *ChemSusChem*, 3, **2010**, 195–208.

[8] F. Leurent, E. Windisch. *European Transport Research Review*, 3, **2011**, 221–235.

[9] X. Rui, Q. Yan, M. Skyllas-Kazacos, T. M. Lim. *Journal of Power Sources*, 258, **2014**, 19–38.

[10] A. Morozan, B. Jousselme, S. Palacin. *Energy & Environmental Science*, 4, **2011**, 1238–1254.

[11] T. Abbasi, S. Abbasi. *Renewable and Sustainable Energy Reviews*, 15, **2011**, 3034–3040.

[12] K. Binnemans, P. T. Jones, B. Blanpain, T. Van Gerven, Y. Yang, A. Walton, M. Buchert. *Journal of Cleaner Production*, 51, **2013**, 1–22.

[13] B. Jiang, Z. Sun, M. Liu. *Energy*, 35, **2010**, 4257–4264.

[14] P. Pongsoi, S. Wongwises. *Renewable and Sustainable Energy Reviews*, 24, **2013**, 586–592.

[15] J. Li, X. Zhuang, X. Querol, O. Font, N. Moreno, J. Zhou. *Fuel*, 95, **2012**, 446–456.

[16] J. D. Hughes. *Nature*, 494, **2013**, 307–308.

[17] G. Whiteman, C. Hope, P. Wadhams. *Nature*, 499, **2013**, 401–403.

[18] D. Singh, E. Croiset, P. L. Douglas, M. A. Douglas. *Energy Conversion and Management*, 44, **2003**, 3073–3091.

[19] N. Dave, T. Do, D. Palfreyman, P. Feron. *Energy Procedia*, 4, **2011**, 2005–2019.

[20] N. MacDowell, N. Florin, A. Buchard, J. Hallett, A. Galindo, G. Jackson, C. S. Adjiman, C. K. Williams, N. Shah, P. Fennell. *Energy & Environmental Science*, 3, **2010**, 1645–1669.

[21] C. Pauley, S Haigh, P. Simiskey. *Oil Gas Journal;(United States)*, 82, **1984**.

[22] M. R. Abu-Zahra, Z. Abbas, P. Singh, P. Feron. **2013**.

[23] H. Herzog. *Energy Laboratory Working Paper*, **1999**.

[24] J. Oexmann, A. Kather. *Energy Procedia*, 1, **2009**, 799–806.

[25] M. Zhao, A. I. Minett, A. T. Harris. *Energy & Environmental Science*, 6, **2013**, 25–40.

[26] G. T. Rochelle et al. *Science*, 325, **2009**, 1652–1654.

[27] W. Wagner, A. Pruß. *Journal of Physical and Chemical Reference Data*, 31, **2002**, 387–535.

[28] T. Tsuji. *Thermodynamic Properties of Solids*, **2010**, 159–196.

[29] A. Goeppert, M. Czaun, R. B. May, G. S. Prakash, G. A. Olah, S. Narayanan. *Journal of the American Chemical Society*, 133, **2011**, 20164–20167.

[30] A. Heydari-Gorji, Y. Yang, A. Sayari. *Energy & Fuels*, 25, **2011**, 4206–4210.

[31] A. Heydari-Gorji, A. Sayari. *Chemical Engineering Journal*, 173, **2011**, 72–79.

[32] A. Heydari-Gorji, Y. Belmabkhout, A. Sayari. *Langmuir*, 27, **2011**, 12411–12416.

[33] X. Wang, V. Schwartz, J. C. Clark, X. Ma, S. H. Overbury, X. Xu, C. Song. *The Journal of Physical Chemistry C*, 113, **2009**, 7260–7268.

[34] X. Ma, X. Wang, C. Song. *Journal of the American Chemical Society*, 131, **2009**, 5777–5783.

[35] S. Choi, M. L. Gray, C. W. Jones. *ChemSusChem*, 4, **2011**, 628–635.

[36] J. C. Hicks, J. H. Drese, D. J. Fauth, M. L. Gray, G. Qi, C. W. Jones. *Journal of the American Chemical Society*, 130, **2008**, 2902–2903.

[37] S. A. Didas, R. Zhu, N. A. Brunelli, D. S. Sholl, C. W. Jones. *The Journal of Physical Chemistry C*, **2014**.

[38] N. A. Brunelli, S. A. Didas, K. Venkatasubbaiah, C. W. Jones. *Journal of the American Chemical Society*, 134, **2012**, 13950–13953.

[39] M. Kanniche, R. Gros-Bonnivard, P. Jaud, J. Valle-Marcos, J.-M. Amann, C. Bouallou. *Applied Thermal Engineering*, 30, **2010**, 53–62.

[40] B. Buhre, L. Elliott, C. Sheng, R. Gupta, T. Wall. *Progress in Energy and Combustion Science*, 31, **2005**, 283–307.

[41] Q. Wang, J. Luo, Z. Zhong, A. Borgna. *Energy & Environmental Science*, 4, **2011**, 42–55.

[42] J. David, H. Herzog. In: *fifth international conference on greenhouse gas control technologies, Cairns, Australia*. **2000**, 13–16.

[43] C. M. Quintella, S. A. Hatimondi, A. P. S. Musse, S. F. Miyazaki, G. S. Cerqueira, A. d. A. Moreira. *Energy Procedia*, 4, **2011**, 2050–2057.

[44] P. Bollini, S. A. Didas, C. W. Jones. *Journal of Materials Chemistry*, 21, **2011**, 15100–15120.

[45] K. R. Thampi, J. Kiwi, M. Graetzel. *Nature*, 327, **1987**, 506–508.

[46] S. K. Hoekman, A. Broch, C. Robbins, R. Purcell. *International Journal of Greenhouse Gas Control*, 4, **2010**, 44–50.

[47] D. Hu, J. Gao, Y. Ping, L. Jia, P. Gunawan, Z. Zhong, G. Xu, F. Gu, F. Su. *Industrial & Engineering Chemistry Research*, 51, **2012**, 4875–4886.

[48] M. Blunt, F. J. Fayers, F. M. Orr Jr. *Energy Conversion and Management*, 34, **1993**, 1197–1204.

[49] T. Holt, E. Lindeberg. *Energy conversion and management*, 34, **1993**, 1189–1196.

[50] A. S. Fayed. *Oil Gas Journal;(United States)*, 81, **1983**.

[51] P. Nugent, Y. Belmabkhout, S. D. Burd, A. J. Cairns, R. Luebke, K. Forrest, T. Pham, S. Ma, B. Space, L. Wojtas, et al. *Nature*, 495, **2013**, 80–84.

[52] Z. R. Herm, J. A. Swisher, B. Smit, R. Krishna, J. R. Long. *Journal of the American Chemical Society*, 133, **2011**, 5664–5667.

[53] J. Schell, N. Casas, R. Blom, A. I. Spjelkavik, A. Andersen, J. H. Cavka, M. Mazzotti. *Adsorption*, 18, **2012**, 213–227.

[54] S. Cavenati, C. A. Grande, A. E. Rodrigues. *Journal of Chemical & Engineering Data*, 49, **2004**, 1095–1101.

[55] D. Zhao, J. Feng, Q. Huo, N. Melosh, G. H. Fredrickson, B. F. Chmelka, G. D. Stucky. *Science*, 279, **1998**, 548–552.

[56] C. Kresge, M. Leonowicz, W. Roth, J. Vartuli, J. Beck. *Nature*, 359, **1992**, 710–712.

[57] N. Stock, S. Biswas. *Chemical Reviews*, 112, **2011**, 933–969.

[58] J.-E. Park, H.-K. Youn, S.-T. Yang, W.-S. Ahn. *Catalysis Today*, 190, **2012**, 15–22.

[59] S Schacht, Q Huo, I. Voigt-Martin, G. Stucky, F Schüth. *Science*, 273, **1996**, 768–771.

[60] Q. Huo, J. Feng, F. Schüth, G. D. Stucky. *Chemistry of Materials*, 9, **1997**, 14–17.

[61] T. Förster, S. Scholz, Y. Zhu, J. A. Lercher. *Microporous and Mesoporous Materials*, 142, **2011**, 464–472.

[62] S. Scholz, S. R. Bare, S. D. Kelly, J. A. Lercher. *Microporous and Mesoporous Materials*, 146, **2011**, 18–27.

[63] S. Scholz, H. Shi, J. A. Lercher. *Topics in Catalysis*, 55, **2012**, 800–810.

[64] S. Scholz, J. A. Lercher. *Chemistry of Materials*, 23, **2011**, 2091–2099.

[65] C. Brinker. *Journal of Non-Crystalline Solids*, 100, **1988**, 31–50.

[66] H. Gesser, P. Goswami. *Chemical Reviews*, 89, **1989**, 765–788.

[67] R. Deshpande, D.-W. Hua, D. M. Smith, C. J. Brinker. *Journal of Non-Crystalline Solids*, 144, **1992**, 32–44.

[68] C. J. Brinker, G. W. Scherer. Gulf Professional Publishing, **1990**.

[69] D. D. Perrin, B. Dempsey, E. P. Serjeant. Vol. 1. Springer, **1981**.

[70] F. G. Bordwell. URL: `http://www.chem.wisc.edu/areas/reich/pkatable/` (visited on 03/10/2014).

[71] F. G. Bordwell. *Accounts of Chemical Research*, 21, **1988**, 456–463.

[72] F. K. Beilstein. Vol. 1. J. Springer, **1918**.

[73] H. Pfeiffer, P. Bosch, S. Bulbulian. *Materials Chemistry and Physics*, 78, **2003**, 558–561.

[74] G Busca, V Lorenzelli. *Materials Chemistry*, 7, **1982**, 89–126.

[75] M. Bensitel, V. Moraver, J. Lamotte, O. Saur, J.-C. Lavalley. *Spectrochimica Acta Part A: Molecular Spectroscopy*, 43, **1987**, 1487 –1491. ISSN: 0584-8539.

[76] K. Pokrovski, K. T. Jung, A. T. Bell. *Langmuir*, 17, **2001**, 4297–4303.

[77] Z Dang, B. Anderson, Y Amenomiya, B. Morrow. *The Journal of Physical Chemistry*, 99, **1995**, 14437–14443.

[78] K. T. Jung, A. T. Bell. *Journal of Catalysis*, 204, **2001**, 339–347.

[79] R. W. Stevens Jr, R. V. Siriwardane, J. Logan. *Energy & Fuels*, 22, **2008**, 3070–3079.

[80] P. Linga, R. Kumar, P. Englezos. *Journal of Hazardous Materials*, 149, **2007**, 625–629.

[81] D. Ko, R. Siriwardane, L. T. Biegler. *Industrial & Engineering Chemistry Research*, 42, **2003**, 339–348.

[82] D. Zhao, J. Sun, Q. Li, G. D. Stucky. *Chemistry of Materials*, 12, **2000**, 275–279.

[83] S. Brunauer, P. H. Emmett, E. Teller. *Journal of the American Chemical Society*, 60, **1938**, 309–319.

[84] M. Dubinin. *Progress in Surface and Membrane Science*, 9, **1975**, 1–70.

[85] E. P. Barrett, L. G. Joyner, P. P. Halenda. *Journal of the American Chemical society*, 73, **1951**, 373–380.

[86] X. Yan, L. Zhang, Y. Zhang, G. Yang, Z. Yan. *Industrial & Engineering Chemistry Research*, 50, **2011**, 3220–3226.

[87] Y. Kuwahara, D.-Y. Kang, J. R. Copeland, N. A. Brunelli, S. A. Didas, P. Bollini, C. Sievers, T. Kamegawa, H. Yamashita, C. W. Jones. *Journal of the American Chemical Society*, 134, **2012**, 10757–10760.

[88] D. Wang, X. Wang, X. Ma, E. Fillerup, C. Song. *Catalysis Today*, **2014**.

[89] A. Sayari, A. Heydari-Gorji, Y. Yang. *Journal of the American Chemical Society*, 134, **2012**, 13834–13842.

[90] P. Bollini, S. Choi, J. H. Drese, C. W. Jones. *Energy & Fuels*, 25, **2011**, 2416–2425.

[91] C. S. Srikanth, S. S. Chuang. *ChemSusChem*, 5, **2012**, 1435–1442.

[92] E. M. Hampe, D. M. Rudkevich. *Tetrahedron*, 59, **2003**, 9619–9625.

[93] W. A. Eger, A. Genest, B. Rieger, N. Rösch. *ChemSusChem*, 5, **2012**, 1967–1973.

[94] L. Phan, J. R. Andreatta, L. K. Horvey, C. F. Edie, A.-L. Luco, A. Mirchandani, D. J. Darensbourg, P. G. Jessop. *The Journal of Organic Chemistry*, 73, **2008**, 127–132.

[95] K. Masuda, Y. Ito, M. Horiguchi, H. Fujita. *Tetrahedron*, 61, **2005**, 213–229.

[96] Z. Dijkstra, A. Doornbos, H Weyten, J. Ernsting, C. Elsevier, J. Keurentjes. *The Journal of Supercritical Fluids*, 41, **2007**, 109–114.

[97] A.-H. Liu, R. Ma, C. Song, Z.-Z. Yang, A. Yu, Y. Cai, L.-N. He, Y.-N. Zhao, B. Yu, Q.-W. Song. *Angewandte Chemie International Edition*, 51, **2012**, 11306–11310.

[98] H. Y. Huang, R. T. Yang, D. Chinn, C. L. Munson. *Industrial & Engineering Chemistry Research*, 42, **2003**, 2427–2433.

[99] Y. Belmabkhout, R. Serna-Guerrero, A. Sayari. *Adsorption*, 17, **2011**, 395–401.

[100] Y. Belmabkhout, N. Heymans, G. De Weireld, A. Sayari. *Energy & Fuels*, 25, **2011**, 1310–1315.

[101] M. W. Hahn, M. Steib, A. Jentys, J. A. Lercher. *Journal of Materials Chemistry A*, 2, **2014**, 13624–13634.

[102] H. Hall Jr. *Journal of the American Chemical Society*, 79, **1957**, 5441–5444.

[103] F. Brotzel, Y. C. Chu, H. Mayr. *The Journal of Organic Chemistry*, 72, **2007**, 3679–3688.

[104] C. Knöfel, C. Martin, V. Hornebecq, P. L. Llewellyn. *The Journal of Physical Chemistry C*, 113, **2009**, 21726–21734.

[105] K. Tanaka, J. White. *The Journal of Physical Chemistry*, 86, **1982**, 4708–4714.

[106] J. Tanthana, S. S. Chuang. *ChemSusChem*, 3, **2010**, 957–964.

[107] J.-B. Bossa, F. Borget, F. Duvernay, P. Theulé, T. Chiavassa. *The Journal of Physical Chemistry A*, 112, **2008**, 5113–5120.

[108] J. Bossa, P Theule, F Duvernay, T Chiavassa. *The Astrophysical Journal*, 707, **2009**, 1524.

[109] N. Hiyoshi, K. Yogo, T. Yashima. *Microporous and Mesoporous Materials*, 84, **2005**, 357–365.

[110] A. Danon, P. C. Stair, E. Weitz. *The Journal of Physical Chemistry C*, 115, **2011**, 11540–11549.

[111] N. B. Colthup, L. H. Daly, S. E. Wiberley. Elsevier, **1990**.

[112] Z. Bacsik, N. Ahlsten, A. Ziadi, G. Zhao, A. E. Garcia-Bennett, B. Martín-Matute, N. Hedin. *Langmuir*, 27, **2011**, 11118–11128.

[113] E. P. Hunter, S. G. Lias. *Journal of Physical and Chemical Reference Data*, 27, **1998**, 413–656.

[114] M. A. Alkhabbaz, P. Bollini, G. S. Foo, C. Sievers, C. W. Jones. *Journal of the American Chemical Society*, 136, **2014**, 13170–13173.

[115] A. Sayari, Y. Belmabkhout. *Journal of the American Chemical Society*, 132, **2010**, 6312–6314.

[116] B. C. Lippens, J. De Boer. *Journal of Catalysis*, 4, **1965**, 319–323.

[117] V. Blum, R. Gehrke, F. Hanke, P. Havu, V. Havu, X. Ren, K. Reuter, M. Scheffler. *Computer Physics Communications*, 180, **2009**, 2175–2196.

[118] X. Ren, P. Rinke, V. Blum, J. Wieferink, A. Tkatchenko, A. Sanfilippo, K. Reuter, M. Scheffler. *New Journal of Physics*, 14, **2012**, 053020.

[119] A. D. Becke. *Physical Review A*, 38, **1988**, 3098.

[120] A. D. Becke. *The Journal of Chemical Physics*, 98, **1993**, 5648–5652.

[121] P. Stephens, F. Devlin, C. Chabalowski, M. J. Frisch. *The Journal of Physical Chemistry*, 98, **1994**, 11623–11627.

[122] A. Tkatchenko, M. Scheffler. *Physical Review Letters*, 102, **2009**, 073005.

[123] P. M. Schoenecker, C. G. Carson, H. Jasuja, C. J. Flemming, K. S. Walton. *Industrial & Engineering Chemistry Research*, 51, **2012**, 6513–6519.

[124] G. Li, P. Xiao, P. Webley, J. Zhang, R. Singh, M. Marshall. *Adsorption*, 14, **2008**, 415–422.

[125] Z. Liang, M. Marshall, A. L. Chaffee. *Energy & Fuels*, 23, **2009**, 2785–2789.

[126] R. M. Ravenelle, J. R. Copeland, W.-G. Kim, J. C. Crittenden, C. Sievers. *ACS Catalysis*, 1, **2011**, 552–561.

[127] M. W. Hahn, J. R. Copeland, A. H. Van Pelt, C. Sievers. *ChemSusChem*, 6, **2013**, 2304–2315.

[128] D. S. Mebane, J. D. Kress, C. B. Storlie, D. J. Fauth, M. L. Gray, K. Li. *The Journal of Physical Chemistry C*, 117, **2013**, 26617–26627.

[129] E. R. Monazam, L. J. Shadle, D. C. Miller, H. W. Pennline, D. J. Fauth, J. S. Hoffman, M. L. Gray. *AIChE Journal*, 59, **2013**, 923–935.

[130] X. Xu, C. Song, B. G. Miller, A. W. Scaroni. *Fuel Processing Technology*, 86, **2005**, 1457–1472.

[131] Z. H. Cheng, A. Yasukawa, K. Kandori, T. Ishikawa. *Langmuir*, 14, **1998**, 6681–6686.

[132] E. D. Snijder, M. J. te Riele, G. F. Versteeg, W. Van Swaaij. *Journal of Chemical and Engineering data*, 38, **1993**, 475–480.

[133] P. Bollini, N. A. Brunelli, S. A. Didas, C. W. Jones. *Industrial & Engineering Chemistry Research*, 51, **2012**, 15153–15162.

[134] S. A. Didas, A. R. Kulkarni, D. S. Sholl, C. W. Jones. *ChemSusChem*, 5, **2012**, 2058–2064.

[135] J.-Y. Park, S. J. Yoon, H. Lee. *Environmental Science & Technology*, 37, **2003**, 1670–1675.

[136] M. Baerns, A. Behr, A. Brehm, J. Gmehling, H. Hofmann, U. Onken, A. Renken, K.-O. Hinrichsen, R. Palkovits. Vol. 1. Wiley-VCH, **2013**.

[137] S. Cui, W. Cheng, X. Shen, M. Fan, A. T. Russell, Z. Wu, X. Yi. *Energy Environ. Sci.* 4, **2011**, 2070–2074.

[138] C. L. J. Cavalcante, D. M. Ruthven. *Industrial & Engineering Chemistry Research*, 34, **1995**, 185–191.

[139] A. Jess, P. Wasserscheid. John Wiley & Sons, **2013**.

[140] J. J. Carroll, J. D. Slupsky, A. E. Mather. *Journal of Physical and Chemical Reference Data*, 20, **1991**, 1201–1209.

[141] URL: `http://www.nasdaq.com` (visited on 12/14/2014).

[142] URL: `http://www.forbes.com` (visited on 12/18/2014).

[143] A. Weidlich, F. Sensfuß, M. Genoese, D. Veit. In: *Emissions Trading*. Springer, **2008**, 91–101.

[144] G. Oggioni, I. Rumiantseva, Y. Smeers. In: *Clean Electrical Power, 2007. ICCEP'07. International Conference on*. IEEE. **2007**, 291–298.

[145] M. Achtnicht. *Climatic change*, 113, **2012**, 679–697.

[146] J. Albrecht. *Journal of Cleaner Production*, 9, **2001**, 179–189.

[147] A. Haryanto, S. Fernando, N. Murali, S. Adhikari. *Energy & Fuels*, 19, **2005**, 2098–2106.

[148] P. L. Spath, M. K. Mann. National Renewable Energy Laboratory Golden, CO, **2000**.

[149] J. A. Turner. *Science*, 285, **1999**, 687–689.

[150] J. M. Carrasco, L. G. Franquelo, J. T. Bialasiewicz, E. Galván, R. P. Guisado, M. A. Prats, J. I. León, N. Moreno-Alfonso. *Industrial Electronics, IEEE Transactions on*, 53, **2006**, 1002–1016.

[151] R. Kemp, J. Rotmans. *System innovation and the transition to sustainability: theory, evidence and policy*, **2004**, 137–167.

[152] E Akalin, S Akyüz. *Journal of Molecular Structure*, 482, **1999**, 175–181.

[153] K Schwetlick. **2009**.

[154] G. Socrates. John Wiley & Sons, **2004**.

[155] J. Langer, B. Schrader, V. Bastian, E. Jacob. *Fresenius' Journal of Analytical Chemistry*, 352, **1995**, 489–495.

[156] G. Herzberg. Van Nostrand Reinhold, **1945**.

[157] R. Khanna, M. Moore. *Spectrochimica Acta Part A: Molecular and Biomolecular Spectroscopy*, 55, **1999**, 961–967.

A Appendix

A.1 Chapter 2

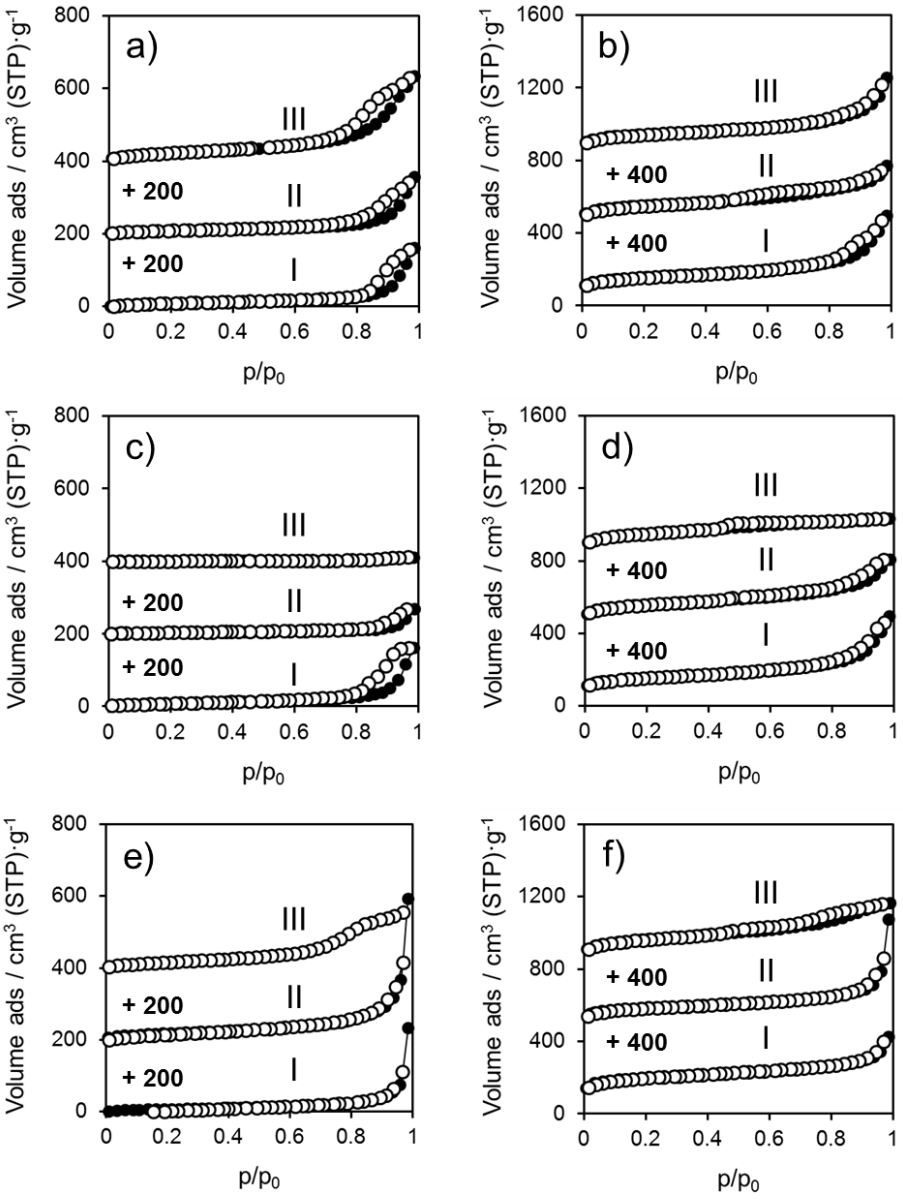

Figure A.1: N_2 adsorption (filled symbol) and desorption (unfilled symbol) isotherms of (a, b) aniline, (c, d) benzyl alcohol and (e, f) butanol spheres. Isotherms are vertically shifted in steps of $200\,cm^3\,g^{-1}$ for (a, c, e) as prepared and in steps of $400\,cm^3\,g^{-1}$ for (b, d, f) calcined SiO_2 spheres. 0 (I) , 1 (II) and 7 (III) wt.% Zr^{4+}.

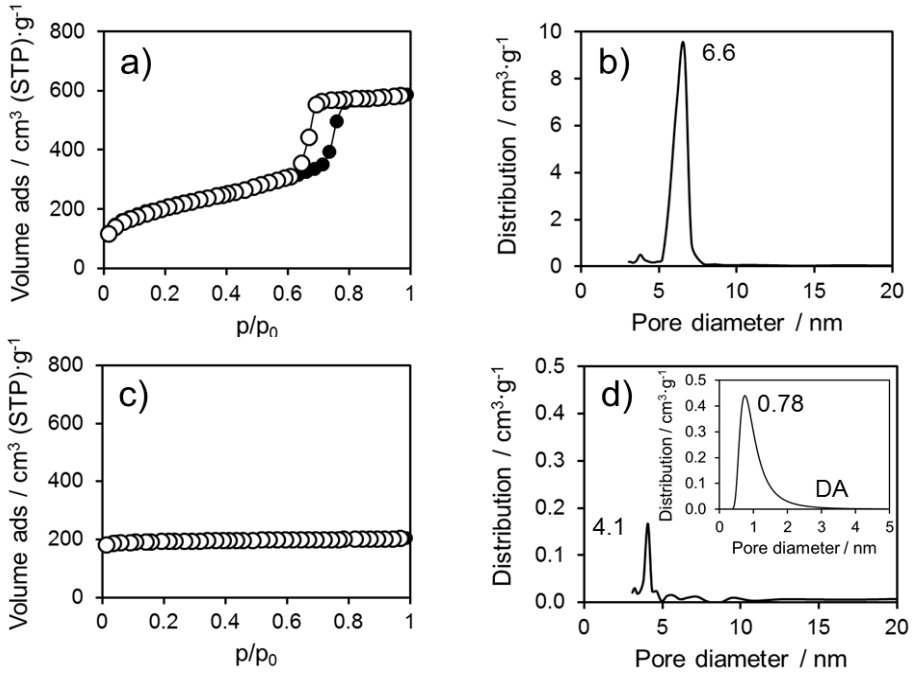

Figure A.2: N_2 physisorption isotherms of (a) SBA-15 and (c) zeolite 13X. Filled and empty symbols represent adsorption and desorption branches, respectively. Pore size distribution of (b) SBA-15 and (d) zeolite 13X calculated by BJH method (N_2 desorption branch) and (d) additionally DA method for micropore analysis.

A.2 Chapter 3

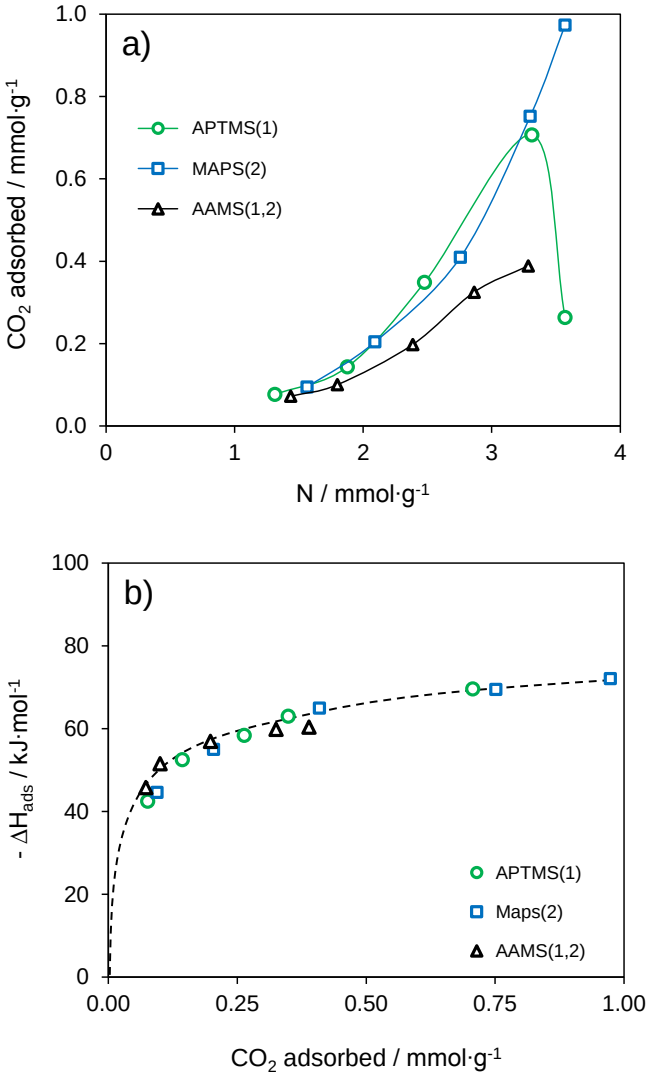

Figure A.3: (a) Adsorbed CO_2 over the amine concentration and (b) heats of adsorption versus adsorbed CO_2. Values determined by TGA DSC under flow conditions at 50 °C.

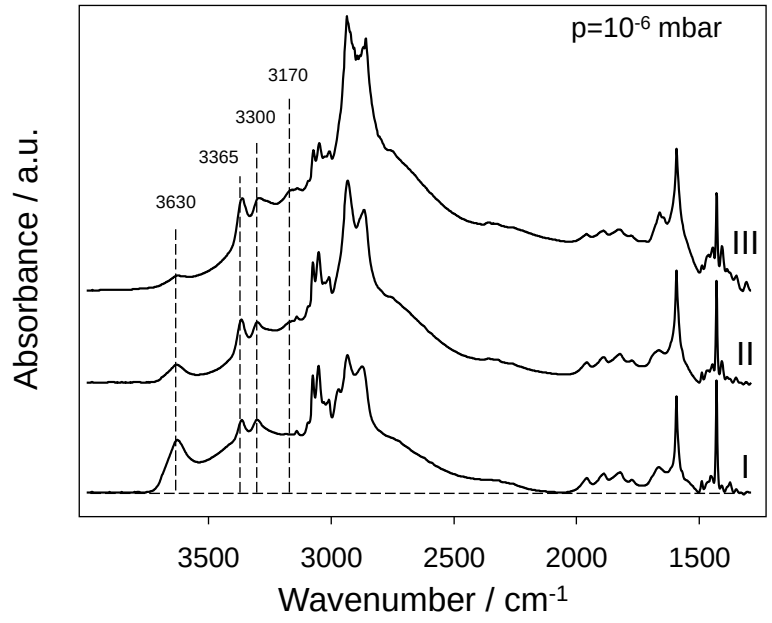

Figure A.4: Absolute IR spectra of (I) APTMS(1) (3.57 mmol g^{-1}), (II) MAPS(2) (3.57 mmol g^{-1}) and (III) AAMS(1,2) (3.29 mmol g^{-1}). Spectrum range from 3500 - 1250 cm^{-1}. Absorbance in absorption units.

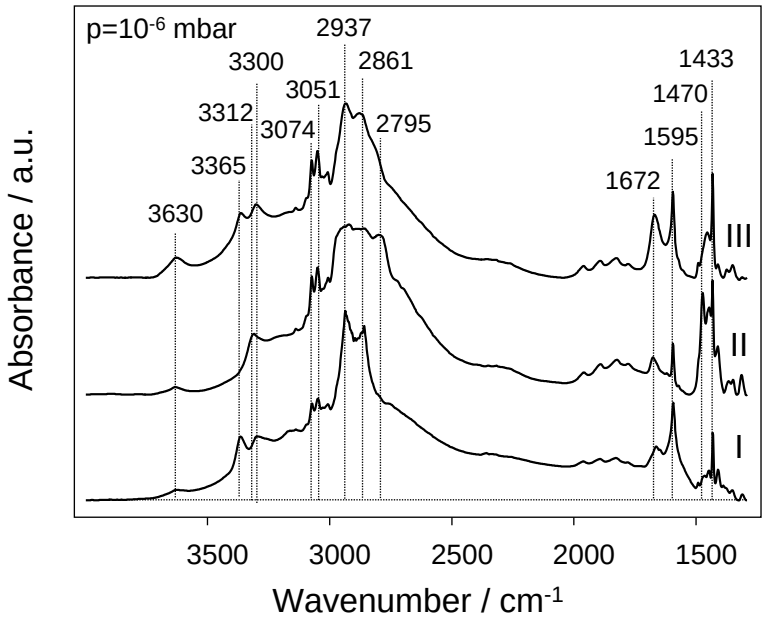

Figure A.5: Absolute IR spectra of APTMS(1) with an amine content of (I) 1.31 (II) 2.48 and (III) 3.57 mmol g^{-1} in the spectrum range of 1850 - 1250 cm^{-1}. Absorbance in absorption units.

Table A.1: Overview of relevant IR bands of amine functionalized SiO_2 supports.

Wavenumber / cm^{-1}	Assignment	References
>3750	OH stretching vibration of free silanol groups (support)	[98,104,109]
3700 - 3000	OH stretching of hydrogen bonded OH groups (H_2O)	[104,105]
3650 - 3630	OH stretching of hydrogen bonded OH groups (support)	[104,106,110]
3370 - 3360	Asymmetric NH_2-stretching vibration of primary amines	[89,106,112]
3330 - 3300	Symmetric NH_2-stretching vibration of primary amines NH-stretching vibration of secondary amines	[89,91,106,110]
3090 - 3010	CH stretching vibration in aromatics	[111,152]
2930 - 2850	CH_2 stretching vibration	[91,106,110]
2820 - 2760	NCH_3 stretching vibration	[153]
1680 - 1600	Deformation of primary NH_2 and secondary amines NH	[89,104,106,110,112]
1470 - 1440	CH_2 bending	[91,104,110,154]
1440 - 1410	CN stretching	[91,110,154,155]

A.3 Chapter 4

Activation of the sorbents

The changes in the chemical composition of DETA 23 before and after activation at 100 °C and 10^{-2} mbar for 2 h are listed in Table A.2. DETA impregnated SBA-15 with an amine loading of 23 wt.% was used, because the amine exhibits a boiling point of 200 °C and the highest vapor pressure (0.5 mbar) of all employed amines. The vapor pressure of TEPA and PEI are both significantly lower and therefore these molecules are less likely to desorb during the thermal activation in vacuum. The concentration of C and H decreased significantly (15 % for C and 11 % for H), because chemisorbed CO_2 and physisorbed H_2O were removed during activation. In contrast, the concentration of N was not affected (within the limits of accuracy ± 5 %) confirming that the loss of amines in the activation step prior to N_2 physisorption can be neglected.

Table A.2: C, H, N analysis before and after activation of DETA 23 at 100 °C and 10^{-2} mbar for 2 h.

	C / mmol g^{-1}	H / mmol g^{-1}	N / mmol g^{-1}
DETA 23 no activation	9.7	41.3	6.5
PEI 23 activated	8.6	35.1	6.3

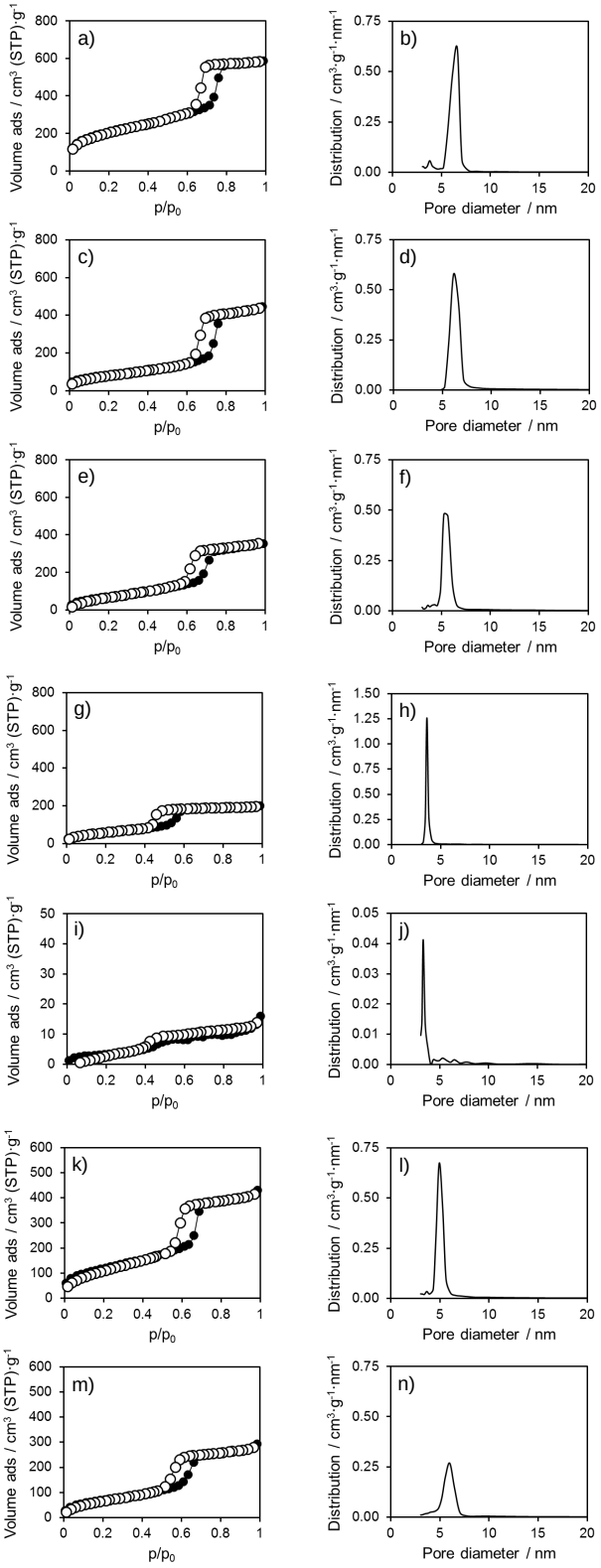

Figure A.6: N_2 physisorption isotherms and pore size distribution (BJH method) of (a, b) SBA-15, (c, d) DETA 9, (e, f) DETA 23, (g, h) TEPA 9, (i, j) TEPA 23, (k, l) PEI 5, (m, n) PEI 18. Filled and empty symbols represent the adsorption and desorption branch, respectively.

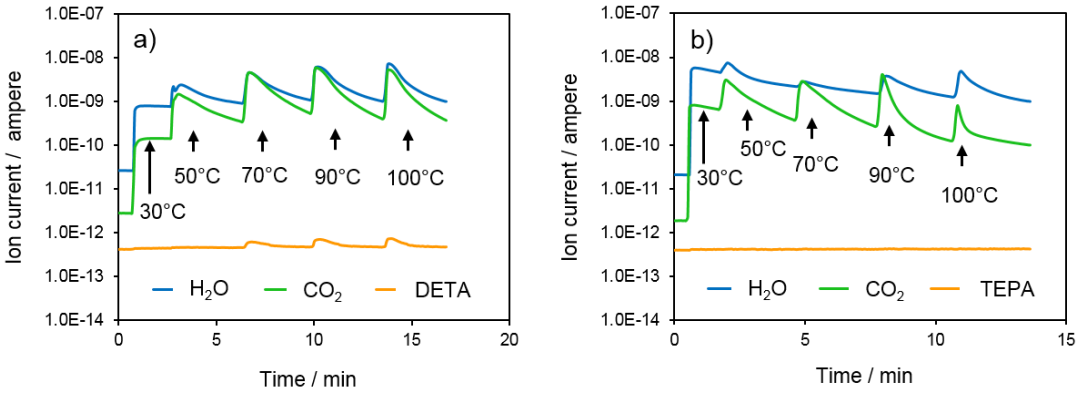

Figure A.7: Desorption species monitored by mass spectrometry during activation at 10^{-6} mbar (30 - 100 °C) for (a) DETA 23 and (b) TEPA 23.

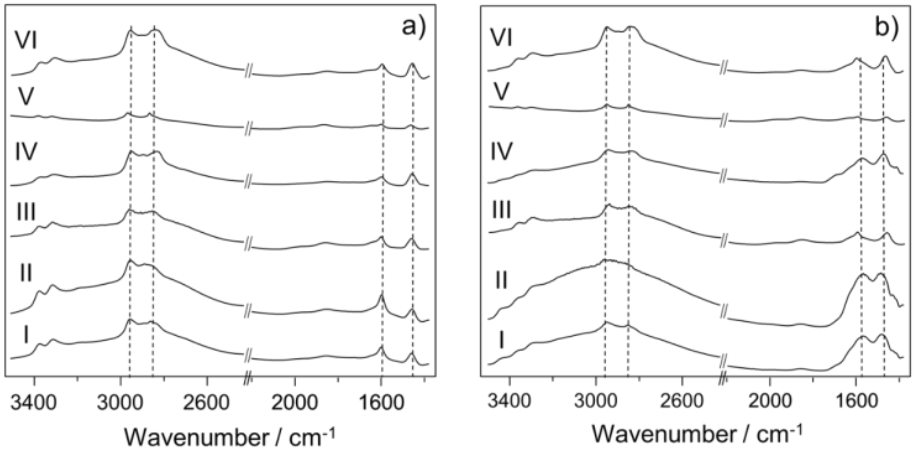

Figure A.8: Absolute IR spectra of (I) DETA 9 and (II) DETA 23, (III) TEPA 9 and (IV) TEPA 23, (V) PEI 5 and (VI) PEI 18 at 50 °C and CO_2 partial pressure of (a) 0 mbar and (b) 10 mbar.

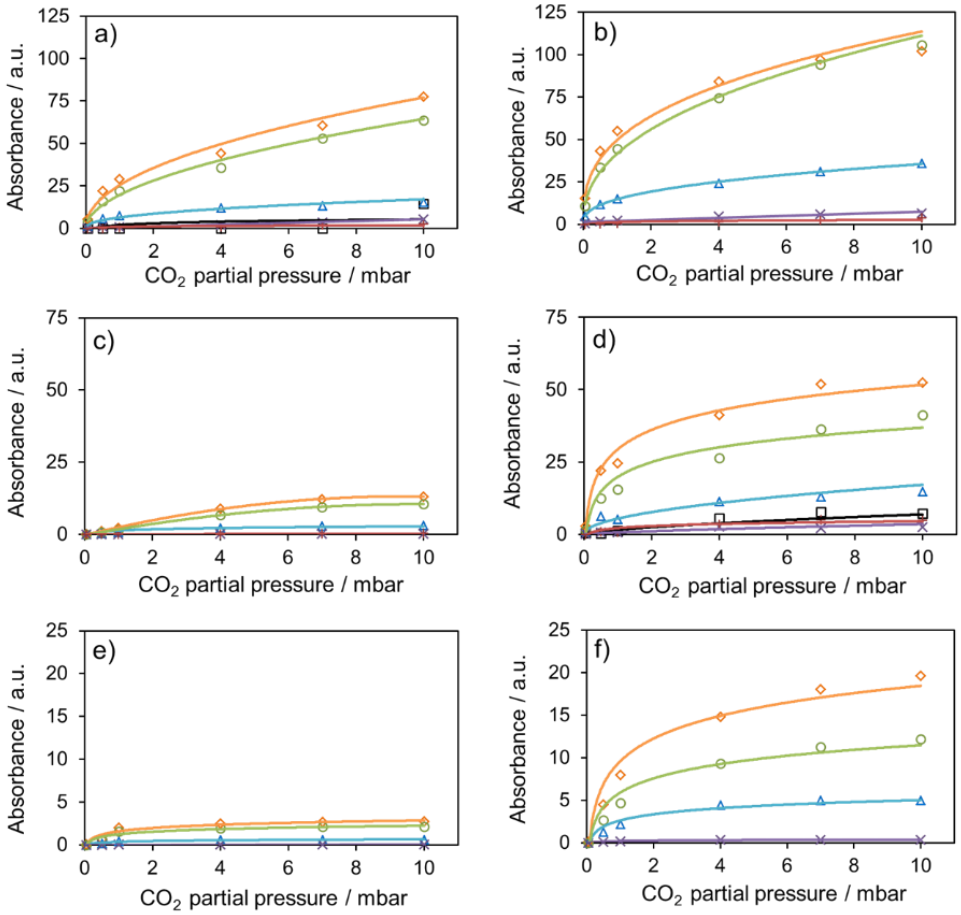

Figure A.9: Integrated equilibrium IR peak areas (1750 - 1350 cm^{-1}) of (a) DETA 9, (b) DETA 23, (c) TEPA 9, (d) TEPA 23, (e) PEI 5, (f) PEI 18 at CO_2 partial pressures between 0.05 mbar and 10 mbar. Resonances at (□) 1670 cm^{-1}, (Δ) 1630 cm^{-1}, (◇) 1463 cm^{-1}, (○) 1490 cm^{-1}, (×) 1430 cm^{-1} and (+) 1415 cm^{-1}.

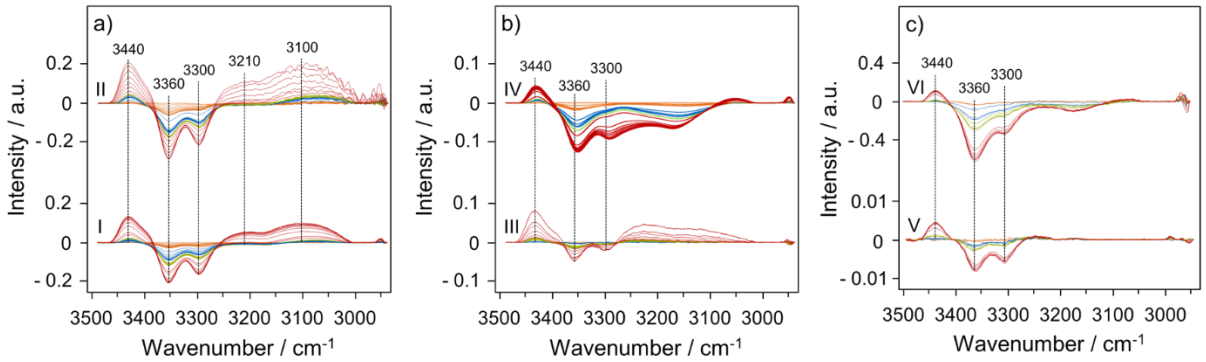

Figure A.10: Difference IR spectra (3500 - 2950 cm^{-1}) taken every 120 s in a pressure range of 0.05 mbar - 10 mbar: 0.05 mbar (–), 0.5 mbar (–), 1.0 mbar (–) and 10 mbar (–). (a) DETA 9 (I) and DETA 23 (II), (b) TEPA 9 (III) and TEPA 23 (IV), (c) PEI 5 (V) and PEI 18 (VI).

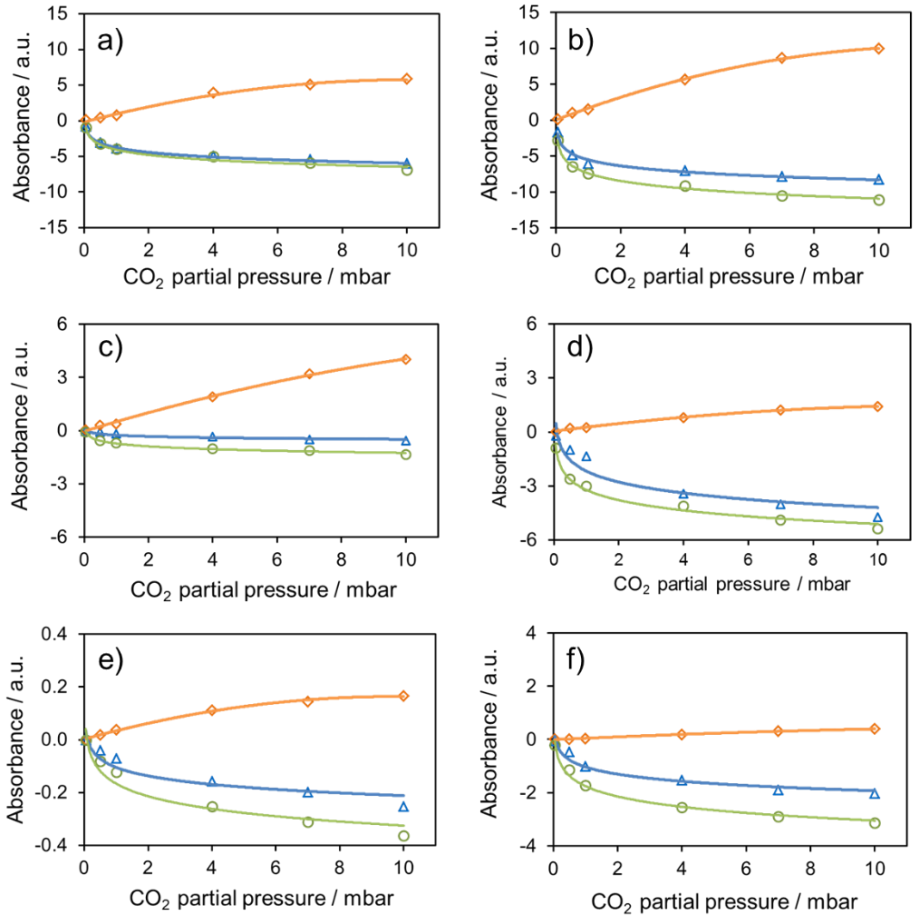

Figure A.11: Integrated equilibrium IR peak areas (3440 - 3300 cm^{-1}) of (a) DETA 9, (b) DETA 23, (c) TEPA 9, (d) TEPA 23, (e) PEI 5, (f) PEI 18 at CO_2 partial pressures between 0.05 mbar and 10 mbar. Resonances at (◇) 3440 cm^{-1}, (○) 3365 cm^{-1} and (Δ) 3300 cm^{-1}.

Table A.3: Overview of relevant IR bands for the adsorption of CO_2 on amine functionalized SiO_2 supports in the range of 4000 - 1300 cm^{-1}.

Wavenumber / cm^{-1}	Assignment	References
3715, 3615	Combination band of gas phase CO	[110,156]
3440 - 3420	CO stretching vibration (carbamic acid)	[33,104,112]
3000	Stretching vibration of COOH (carbamic acid, broad peak)	[111,157]
2345	Gas phase CO_2	[112,131]
	Asymetric stretching of linearly physisorbed CO_2	
1720 - 1670	CO stretching vibration (carbamic acid)	[104–108]
1660 - 1620	Asymmetric NH_3^+/NH_2^+ deformation	[109–111]
1565 - 1550	Asymmetric COO^- stretching vibration	[33,98,104,112]
1490 - 1480	Symmetric NH_3^+/NH_2^+ deformation	[110–112]
1430 - 1400	Symmetric COO^- stretching vibration	[110–112]
1380	OH deformation (carbamic acid)	[107,108]
1330 - 1300	NCOO skeletal vibration	[33,98,106]